ELECTRON PARAMAGNETIC RESONANCE (EPR) SPECTROSCOPIC INVESTIGATION OF DEFECT CENTERS IN SELECTED BORATES AND BOROSILICATES

A Thesis Submitted to the College of Graduate Studies and Research

in Partial Fulfillment of the Requirements for the Degree of Master in Sciences

in the Department of Geological Sciences

University of Saskatchewan

Saskatoon

by

Rong Li

2012

Permission to use:

In presenting this thesis in partial fulfillment of the requirements for a Master degree in Science from the University of Saskatchewan, I agree that the Libraries of this University may make it freely available for inspection. I further agree that permission for copying of this thesis in any manner, in whole or in part, for scholarly purposes may be granted by the professors who supervised my thesis work, or, in their absence, by the Head of the Department of Geological Sciences or the Dean of the College of Graduate Studies and Research, in which my thesis work was done. It is understood that any copying or publication or use of this thesis or parts thereof for financial gain shall not be allowed without my written permission. It is also understood that due recognition shall be given to me and to the University of Saskatchewan in any scholarly use which may be made of any material in my thesis.

Request for permission to copy or to make other use of material in this thesis, in whole or in part, should be address to:

Head of the Department of Geological Sciences

University of Saskatchewan

114 Science Place

Saskatoon, Saskatchewan,

S7N 5E2 CANADA

Abstract

This thesis presents the results of a single-crystal electron paramagnetic resonance (EPR) spectroscopic investigation of defect centers in selected borates and borosilicates (i.e., datolite, danburite, and jeremejevite). The research brings new complementary data to the current understanding of defect structures in minerals, which are not only important to Earth Sciences but also directly relevant to environmental applications (e.g., nuclear waste disposal) and materials science.

Single-crystal EPR spectra of a gamma-ray-irradiated datolite from Bergen Hill, New Jersey, USA, reveal the presence of a boron-oxygen hole center (BOHC). Spin-Hamiltonian parameters obtained from single-crystal EPR spectra and radiation-dose-dependence experiments allow us to confirm the BOHC center in datolite as the $[BO_4]^0$ type, involving hole trapping on the hydroxyl oxygen atom after the removal of the hydrogen atom: via a reaction $O_3BOH \rightarrow O_3BO^{\bullet} + H^0$, where $\bullet$ denotes the unpaired electron. Density functional theory (DFT) calculations support the proposed structural model, and the calculated ^{11}B hyperfine coupling constants are in excellent agreement with the experimental results. Also, isochronal and isothermal annealing experiments provide information about the thermal stability and decay kinetics of the $[BO_4]^0$ center in datolite. The confirmation of the $[BO_4]^0$ center and its formation from the O_3BOH precursor in datolite are compared with other BOHCs in minerals and are discussed with relevance to the implications for not only understanding of BOHCs in alkali borosilicate glasses but also their applications to

nuclear waste disposal.

A combined study by use of synchrotron X-ray absorption spectroscopy (XAS), single-crystal EPR and pulse electron spin echo envelope modulation (ESEEM) spectroscopy provides compelling evidence for lattice-bound arsenic in danburite from Charcas, San Luis Potosi, Mexico. Arsenic K-edge X-ray absorption near-edge (XANES) spectra show that the dominant oxidation state is +3, and modeling of the extended X-ray absorption fine structure (EXAFS) spectra suggests that As^{3+} mainly occupies the Si site. Detailed single-crystal EPR spectra, measured before and after gamma-ray irradiation, reveal three arsenic-associated paramagnetic electron centers (I, II and III). Centers I and II are varieties of the $[AsO_2]^{2-}$ radicals, formed from electron trapping on a substitutional As^{3+} ion at the Si site. This model is also supported by the ^{11}B superhyperfine structures determined by ESEEM spectra at 80 K. Center III is the $[AsO_3]^{2-}$ radical, originated from electron trapping on a $[AsO_4]^{3\neg}$ group after removal of the O4 atom during gamma-ray irradiation. Therefore, arsenic in danburite is present in both the +3 and +5 oxidation states and preferentially occupies the Si site.

Single-crystal EPR spectra of jeremejevite from Cape Cross, Namibia, reveal an $S = 1/2$ hole center characterized by a hyperfine structure arising from interaction with two equivalent ^{27}Al nuclei. Our results suggest that this aluminum-associated oxygen hole center represents hole trapping on a hydroxyl oxygen atom linked to two equivalent octahedral Al^{3+} ions, after the removal of the proton (i.e., a $^{VI}Al{-}O^{-}{-}^{VI}Al$ center). Periodic *ab initio* UHF and DFT calculations confirmed the experimental ^{27}Al

hyperfine coupling constants and directions, supporting the proposed structural model. Also, isochronal annealing experiments provide information about the thermal stability of the $^{VI}Al–O^{-}–^{VI}Al$ center. These data obtained from the $^{VI}Al–O^{-}–^{VI}Al$ center in jeremejevite provide new insights into analogous defects that have been documented in several other minerals.

Acknowledgements

This research contained herein would have never been carried without the assistance and support of many people.

I extend sincere gratitude to my supervisor Dr. Yuanming Pan for his support and guidance that he generously gave me all these years, and to the members of my advisory committee: Dr. Matthew Paige, Dr. Jim Merriam, Dr. George Graham, and Dr. Kevin Ansdell.

I would also like to express my gratitude to Dr. Mark J. Nilges, Dr. Zucheng Li and Ms. Jinru Lin, for collaborative work with pulse electron spin echo envelope modulation (ESEEM) experiments, theoretical calculations, and synchrotron X-ray absorption spectroscopy (XAS), respectively.

Many thanks to the technical staff Mr. Blane Novakovski and Dr. Jianzhong Fan, who providing a friendly and cooperative work environment helping me with the sample preparation and inductively coupled plasma mass spectrometry (ICPMS) analysis, respectively.

I would like to thank Dr. Mao Mao who gave me precious advices in EPR spectroscopy and helped me undergo the complicated problems of spectral simulations and fittings.

My husband Yi Wang always supports me during this research, and I am eternally grateful to him. The birth of my son, Richard L. Wang, was a special moment during this study, and watching him grow has provided much perspective.

My parents, Ji Li and Yuling Feng, have encouraged my higher education for many years, and I lovingly thank them for constant support. I also wish to thank all my other close and extended family members and friends for their support and encouragement. They have always been there for me.

I gratefully acknowledge the Natural Science and Engineering Research Council (NSERC) of Canada for financial support through research grants to Dr. Yuanming Pan. My study was also supported by a 2011 Graduate Teaching Fellowship (GTF) from the University of Saskatchewan.

Thank you!

TABLE OF CONTENTS

LIST OF TABLES

LIST OF FIGURES

CHAPTER 1

Introduction

1.1 STUDY OVERVIEW

A crystal is a solid material whose internal particles (atoms, molecules, or ions) are arranged in an orderly, infinite repeating pattern extending in all three spatial dimensions. This ideal perfect crystal does not exist in reality, but it can be used as a theoretical research model. On the contrary, all natural and artificial crystals are not perfect and have gained tremendous recognition especially after the realization that many of their physical and chemical properties are often determined not so much by the structure of the material itself, but by the irregular arrangement of the faults and defects in the structures (Tilley 1987). The study of defect centers has long been the important subject of experimental and theoretical investigations from two main scientific perspectives: 1) they play the main role to determine and alter the physical and chemical properties of the host material in the solid state, and 2) they can be used as tracers of past geological conditions (i.e., irradiation, temperature, pressure, chemical heterogeneities), both of which require a fundamental understanding in regards to the type, concentration, formation mechanism, structural characteristics, electronic properties and dynamic stability of these defect centers (Kordas and Goldfarb 2008).

Defect centers exert profound impacts on the performance of various materials and have received intensive research worldwide. Physical properties of solid materials

such as optical, electrical, mechanical and magnetic properties have been shown to depend on the presence of defects (Petroff 1950; Teal and Little 1950; Seidel 1961; Marfunin 1995; Regenauer-Lieb *et al.* 2006). In addition, defects have a great influence on the chemical properties of solid materials. For example, on the surface of a metal, the impurity atoms and the host atoms will form the primary cell model in the atmospheric environments. If the impurities are as micro-cathodes, it will greatly accelerate the corrosion of the metal. In addition, surface energy will also be greatly affected by defects, such as surface chemical activity and chemical energy. In a word, defects in solid materials affect their performance substantially. But they may also improve certain aspects of the material if defects can be used properly. For example, the electrical conductivity of intrinsic semiconductors is not favorable because the charge carriers are usually very few in number. However, if traces of impurities are incorporated in semiconductor materials, the conductive properties can be greatly enhanced. Therefore, defect centers are very important and are foundations for the field of solid state physics, solid state chemistry, and materials science. Presently, controlling the type and concentration of defects in a material so as to tune its properties in order to achieve a desired manner is employed both in semiconductor and solid-state laser technology. The tremendous progress in understanding the changes in physical and chemical properties of materials as a result of defect center incorporation has helped to create an entirely new field of research, namely defect engineering which is proposed to undergo rapid development in the near future.

Moreover, as a result of natural high-energy irradiation (alpha, gamma or X-rays,

electrons, neutrons), the extensive occurrence of defect centers (electrons or positive holes) in various minerals led to their use as natural dosimeters, geothermometers and geochronometers (Ikeya 1993). For example, the basic principle of EPR dating is the same as for thermoluminescence (Calas 1988): if a mineral is subject to natural radiation from radioisotopes including uranium (^{238}U and ^{235}U), thorium (^{232}Th) and their daughter radioisotopes, and potassium (^{40}K) in the environment or inside an archaeological or geological material, the electronic and atomic defects will be produced in the material, some of which may be trapped by impurities as well as by inherent defects. They are often fairly stable and the defect concentration increases linearly with time. These defects can be detected by EPR. The intensity of EPR signal is proportional to the spin concentration and so to the total dose, i.e., the radiation dose rate and the time elapsed after their formation or an event, such as heating, which affects the spin concentration (Ikeya 1993). Therefore, it is necessary to establish the relation between EPR signal intensity and the radiation dose using artificial irradiation. Extrapolation to zero intensity gives the accumulated dose (AD) since time 0. If the annual dose rate is known, age may be derived. The age is calculated from the ratio between AD and the annual dose rate. The linearity of the relation AD and time requires that there is no saturation of the available hole/electron traps. EPR dating has been tested only in recent ($<10^6$ years) minerals, mainly calcite (Hennig and Grün 1983; Nambi 1985; Calas 1988). Being able to identify the type of defect centers with their particular production and annealing rates as a function of radiation dose and temperature has made their use as markers of past geological

events possible (Ikeya 1993; Pan *et al.* 2006).

Therefore, the presence of defect centers in minerals exert profound influences for diverse applications in various branches of science, between applied chemistry, solid state physics, materials science, medicine, archaeology, geochronology, mineralogy, geology, nuclear waste disposal and mineral resources exploration (Calas 1988; Ikeya 1993; Rossman 1994; Marfunin 1995; Rink 1997; Pan *et al.* 2006). Defect centers are also exploited in analytical methods and principles pertaining to all these areas.

Spectroscopic methods such as X-ray electron spectroscopy, optical absorption spectroscopy, infrared radiation (IR) spectroscopy, Raman spectroscopy, Mössbauer spectroscopy, nuclear magnetic resonance (NMR), electron nuclear double resonance (ENDOR), electron paramagnetic resonance (EPR) spectroscopy, to mention just a few, have been employed in the study of defect centers over the years.

Among these spectroscopic methods, EPR spectroscopy has been proven to be one of the most effective experimental methods for studying defect centers by far, because of its extremely high sensitivity (detection of extremely dilute paramagnetic centers, i.e. 0.0001%; Weil and Bolton 2007), which is up to 10,000 times that of optical absorption spectroscopy (Rossman 1994), and its ability to provide valuable additional information on both identification and assessment of their chemical nature, crystallographic symmetry and electronic structure environments of the paramagnetic species, which cannot be resolved by refinement of the crystal structure, nor by electron microprobe analysis (Calas 1988).

The limitation of EPR arises from its ability to detect only paramagnetic species; all diamagnetic entities are EPR-silent. However, this problem is easily overcome because most defect centers are paramagnetic, or can become paramagnetic as a result of irradiation. In the energetic ground state, these centers are in general diamagnetic. If these crystals are irradiated, free electrons and holes are created, which, subsequently, can be trapped at the defect and impurity sites. The centers are then converted into paramagnetic states and become accessible to EPR. Because of EPR's high sensitivity and interactions between paramagnetic ions, only paramagnetic centers embedded in diamagnetic matrices can be detected, which restricts EPR to the "white" minerals, such as those lacking iron (Calas 1988).

The paramagnetic species for EPR studies usually are of two types: either transition-metal (or rare earth) ions with partially filled inner electron shells substituting for a diamagnetic host ion, but in some cases, they may also be interstitial ions; or radiation defects formed by natural high-energy irradiation due to radioactivity or by subsequent artificial irradiations. Because of their characteristic optical absorption in the visible range they are sometimes also called color centers. The best-known examples are the F centers in alkali halides, i.e., electrons in anion vacancies (Schulman and Compton 1962; Vassilikou-Dova and Lehmann 1987).

EPR spectra describe the interaction between an electronic spin submitted to the influence of crystal field and an external magnetic field. As with the other spectroscopic techniques, EPR spectroscopy can be used to study crystalline as well as amorphous materials, including glasses, gels and aqueous solution. However,

although powder EPR spectra measurement can provide some valuable information, the distribution effects will significantly broaden the spectral peak width, which make the spectra analysis difficult; furthermore, because of distinct angle dependence and relaxation times of the paramagnetic centers, some sites may not be seen and an incorrect picture of the behavior of the element will be obtained. In addition, powder EPR spectra are generally lower in resolution and sensitivity than their single crystal counterparts, which make information obtained from these measurements ambiguous in comparison with that obtained from single crystal EPR technique. Single crystal EPR techniques gives unambiguous information about the valence state and site symmetry, and, at least for some ions, it enables precise determination of geometries (distortions of their first coordination spheres) from characteristics of their EPR spectra. Thus, occasionally, controversial site assignments can be unambiguously determined, provided the crystal structure of the pure host compound is known with sufficient accuracy. As a result, single crystal EPR spectroscopy has emerged as the research and analytical method of choice in the current study of defect centers. EPR spectra of oriented single crystals are needed to accurately determine various EPR parameters which can give information needed to locate an element in the crystal structure: the orientation of the Hamiltonian axes, the values of the E and D parameters, the values of HFS constant A, the origin of SHFS. However, it must be pointed out that the EPR is only sensitive to the Laue symmetry, i.e., it does not reflect the presence or absence of an inversion center (Calas 1988).

The research objectives of this present study are to determine the geometrical

and electronic structures of several defect centers in selected borate and borosilicate minerals. Defect centers in borate and borosilicate glasses are of technological importance, because they exert a profound influence on various properties for diverse applications from fiber optical wave guide materials to radiation dosimetry, nuclear encapsulation materials, fast ionic conductors, micro- and optoelectronics (Yasaitis and Smaller 1953; Lee and Bray 1963; Griscom *et al.* 1968; Shkrob *et al.* 2000; Shkrob and Tarasov 2000; Porwal *et al.* 2005; Kordas 1999, 2003, 2005; Kadam *et al.* 2008; Kordas and Goldfarb 2008; Filonovich *et al.* 2008; Mohapatra *et al.* 2009). The EPR characterization of these defect centers dated back to 1950s (Yasaitis and Smaller 1953; Lee and Bray 1963, 1964; Taylor and Griscom 1971; Taylor and Bray 1972; Griscom *et al.* 1968; Griscom 1993). In these early studies, EPR and optical absorption spectroscopy were used to investigate paramagnetic ions and radiation-induced paramagnetic defects. These spin centers were assumed to be electrons or holes trapped in various structural units in borate and borosilicate glasses. However, the atomic and electronic structure models and locations of these defects in the glass network are generally poorly understood and still controversial and are usually difficult to interpret with respect to their structures, owing to the fact that the variety of possible structures in the polymeric matrix. For this reason, though these defect centers in borate and borosilicate glasses were repeatedly studied afterwards (Shkrob *et al.* 2000; Carboni *et al.* 2003; Kordas and Goldfarb 2008), there is still a lot of uncertainty about characterizing the spin centers structurally in the glass network.

Therefore, we have attempted to simplify the problem by studying isolated defects trapped in the crystalline matrices investigated by single-crystal EPR and related techniques, and have been important in providing models for analogous centers in glasses (Reinberg 1964; Schirmer *et al.* 1965; Eachus and Symons 1968; Bershov and Martirosyan 1970; Herve and Maffeo 1970; Bacquet *et al.* 1974; Bershov and Marfunin 1981; Misra *et al.* 1983; Novozhilov *et al.* 1988; Shkrob and Tarasov 2000; Walsby *et al.* 2000). In particular, single-crystal EPR spectra can provide detailed information about the orientation of the paramagnetic species in the host lattice, hence making possible unambiguous identification and elucidation of the atomic and electronic structure under favorable conditions. For example, the classic $[BO_3]^{2-}$ radical which is established in gamma-ray-irradiated calcite (Eachus and Symons 1968) has long been cited as a model for this type of boron-oxygen hole center (BOHC) in glasses. Similarly, BOHC investigated in danburite (Shkrob and Tarasov 2000) is wishing to provide structure models for similar defects in alkali borosilicate glasses.

In this work, the purpose of the proposed research is to better understand the hyperfine structure of various defect centers in selected borates and borosilicates (i.e., datolite, danburite, jeremejevite) single crystals, by means of electron paramagnetic resonance (EPR) spectroscopy, in order to complement and confirm the previous EPR studies and provide structural models for analogous centers.

1.2 THESIS OUTLINE

This thesis is part of a broad study on defect centers in minerals. Aiming to bring new complementary data to the current understanding of defect structures in minerals, this body of research is a series which attempts to produce precise interaction matrix (tensor) and directional data in the micro-region and to investigate the nature and mechanism of paramagnetic defect species in crystalline systems in selected borate and borosilicates, namely datolite, danburite and jeremejevite, through EPR spectroscopy.

This thesis is divided into 4 parts. Chapter 2 is a synthesis of the fundamental theory of EPR spectroscopy. Each of the last 3 chapters is a separate article for peer-reviewed publications (Li *et al.* 2011; Li *et al.* 2012a; Li *et al.* 2012b).

Chapter 3 presents and discusses a well-resolved type of boron-oxygen hole centers ($[BO_4]^0$) in datolite. This study focuses on the electronic structure and formation mechanism of the $[BO_4]^0$ center and provides information about its thermal stability and decay kinetics. Density functional theory (DFT) calculations, which are done by Dr. Zucheng Li (Research Associate in Prof. Pan's group), support the proposed structural model, and yielded ^{11}B hyperfine coupling constants that were in excellent agreement with the experimental results. Also, Dr. Mao Mao assisted me in data fitting and spectral simulations during the initial state of this study. Both of them were included as co-authors of a paper that stemmed from this chapter (Li et al. 2011).

The structural properties of three well-resolved arsenic-associated electron centers (two $[AsO_2]^{2-}$ radicals and one $[AsO_3]^{2-}$ radical) in danburite are the second topic addressed by the present research. Combined results of synchrotron X-ray

absorption spectroscopy (XAS), single-crystal EPR and pulsed electron spin echo envelop modulation (ESEEM) spectroscopy are presented in Chapter 4, with the purpose to provide detailed information about arsenic speciation in danburite. X-ray absorption near-edge (XANES) and extended X-ray absorption fine structure (EXAFS) experiments and relevant interpretations were done by Ms. Jinru Lin (Ph.D. student in Prof. Pan's group) and Dr. Ning Chen (Beamline Scientist, Canadian Light Source). The proposed structural models for the two $[AsO_2]^{2-}$ radicals are evaluated further with the ^{11}B superhyperfine structures determined by ESEEM, which was done by Dr. Mark J. Nilges (Manager, Illinois EPR Research Center). All of them are included as co-authors of a manuscript that stemmed from this chapter (Li et al. 2012b).

Chapter 5 investigates a $^{VI}Al{-}O^{-}{-}^{VI}Al$ center in jeremejevite. Detailed analyses of the single-crystal EPR spectra allowed determination of the spin Hamiltonian of this center and its site assignments in the crystal structure. This center characterized by superhyperfine interactions with two ^{27}Al nuclei represents a close analog for the B center in kaolinite (Clozel et al. 1995). Periodic *ab initio* UHF and DFT calculations confirmed the experimental ^{27}Al hyperfine coupling constants and directions, supporting the proposed structural model, which is also done by Dr. Zucheng Li and was included as a co-author as well (Li et al. 2012a).

1.3 References

Bacquet, G., Dugas, J., Belin, C. (1974): RPE de BO_2 dans la calcite synthetique irradiee. 18th AMPERE Congress, Nottingham.

Bershov, L.V., Marfunin, A.S. (1981): On schemes of isomorphism of boron in alumosilicates, carbonates and sulfates according to electron-spin-resonance data. *Geokhimya*, **3**: 446-449.

Bershov, L.V., Martirosyan, V.O. (1970): Point defects in borosilicates danburite and datolite. *Soviet Physics Crystallography, USSR*, **14**: 823-825.

Calas, G. (1988): Electron paramagnetic resonance. *Reviews in Mineralogy*, **18**: 513-571.

Carboni, R., Pacchioni, G., Fanciulli, M., Giglia, A., Mahne, N., Pedio, M., Nannarone, S., Boscherini, F. (2003): Coordination of boron and phosphorous in borophosphosilicate glasses. *Applied Physics Letters*, **83**: 4312-4314.

Clozel, B., Gaite, J.M., Muller, J.P. (1995): $Al{-}O^{-}{-}Al$ paramagnetic defects in kaolinite. *Physics and Chemistry of Minerals*, **22**: 351-356.

Eachus, R.S., Symons, M.C.R. (1968): Oxides and oxyions of non-metals. X. BO_3^{2-} impurity center in irradiated calcium carbonate. *Journal of the Chemical Society A: Inorganic, Physical, Theoretical*, **10**: 2438-2441.

Filonovich, S.A., Ribeiro, M., Rolo, A.G., Alpuim, P. (2008): Phosphorous and boron

doping of nc-Si:H thin films deposited on plastic substrates at 150℃ by hot-wire chemical vapor deposition. *Thin Solid Films*, **516**: 576-579.

Griscom, D.L. (1993): Experimental Techniques of Glass Science, chap. 6, American Ceramic Society, Westerville OH, p 161.

Griscom, D.L., Taylor, P.C., Ware, D.A., Bray, P.J. (1968): ESR studies of lithium borate glasses and compounds γ irradiated at 77ºK: Evidence for a new interpretation of the trapped-hole centers associated with boron. *The Journal of Chemical Physics*, **48**: 5158-5173.

Hennig, G.J., Grün, R. (1983): ESR dating in quaternary geology. *Quaternary Science Reviews*, **2**: 157-238.

Herve, A., Maffeo, B. (1970): Electron paramagnetic resonance of a new boron center in BeO irradiated with neutrons. *Journal de Physique*, **31**: 673.

Ikeya, M. (1993): New applications of electron paramagnetic resonance: ESR dating, dosimetry, and spectroscopy. World Scientific, Singapore.

Kadam, R.M., Seshagiri, T.K., Natarajan, V. and Godbole, S.V. (2008): Radiation induced defects in $BaBPO_5$: Ce and their role in thermally stimulated luminescence

reactions: ESR and TSL investigations. *Nuclear Instruments and Methods in Physics Research B*, **266**: 5137-5143.

Kordas, G. (1999): Complementary use of cw-EPR, HYSCORE and pulse ENDOR spectroscopies for scanning the environment of unpaired states in a- and c-B_2O_3. *Journal of Non-Crystalline Solids*, **260**: 75-82.

Kordas, G. (2003): Equivalent exploitation of four-pulse one-dimensional ESEEM and HYSCORE spectroscopies for the elucidation of BOHC defects in borate glasses supported by quantum mechanical calculations. *Physical Review B*, **68**: 024202.

Kordas, G. (2005): On the structure of the BOHC in the borosilicate and borophosphosilicate glasses. *Journal of Non-Crystalline Solids*, **351**: 2358-2360.

Kordas, G., Goldfarb, D. (2008): Characterization of borate glasses by W-band pulse electron-nuclear double resonance spectroscopy. *The Journal of Chemical Physics*, **129**: 154502.

Lee, S., Bray, P.J. (1963): Electron spin resonance studies of irradiated glasses containing boron. *Journal of Chemical Physics*, **39**: 2863-2873.

Lee, S., Bray, P.J. (1964): ESR studies of irradiated alkali borate glasses with high

alkali oxide content. *Journal of Chemical Physics*, **40**: 2982-2988.

Li, R., Li, Z., Mao, M., Pan, Y. (2011): Single-crystal EPR and DFT studies of a $[BO_4]^0$ center in datolite electronic structure, formation mechanism and implications. *Physics and Chemistry of Minerals*, **38**: 33-43.

Li, R., Li, Z., Pan, Y. (2012a): Single-crystal EPR and DFT study of a $^{VI}Al{-}O^{-}{-}^{VI}Al$ center in jeremejevite: electronic structure and ^{27}Al hyperfine constants. *Physics and Chemistry of Minerals*, **39**: 491-501.

Li, R., Lin, J., Nilges, M.J., Chen, N., Pan, Y. (2012b): Arsenic speciation in danburite ($CaB_2Si_2O_8$): A synchrotron XAS, single-crystal EPR and pulsed ESEEM study. (in review)

Marfunin A.S. (1995): Composition, structure and properties of mineral matter. Springer, Berlin.

Misra, S.K., Bandet, J., Bacquet, C., McEnally, T.E. (1983): Electron spin resonance studies of defect centers containing boron atoms in natural danburite crystals. *Physica Status Solidi. A, Applied Research*, **80**: 581-588.

Mohapatra, M., Kadam, R.M., Tomar, B.S., Mishra, R.K., Kaushik, C.P., Godbole,

S.V., Raj, K., Manchanda, V.K. (2009): EPR investigations of electron beam irradiated Trombay waste base glass. *IOP Conference Series-Materials Science and Engineering*, **2**: 012022 (1-4).

Nambi, K.S. (1985): Scope of electron spin resonance in thermally stimulated luminescence studies and its chronological applications. *Nuclear Tracks and Radiation Measurements*, **10**: 113-131.

Novozhilov, A.I., Nosv. S.P., Gorbacheva, G.A., Samoilovich, M.I. (1988): EPR and optical absorption of color centers in danburite. *Mineral. Zh.* **10**: 85-88 (in Russian).

Pan, Y., Botis, S., Nokhrin, S. (2006): Application of natural radiation-induced paramagnetic defects in quartz to exploration in sedimentary basins. *Journal of China University of Geosciences*, **17**: 258-271.

Petroff, S. (1950): Photochemical observation of KCl crystals. *Zeitschrift fur Physik*, **127**: 443-454.

Porwal, N.K., Kadam, R.M., Seshagiri, T.K., Natarajan, V., Dhobale, A.R., Page, A.G. (2005): EPR and TSL studies on MgB_4O_7 doped with Tm: role of BO_3^{2-} in TSL glow peak at 470 K. *Radiation Measurements*, **40**: 69-75.

Regenauer-Lieb, K., Hobbs, B., Yuen, D.A., Ord, A., Zhang, Y., Mulhaus, H.B., Morra, G. (2006): From point defects to plate tectonic faults. *Philosophical Magazine*, **86**: 3373-3392.

Reinberg, A.R. (1964): Electron spin resonance of boron in single-crystal BeO. *Journal of Chemical Physics*, **41**: 850-855.

Rink, W.J. (1997): Electron spin resonance (ESR) dating and ESR applications in quaternary science and archaeometry. *Radiation Measurements*, **27**: 975-1025.

Rossman G.R. (1994): Colored varieties of silica minerals. *Reviews in Mineralogy*, **29**: 433-467.

Schirmer, O.F., Muller, K.A., Schneider, J. (1965): Electron spin resonance of donor centers in beryllium oxide. *Physik der Kondensiterten Materie*, **3**: 323-334.

Schulman, J.H., Compton, W.D. (1962): Color centers in solids. Pergamon Press, New York.

Seidel, H. (1961): Elektronen-kern-doppelresonanz-spektren von F-zentren in alkalihalogenid-kristallen. *Zeitschrift fur Physik*, **165**: 218-238.

Shkrob, I.A., Tadjikov, B.M., Trifunac, A.D. (2000): Magnetic resonance studies on radiation-induced point defects in mixed oxide glasses: I. Spin centers in B_2O_3 and alkali borate glasses. *Journal of Non-Crystalline Solids*, **262**: 6-34.

Shkrob, I.A., Tarasov, V.F. (2000): On the structure of trapped hole in borosilicates. *Journal of Chemical Physics*, **113**: 10723-10732.

Taylor, P.C., Bray, P.J. (1972): Electron-spin resonance of Mn2+ in strontium borate compounds and glasses. *Journal of Physics and Chemistry of Solids*, **33**: 43-58.

Taylor, P.C., Griscom, D.L. (1971): Toward a unified interpretation of ESR trapped-hole centers in irradiated borate compounds and glasses. *Journal of Chemical Physics*, **55**: 3610-3611.

Teal, G.K., Little, J.B. (1950): Growth of germanium single crystals. *Physical Review*, **78**: 647.

Tilley, R.J.D. (1987): Defect crystal chemistry and its applications. Chapman and Hall, NY.

Vassilikou-Dova, A.B., Lehmann, G. (1987): Investigations of minerals by electron paramagnetic resonance. *Fortschritte der Mineralogie*, **65**: 173-202.

Walsby, C.J., Lees, N.S., Tennant, W.C., Claridge, R.F.C. (2000): 15 K EPR of an oxygen-hole boron center, $[BO_4]^0$, in x- irradiated zircon. *Journal of Physics. Condensed Matter*, **12**: 1441-1450.

Weil, J.A., Bolton, J.R. (2007): Electron paramagnetic resonance: elementary theory and practical applications. Wiley-Interscience.

Yasaitis, E.L., Smaller, B. (1953): Paramagnetic resonances in irradiated glasses. *Physical Review*, **92**: 1068-1069.

CHAPTER 2

Fundamentals of EPR

2.1 OVERVIEW

The phenomenon of electron paramagnetic resonance was first reported in 1945 by Zavoisky (Zavoisky 1945) but was not extensively applied to materials research until the end of the 1950's. Electron paramagnetic resonance (EPR) spectroscopy is also called electron spin resonance (ESR) spectroscopy and the two names are equally well justified, because most often this paramagnetism is due to electron spin (Vassilikou-Dova and Lehmann 1987). It is a spectroscopic technique based upon observing resonance absorption of microwave power by unpaired electron spins in a tuned externally applied magnetic field.

One of the main methods to produce paramagnetic centers is irradiation, which includes γ-ray, X-ray, electron, and neutron sources. Both γ- and X-ray radiation is very high in energy, and can excite electrons to higher energy levels, and even other atoms or molecules orbitals to form holes or electron centers. Electron and neutron irradiation are particle radiation methods. The electron particles have electric and magnetic fields; they can influence the electrons in the crystals to form paramagnetic centers. The neutron particles which only have kinetic energies also can produce paramagnetic defects in the crystals, and the nuclear reactions are usually happening at the same time. The irradiation dose depends on the exposure time of the sample, but the defects produced usually are small in absolute numbers.

EPR spectroscopy can detect all kinds of paramagnetic species, which include: (a) free radicals in solid, liquid or aqueous phases; (b) transition metal ions; (c) various point defects in crystals; (d) systems with more than one unpaired electron (biradicals or triplet-state systems); and (e) systems with conducting electrons (metals and semiconductors, Weil and Bolton 2007).

In recent years, owing to the development of more sophisticated, commercially available EPR spectrometers, the analytical technique is now a powerful tool which is widespread used in various branches of science, such as physics, chemistry, biology and related fields of study, for the detection and identification of free radicals and paramagnetic centers.

2.2 EPR SPECTROMETER

Conventional EPR measurements are done in one of two modes: frequency-sweep or field-sweep. From the resonance condition one could in principle survey the EPR spectrum by varying the radiation frequency, as in optical spectroscopy, and keeping the magnetic field constant. In most EPR measurements, it is more convenient to do the reverse, i.e., to utilize a fixed microwave frequency and scan the EPR spectrum by varying the magnetic field until the resonance condition is matched.

A basic magnetic field-sweep EPR spectrometer requires a microwave bridge, a variable magnetic field, a resonant cavity, a solid-state diode detector, and a computer for data acquisition. Commercial EPR spectrometers commonly operate within band

frequencies of X band (ν = ~9300 MHz), K band (ν = ~24000 MHz), Q band (ν = ~37500 MHz), and W band (ν = ~95000 MHz) (Marfunin 1979).

The principle of the EPR method is as follow (Fig. 2-1): at first, a microwave of specific frequency is produced from an oscillator, called a Klystron or Gunn-diode, and then enters the isolator which enables the microwaves to vibrate at the same orientation. The energy of microwave can be adjusted after it goes through the attenuator. When the microwave reaches the directional coupler, it will split the microwave into two parts: one is sent to the monitoring detector to record as a standard for comparison, and the other is led to the resonant cavity in the static magnetic field produced by the electromagnets. The sample that contains the unpaired paramagnetic electrons is adjusted in a resonant cavity, and the strength of the magnetic field is rising linearly in a specific range by slowly changing the current in the electromagnet coils. Once the microwave reaches the detector, the detector starts to record the signal, and compare with the standard signal from the monitoring detector to analyze the quantity of absorption. Finally, the signal is amplified by the amplifier and recorded by the computer. During this process, the intensity of the magnetic field is rising linearly in a specific range, and resonances will take place in certain magnetic field intensities depending on the sample in the cavity. Therefore, in the final spectrum, the x-coordinate represents the range of magnetic field intensity, and the y-coordinate represents the intensity of absorption for the invariable microwave. In addition, most EPR spectra normally display, not as the direct resonance absorption lines, but as their first derivatives of the absorption curve. This

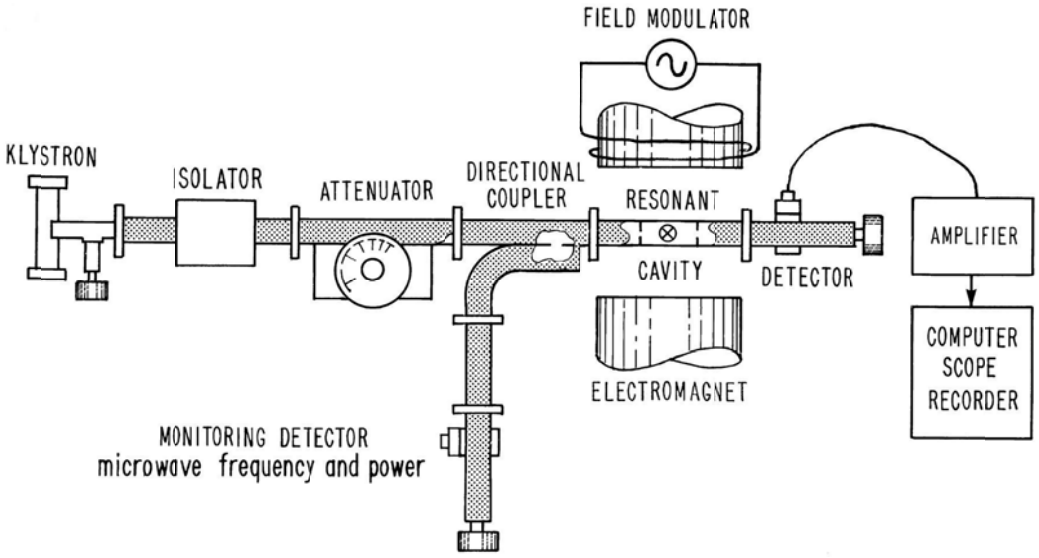

Figure 2-1 Block diagram of a continuous-wave (cw) electron paramagnetic resonance (EPR) spectrometer.

is due, firstly, to a greater distinction of the individual lines in complex spectra, that is, small inflexions in the absorption spectrum are much more obvious in the derivative spectrum; and secondly, to the technical convenience of registering the first derivative (Bersohn and Baird 1966).

Crucial to identifying defect centers is a careful analysis of the experimental EPR spectra, utilizing the correct theory and appropriate experimental "tricks" and computational tools. A flow diagram is given to illustrate a typical approach to this procedure (Fig. 2-2).

In this project, all EPR spectra have been measured by use of the Bruker EMX spectrometer operated at the X-band frequencies (~9.36 to 9.89 GHz) at either room temperature (~300 K) or low temperature (down to liquid nitrogen or liquid helium temperature), equipped with an automatic frequency controller, an ER4119 HS cavity, an ER218G1 goniometer with an angle uncertainty of ~0.2°, and an Oxford liquid helium-liquid nitrogen cryostat, at the Saskatchewan Structural Science Center (SSSC), University of Saskatchewan.

The mineral specimens selected for this study are all from the University of Saskatchewan reference mineral collection. EPR spectra are measured on either the as-is crystals or those after gamma-ray irradiation in a ^{60}Co cell with a dose rate of ~460 Gy/h, which are then analyzed to identify and characterize the detailed information on the structure and geometric particularities of various radiation-induced defects (i.e., electron and hole centers).

The main experimental procedure is as follow: Glue the single crystals with

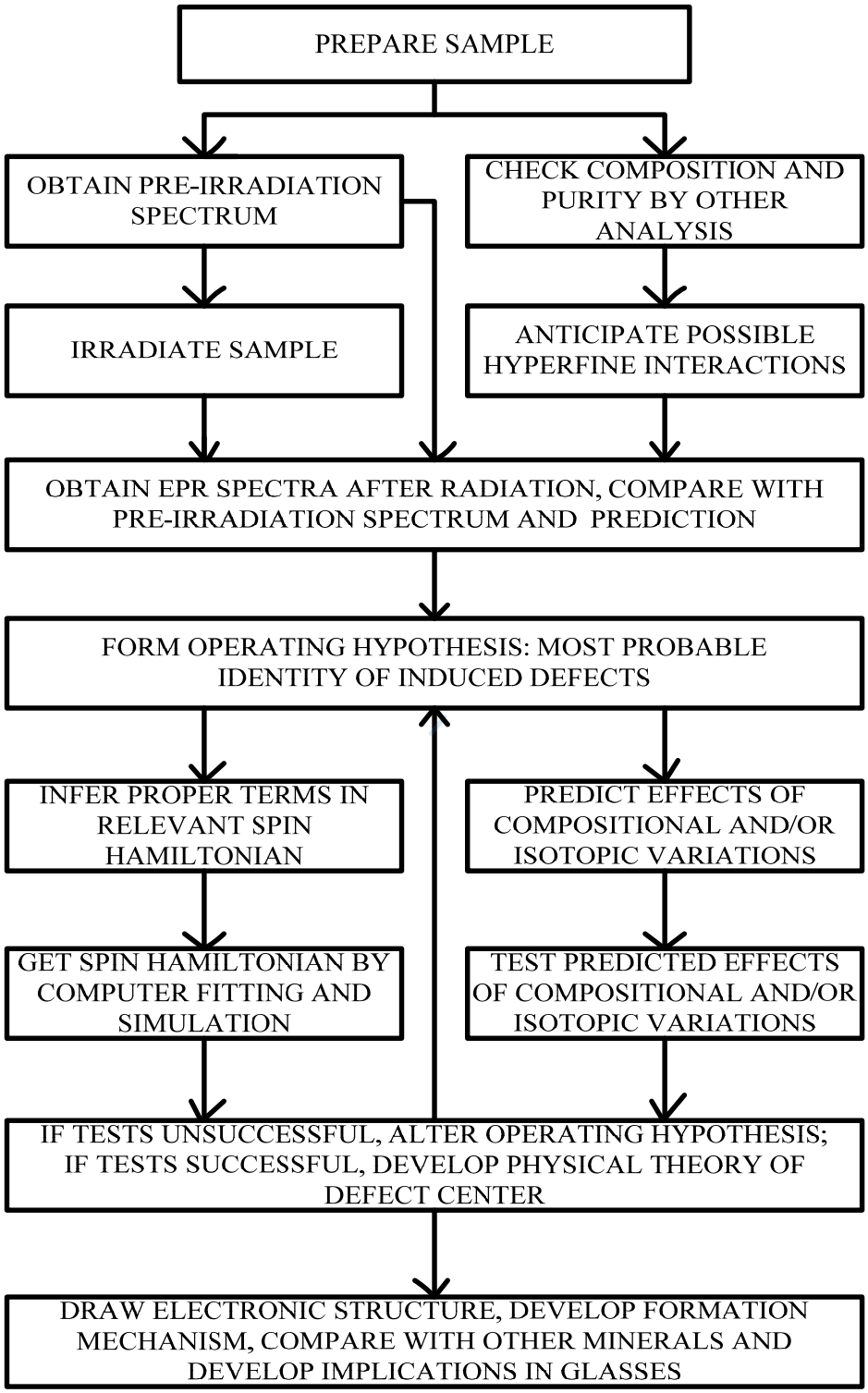

Figure 2-2 Flow diagram illustrating a typical approach to the study of radiation-induced defects in minerals by means of electron paramagnetic resonance techniques.

well-developed faces or cleavage planes to the end of an amorphous silica rod by vacuum grease. Insert the rod into a NMR tube so that the crystal would not fall into the cavity and thus contaminating it. Attach the tube to a goniometer for angular measurements. And then put the whole system into the resonant cavity. The angle intervals for all single-crystal measurements are 5°. Furthermore, powder EPR measurements were prepared by using ~200 mg pulverized selected samples in amorphous silica tubes. Also, more experimental parameters are required, i.e., selection of microwave power, modulation amplitude, spectral resolution, temperature.

For the low temperature experiments, the EPR tube was used, and there was a very weak E_1' center from the tube itself. Magnetic-field calibrations were made by use of the free radical α, γ-bis-diphenylene-β-phenyl allyl in benzene (BDPA; g = 2.0027) at room temperature and the Bruker strong pitch (g = 2.0028) at low temperature, respectively. Gamma-ray-irradiation experiments and thermal annealing experiments were also carried out to examine the stability of these centers.

The software package EPR-NMR program of Mombourquette *et al.* (1996) was used for all data analysis, including angle corrections by iterations, fitting of the spin Hamiltonian parameters and spectral simulations.

2.3 FUNDAMENTAL PRINCIPLE OF EPR

Atoms and molecules both have electrons that surround their nuclei with specific orbitals; and these electrons also possess intrinsic angular momentum which is known

as their “spin”. Because the electron is electrically charged, there is a magnetic field associated with the spinning electron. In other words, the electron, by virtue of its intrinsic angular momentum, can be considered equivalent to a tiny bar magnet (Atkins and Symons 1967). In free space these magnets are aligned randomly, but in the presence of an external applied magnetic field there will be a preferred direction.

Commonly, according to the Pauli Exclusion Principle, if two electrons occupy the same sub-orbital to form magnetically neutral pairs in atoms and molecules (one electron spins clockwise, and the other electron spins anti-clockwise), the energy of their spins would counteract each other, and no net magnetic moment of their spins is present due to the neutralizing effects of the pairing of electron spins. Natural or artificial radiation ionizes atoms or molecules, i.e., breaks the paired electron. When the ionized electron is trapped by some other atoms, an electron-excess atom and an electron-deficient atom are formed: the former and the latter, both with an unpaired electron, are called “trapped electron’’ and “trapped hole” centers, respectively. So, when there is only one electron occupying the electron sub-orbital, the spin quantum number is 1/2, producing a net magnetic moment μ_e ($\mu_e = -g_e\beta_e S$, where g_e and β_e are the g factor of the free electron and is equal to 2.0023 and the Bohr magneton [$\beta_e = 0.927\times10^{-23}JT^{-1} = 0.927\times10^{-20}$ $ergG^{-1}$] for the electron, respectively, and S is the electron magnetic quantum number).

When there is no external magnetic field, the two spin energy levels are degenerate. Once the external magnetic field B is applied, a lower energy state (m_s = +1/2) occurs in which the electrons are lined up with the magnetic field and a higher

energy state (m_s = -1/2) corresponds to electrons lined up in opposition to the magnetic field. The degeneracy is lifted. The interaction between the magnetic moment from the unpaired electron(s) and the external magnetic field is called the Zeeman Effect. The difference in energy (ΔE) between the two electron spin levels is proportional to the external field:

$$\Delta E = g\beta B$$

By varying the static field B, one may change the energy-level separation, as indicated by Figure 2-3.

If a microwave of specific energy enters the system, resonant absorption will occur when the gap between two energy levels is equal to the energy of the microwave emitted:

$$\Delta E = h\nu = g\beta B$$

where h is Planck's constant, ν is microwave frequency. By means of this equation, the value of g factor is dimensionless and can be taken as a parameter which determines the position of the resonance absorption signal in the EPR spectrum and represents the sole value associated with the characteristics of the substance.

Looking at the spectra, it is clear that there are three features which differ from spectrum to spectrum. The first is that resonances for a given microwave frequency do not always occur at the same magnetic field strength (g factor). Secondly, it is rare for spectra to consist of only a single line. Extra lines may be due to other species with different g-values but there is also a mechanism which can give rise to a multiplet spectrum for a single species if it contains magnetic nuclei (nuclear hyperfine

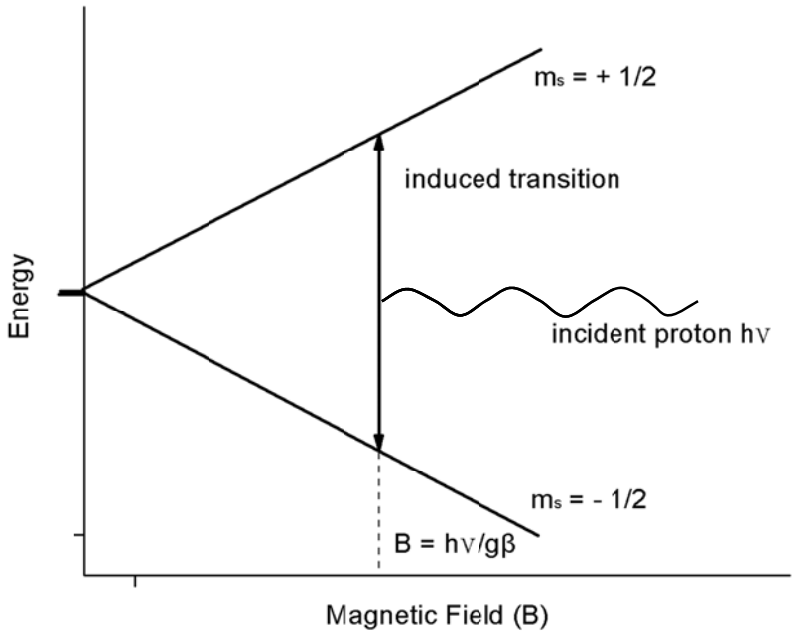

Figure 2-3 The effect of an external magnetic field upon the energy of an electron and the transition induced by an electromagnetic field.

interaction). The third property of the spectrum is the width of the absorption lines.

2.4 THE SPIN HAMILTONIAN

The spin Hamiltonian is a quantum mechanical expression for the energy of the particular electron or hole whose EPR spectrum is to be observed. It is composed of a number of terms representing the Zeeman interaction "g" (the interaction of the electron magnetic moment with the external applied magnetic field), the nuclear hyperfine interaction "A" (the interaction of the electron magnetic moment with the magnetic moments of nearby nuclei), the nuclear quadrupole interaction "P", the electron quadrupole interaction "D" and various high-spin interactions (i.e., fourth-degree parameters S^4 and I^4, and higher-order parameters which are very small or not relevant to this work and will not be enumerated here). Each of these terms involves the quantum mechanical operators for the components of electron spin resolved along three mutually orthogonal directions; the hyperfine term also involves operators of nuclear spin (Griscom 1974).

In general, these parameters can all occur simultaneously for any given paramagnetic species. An EPR spectrum measures the energy absorbed during the stimulated inversion of an electron spin in a magnetic field; thus to describe the EPR spectra, it is necessary to add together all of the possible terms in one center into a single spin Hamiltonian, which fully describes the behavior of the electron spin in the paramagnetic ion of a crystal in a magnetic field:

$$H_S = \beta_e \mathbf{B} \bullet \mathbf{g} \bullet \mathbf{S} + \mathbf{S} \bullet \mathbf{D} \bullet \mathbf{S} + \sum_{i=1}^{n} (\mathbf{S} \bullet \mathbf{A}_i \bullet \mathbf{I}_i - g_{ni} \beta_n \mathbf{B} \bullet \mathbf{I}_i + \mathbf{I}_i \bullet \mathbf{P}_i \bullet \mathbf{I}_i + \cdots)$$

where β_e and β_n are the electron and nuclear magneton, respectively; **S** and **I** are the electron spin and nuclear spin operators, respectively; **g** is the Zeeman electron term; $\mathbf{B_0}$ is the external magnetic field; and **A** and **P** are the hyperfine and quadrupole terms for the nucleus.

The spin-Hamiltonian equation encountered for any electron spin and N nuclear spins, all contributing to the spectrum. Which terms must be included to analyze any given spectrum is a matter of judgment and experience, added to an understanding of the chemical system being investigated. The correct spin Hamiltonian yields the observed positions and relative intensities of the lines (Weil and Bolton 2007).

2.4.1 The g factor

g factor of an EPR signal is used to characterize the resonance point position, which is determined by the field value giving rise to resonance. This parameter is a quantity characteristic of the molecule where the unpaired electron is located, providing information about the orbit that the unpaired electron occupies and local symmetry of paramagnetic defects. So the knowledge of the g-factor can give information about a paramagnetic center's electronic structure.

If the unpaired electron stays on the ground state as a free electron, the "g" value for that is called "g_e", which is equal to 2.0023.

In a single crystal, because of the 3-dimensional structure of paramagnetic defects in the local crystal symmetry, a g matrix is required to describe the spin Hamiltonian for centers.

When an EPR measurement is taken to determine the local structural information of paramagnetic defects in a single crystal, an experimental coordinate system must be chosen. Commonly the X, Y, and Z axes are used in the orthogonal coordinate system and these axes are not necessarily coincident with the crystallographic axes. So, the external magnetic field B is $B\cos\theta_x$, $B\cos\theta_y$, $B\cos\theta_z$. Here, θ_x, θ_y and θ_z are the orientations of the radical between the magnetic field B and the experimental X, Y, Z axes. If there is only the Zeeman term in a spin Hamiltonian, it will become:

$$H=\beta_e[\, B\cos\theta_x,\, B\cos\theta_y,\, B\cos\theta_z]\hat{g} \begin{vmatrix} S_x \\ S_y \\ S_z \end{vmatrix}$$

Here, $\hat{g}=\begin{vmatrix} g_{xx} & g_{xy} & g_{xz} \\ g_{yx} & g_{yy} & g_{yz} \\ g_{zx} & g_{yz} & g_{zz} \end{vmatrix}$

we adopt the definition $\mathbf{gg} \equiv \mathbf{g} \cdot \mathbf{g}^T$. Even if **g** is asymmetric, **gg** is always symmetric. Thus we need write explicitly only the diagonal and upper off-diagonal elements. It is possible to transform it to a diagonal form. This is accomplished by finding a matrix **C** such that:

$$\begin{pmatrix} C_{Xx} & C_{Xy} & C_{Xz} \\ C_{Yx} & C_{Yy} & C_{Yz} \\ C_{Zx} & C_{Zy} & C_{Zz} \end{pmatrix} \cdot \begin{pmatrix} (gg)_{xx} & (gg)_{xy} & (gg)_{xz} \\ & (gg)_{yy} & (gg)_{yx} \\ & & (gg)_{zz} \end{pmatrix} \cdot \begin{pmatrix} C_{Xx} & C_{Yx} & C_{Zx} \\ C_{Xy} & C_{Yy} & C_{Zy} \\ C_{Xz} & C_{Yz} & C_{Zz} \end{pmatrix} = \begin{pmatrix} (gg)_X & & \\ & (gg)_Y & \\ & & (gg)_Z \end{pmatrix}$$

$$\mathbf{C} \qquad\qquad \mathbf{gg} \qquad\qquad \mathbf{C}^T \qquad\qquad d_{\mathbf{gg}}$$

Take the positive square root of each diagonal element of $d_{\mathbf{gg}}$, the obtained results g_x, g_y and g_z are the three principal g values. The components of **C** are in fact the direction cosines connecting the principle axes x, y, z of the paramagnetic defect with the laboratory axes X, Y, Z. Once the principal values of **gg** are found, we can obtain

the matrix **g** itself. The method is to take the positive square root of each diagonal element of d_{gg} and then to change the resulting diagonal matrix d_g back to the laboratory coordinate system by using the reverse ($\mathbf{g} = \mathbf{C}^T \bullet d_g \bullet \mathbf{C}$) of the similarity transformation. The resulting symmetric matrix **g** reproduces the experimental data (line positions and intensities, Weil and Bolton 2007).

In a rigid medium, preferably in single crystal, g anisotropy should be considered. In general, g_{zz} can be denoted $g_{//}$, and $g_{\perp}=g_{xx}=g_{yy}$ in the case of axial symmetry. In the orientation-independent (isotropic) conditions, the g factor is represented by a single value, but these three values are different for a rhombic symmetry.

2.4.2 The Nuclear Hyperfine (hf) Interaction Parameter A

The nuclear hyperfine interaction is the mechanism which accounts for the multiplet character of some of the spectra. Analogous to the case of an electron spin, many nuclei of paramagnetic atoms or ions also have a magnetic moment (i.e., its spin quantum number I is non-zero) if there is an odd number of protons and/or neutrons and produce a magnetic field in the vicinity. In a molecule containing one or more magnetic nuclei with a non-zero nuclear spin, the unpaired electron nearby will experience not only the externally applied field, but also that from the magnetic nuclei. The nuclear fields do not displace the spectrum but produce a further small splitting of the energy levels of the unpaired electrons. This leads to the phenomenon of hyperfine splitting (hfs), splitting the individual EPR resonance signal into multiplets (a number of components centered about the position at which the resonance would have

occurred had there been no hyperfine interaction). In a word, the "A" parameter arises from the interaction between the spin magnetic moment of unpaired electron(s) and those of neighboring nuclear spin.

There are three common mechanisms by which electrons and nuclei interact: Fermi contact interaction, dipolar interaction and spin polarization.

If the electron and nuclear magnetic dipoles were to behave classically and a substantial externally applied static magnetic field B // z is present so as to align them. The dipoles are separated by the distance r, and θ is the angle between B and the line joining the two dipoles. Depending on the value of θ, the local field B_{local} caused by the nucleus at the electron can either aid or opposes the external magnetic field. It is apparent that B_{local}, arising from the nucleus, depends markedly on the instantaneous value of θ (and of r), which is known as dipolar interaction and is anisotropic.

By examining the radial dependence of the hydrogen orbital, it is clear that only electrons in s orbitals have a non-zero probability density at the nucleus; p, d, f, … orbitals all have nodes at the nucleus. By virtue of the spherical symmetry of s orbitals, the hyperfine interaction in this case is of course isotropic, which is known as the Fermi contact interaction (Weil and Bolton 2007).

In a word, Fermi contact interaction applies largely to the case of isotropic interactions (independent of sample orientation in a magnetic field); whereas dipolar interaction to the case of anisotropic interactions (spectra dependent on sample orientation in a magnetic field). Spin polarization is especially important for π-electron radicals.

For lower than cubic site symmetries in a crystal an anisotropy of the hyperfine splitting constants A is observed for which principal values can be determined. They can be decomposed into their isotropic and anisotropic parts:

$A_{zz} = A_{iso} + 2B$

$A_{yy} = A_{iso} - B - C$

$A_{xx} = A_{iso} - B + C$

where $C < B$ and $C \neq 0$ for uniaxial site symmetries.

Strictly speaking, hyperfine interaction parameters have dimensions of energy, but it is common practice to quote "A values" as magnetic fields. It should be understood that the quoted numbers are real $A_i/g_i\beta$ (assuming the principal axes of the A and g matrix are co-parallel).

For a nucleus of spin I, the nuclear spin splits every energy level of the unpaired electron into (2I+1) levels with the external magnetic field. That makes the spectrum show a multiplet consisting of (2I+1) lines of equal intensity and (at least for sufficiently large Zeeman splitting) approximately equidistant components to a first approximation. The energy separation between these components is referred to as the hyperfine coupling constant.

A more complex situation arises when the same unpaired electron, which exhibits spectra with hyperfine structure owing to the interaction with its nearest neighboring nucleus, can also interact with the nuclei of the next nearest-neighboring atoms, if these nuclei are magnetic. In such cases, an additional splitting of each hyperfine structure line will be observed, which is called superhyperfine structure

(shfs). This splitting is mostly unresolved and generally contributes to the broadening of the EPR signals. For example, if nucleus A has a spin of I_A then the unpaired electron experiences a field which is the vector sum of the field applied and the nuclear field. If there is another nucleus B present with spin I_B the field experienced is the sum of all three fields. Thus, if $I_A \neq I_B$, the spectrum will show a multiplet consisting of $(2I_A+1)(2I_B+1)$ absorption lines. If all the nuclei are equivalent, particularly symmetric patterns are obtained. For example, N equivalent protons (with nuclear spin of I_C) give rise to $(2NI_C+1)$ lines with an intensity ratio distribution according to the binomial law.

Both the magnitude of the HFS and SHFS are a direct measure of the degree of interaction between the unpaired electron and the perturbing nuclei, and can be related to the probes of the nature of the chemical bond in minerals (degree of ionic or covalent character of metal-ligand bonds).

2.4.3 The Nuclear Quadrupole Interaction Parameter P

The nuclear spin angular momentum direction is linked to the actual shape of the nucleus, that is, to the axis of symmetry of its electrical charge distribution. When a nucleus has a nuclear spin $I > 1/2$, any electric field gradient acting on that nucleus can orient its charge ellipsoid and hence its spin direction. Such a gradient is caused primarily by the electron distribution in the immediate neighborhood. Thus this tendency to align the nucleus affords a means of examining the relative shapes and potency of the atomic orbitals centered at the nucleus in question. Electron populating

s orbitals cannot act in this fashion, due to their sphericity. Of the non-s orbitals, p orbitals are more effective than d orbitals with the same principal quantum number.

The energy of alignment, called the nuclear quadrupole energy. Analysis of it reveals that the local electric-field gradient splits the nuclear-spin state energies already at zero magnetic field B.

There is a competition to align the nuclear spin by several agents, the local electric-field gradient, the local magnetic field originating from the unpaired electron (s), and the externally applies field. These complications must be dealt with when analyzing EPR spectra of solids which containing nuclei with $I > 1/2$ (Weil and Bolton 2007).

2.4.4 The Electronic Quadrupole Parameter D

When there is more than one unpaired electron in a center ($S > 1/2$), such energy contributions are also present in EPR work.

For the case of two electrons ($S = 1$) there are four spin states, which separates in energy into a triplet and a singlet state by the electron-exchange interaction. In addition to electron exchange, there exists another important interaction, also quadratic in the electron spin, namely the anisotropic magnetic dipole-dipole interaction. This interaction causes the three-fold degeneracy of the triplet state to be removed even in zero magnetic field; the latter effect often is called zero-field splitting (Weil and Bolton 2007). For the system $S > 1$, situation is similar but more complicated.

There is an important theorem (Kramer Theorem): if the system contains an odd number of unpaired electrons (S = 1/2, 3/2, 5/2, …), each energy level at least to maintain the two-fold degeneracy in zero field; for systems with an even number of unpaired electrons (S = 1, 2, 3, …), the resonance absorption may not be seen in the spectrum, if the degeneracy is completely lifted and the zero-field splitting is large.

The dipole-dipole interaction for the coupling of two unpaired electrons is analogous to the corresponding interaction between electronic and nuclear magnetic dipoles, which gives rise to the anisotropic hyperfine interaction. The difference is that the electron spin magnetic moment is 1836 times larger than the nuclear spin magnetic moment, so the dipole-dipole interaction is thousands of times stronger than the hyperfine interaction; the splitting of the absorption lines in spectrum produced by dipole-dipole interaction is also much larger than the hyperfine splitting.

2.5 LINE WIDTH AND LINE SHAPE

The line width and the line shape are also useful information in EPR spectrum.

2.5.1 Line width

For different samples, the line width can be different, and some to a few hundred Gauss wide, some narrow to 0.1 Gauss. So why can line width have such a big difference? In fact, there are two reasons for line broadening: spin-lattice interaction and spin-spin interaction. Define a physical parameter – relaxation time T, that is,

$$\Delta H = \hbar/g\beta\ (1/T)$$

where ΔH is the actual observed line width, T is the relaxation time. Here, T can be

written as:

$$1/T = 1/2T_1 + 1/T_2$$

here, T_1 is known as the "spin-lattice relaxation time", T_2 is called "spin-spin relaxation time".

(a) Spin-Lattice Relaxation

The spin-lattice relaxation process depends upon fluctuating magnetic fields close to the unpaired electron. Such fields may, for example, be due to lattice vibrations causing the oscillation of local electrically charged particles. Such fluctuating fields can couple with the spin magnetic moment of the electron and hence induce transitions. That is, the spin energy is dissipated at lattice phonons. Because of the induced emission the length of time which the particular spin spends in the upper state is reduces; by the uncertainty principle the energy of that state becomes less well defined and therefore the resonance line is broadened.

(b) Spin-Spin Relaxation

The spin-spin relaxation process depends on local magnetic nuclei or unpaired electrons affecting the field at the unpaired electron. A random distribution of such fields will blur the energy levels of the unpaired electron and the line will be broadened by the mechanism also (Atkins and Symons 1967).

2.5.2 Line shape

The shapes of EPR lines are usually described by either Lorentzian or Gaussian line shapes. The expected line shape of the resonance line is Lorentzian, if there is no hyperfine broadening. A Gaussian shape arises from the statistical distribution of the

spin magnetic moments, resulting in a dipolar (inhomogeneous) broadening. If the concentration of paramagnetic centers is low and if there is dynamic averaging, say in liquid solution, lines often approach the Gaussian shape if the line is a superposition of many components. One usually refers to such composites as inhomogeneous broadened. The intersection of the first derivative with the zero line corresponds to the resonance value of the magnetic field, the line width being measured between inflection points.

2.6 REFERENCES

Atkins, P.W., Symons, M.C.R. (1967): The structure of inorganic radicals: an application of electron spin resonance to the study of molecular structure. Elsevier Publishing Company.

Bersohn, M., Baird, J.C. (1966): An introduction to electron paramagnetic resonance. Benjamin.

Griscom, D.L. (1974): ESR studies of radiation-damage and structure in oxide glasses not containing transition group ions: a contemporary overview with illustrations from the alkali borate system. *Journal of Non-crystalline Solids*, **13**: 251-285.

Ikeya, M. (1993): New applications of electron spin resonance: dating, dosimetry and microscopy. World Scientific.

Marfunin, A.S. (1979): Spectroscopy, luminescence and radiation centers in minerals. Springer-Verlag.

Mombourquette, M.J., Weil, J.A., McGavin, D.G. (1996): EPR-NMR User's Manual. Department of Chemistry, University of Saskatchewan, Saskatoon, Saskatchewan.

Vassilikou-Dova, A.B., Lehmann, G. (1987): Investigations of minerals by electron paramagnetic resonance. *Fortschritte der Mineralogie*, **65**: 173-202.

Weil, J.A., Bolton, J.R. (2007): Electron paramagnetic resonance: elementary theory and practical applications. Wiley-Interscience.

Zavoisky, E. (1945): Spin-magnetic resonance in paramagnetics. *Journal of Physics. E. Scientific Instruments*, **9**: 245-249.

CHAPTER 3

Single-crystal EPR and DFT studies of a $[BO_4]^0$ center in datolite: Electronic structure, formation mechanism and implications

A natural datolite $CaBSiO_4(OH)$ (Bergen Hill, New Jersey, USA), before and after gamma-ray irradiation (up to ~70 kGy), has been investigated by single-crystal and powder electron paramagnetic resonance (EPR) spectroscopy from 10 K to 295 K. EPR spectra of gamma-ray-irradiated datolite show the presence of a boron-associated oxygen hole center (BOHC) and an atomic hydrogen center (H^0), both of which grow with the increase of the radiation dose. The principal g and A(^{11}B) values of the BOHC at 10 K are: g_1=2.04817(3), g_2=2.01179(2), g_3=2.00310(2), A_1= –0.401(7) mT, A_2= –0.906(2) mT, A_3= –0.985(2) mT, with The orientations of the g_1 and A_1 axes are approximately along the B–OH bond direction. These experimental results suggest that the BOHC represents hole trapping on the hydroxyl oxygen atom after the removal of the hydrogen atom (i.e. a $[BO_4]^0$ center): via a reaction $O_3BOH \rightarrow O_3BO\bullet + H^0$, where $\bullet$ denotes the unpaired electron. Density functional theory (DFT) calculations (CRYSTAL06, B3PW, all-electron basis sets, and 1×2×2 supercell) support the proposed structural model and yield the following ^{11}B hyperfine coupling constants: A_1= –0.429 mT, A_2= –0.901 mT, A_3= –0.954 mT, in excellent agreement with the experimental results. The $[BO_4]^0$ center undergoes the onset of thermal decay at ~200 ºC and is completely annealed out at 375 ºC but can be restored readily by gamma-ray irradiation. Isothermal annealing experiments show that the $[BO_4]^0$ center

exhibits a second-order thermal decay with an activation energy of 0.96 eV. The confirmation of the $[BO_4]^0$ center (and its formation from the O_3BOH precursor) in datolite has implications for not only understanding of BOHCs in alkali borosilicate glasses but also their applications to nuclear waste disposal.

3.1 INTRODUCTION

Radiation-induced defects (RIDs) such as boron-associated oxygen hole centers (BOHCs) in borate and borosilicate glasses have long been the subject of intensive experimental and theoretical investigations, because they exert profound influences on various properties of these important materials for diverse applications from fiber optics to radiation dosimetry and nuclear waste disposal (Yasaitis and Smaller 1953; Lee and Bray 1963; Griscom *et al.* 1968; Shkrob *et al.* 2000; Shkrob and Tarasov 2000; Porwal *et al.* 2005; Kordas 1999, 2003, 2005; Kadam *et al.* 2008; Kordas and Goldfarb 2008; Mohapatra *et al.* 2009). For example, alkali borosilicate glasses have been the matrix of choice for confinement of high level nuclear wastes in several countries (Weber *et al.* 1997; Shkrob *et al.* 2000; Deschanels *et al.* 2007; Parkinson *et al.* 2007; Mohapatra *et al.* 2009). Therefore, knowledge about microscopic processes for the formation and evolution of RIDs in alkali borosilicate glasses is of vital importance to the effective processing, immobilization and safe storage of high level nuclear wastes (Weber *et al.* 1997; Shkrob *et al.* 2000; Parkinson *et al.* 2007; Mohapatra *et al.* 2009).

Electron paramagnetic resonance (EPR) spectroscopic studies of BOHCs in

borate and borosilicate glasses dated back to 1950's (Yasaitis and Smaller 1953; Lee and Bray 1963; Griscom *et al.* 1968). However, questions concerning the atomic and electronic structures of BOHCs in glasses remain (Shkrob *et al.* 2000; Carboni *et al.* 2003; Kordas and Goldfarb 2008). In this context, single-crystal EPR studies of analogous centers in minerals are particularly informative (Eachus and Symons 1968; Bershov and Martirosyan 1970; Misra *et al.* 1983; Novozhilov *et al.* 1988; Shkrob and Tarasov 2000; Walsby *et al.* 2000; Table 3-1). For example, Bershov and Marfunin (1981) classified BOHCs in minerals into three types: (1) $[BO_4]^0$ formed from hole trapping by $[BO_4]^{5-}$ substituting for $[SiO_4]^{4-}$ in silicates, (2) $[BO_3]^{2-}$ from $[BO_3]^{3-}$ for $[CO_3]^{2-}$ in carbonates, and (3) $[BO_2]^0$ from $[BO_4]^{5-}$ for $[SO_4]^{2-}$ in sulfates (Table 3-1).

Of these three types, $[BO_3]^{2-}$ is by far the best studied (Eachus and Symons 1968; Shkrob and Tarasov 2000) and has generally been accepted as the most prevalent BOHC in borate and borosilicate glasses (Taylor *et al.* 1971; Griscom 1993; Shkrob *et al.* 2000; Kordas 2003, 2005; Kordas and Goldfarb 2008; Kadam *et al.* 2008). The $[BO_4]^0$ type (Lee and Bray 1963; Bershov and Marfunin 1967, 1981; Misra *et al.* 1983), on the other hand, has received much less attention, and its existence has been called into question (Shkrob and Tarasov 2000; Pacchioni *et al.* 2001). For example, Shkrob and Tarasov (2000), on the basis of combined electron spin echo envelope modulation (ESEEM) experiments and modified neglect of differential overlap (MNDO) calculations, suggested that the previously proposed $[BO_4]^0$ centers in

Table 3-1 Summary of boron-oxygen hole centers (BOHCs) in minerals

Mineral	Center	Principal *g*-factor values			Principal $A(^{11}B)$ values (mT)			Radiation (T)	References
		g_1	g_2	g_3	$A_1/g_e\beta_e$	$A_2/g_e\beta_e$	$A_3/g_e\beta_e$		
Calcite	$[BO_3]^{2-}$	2.0080	2.0127	2.0127	–1.26	–0.84	–0.84	γ-ray, 4.2 K	Eachus and Symonns (1968)
Calcite	$[BO_3]^{2-}$	2.008	2.009	2.014	1.23	0.92	0.82	γ-ray, 77 K	Bershov and Marfunin (1981)
Calcite	$[BO_2]^0$	2.0080	2.0086	2.0149	1.315	0.978	0.878	X-ray, 77 K	Bacquet *et al.* (1974)
Anhydrite	$[BO_2]^0$	2.0086	2.0122	2.0120	1.17	0.90	0.92	γ-ray, 290 K	Bershov and Marfunin (1981)
Anhydrite	$[BO_2]^0$	2.0076	2.0118	2.0116	1.24	0.99	0.99	γ-ray, 77 K	Bershov and Marfunin (1981)
					0.41*	0.32*			
Datolite	$[BO_4]^0$	2.0059(5)	2.0066(5)	2.0512(5)	0.92(5)	0.63(5)	0.46(5)	Natural, 77 K	Bershov and Matrirosyan (1970)
Danburite	$[BO_4]^0$	2.0059(5)	2.0066(5)	2.0481(5)	0.96(5)	0.94(5)	0.49(5)	Natural, 77 K	Bershov and Matrirosyan (1970)
Danburite	I	2.0024(9)	2.0103(9)	2.0465(9)	0.96(10)	1.04(10)	0.54(10)	X-ray, 77 K	Misra *et al.* (1983)
Danburite	II	2.0026(9)	2.0099(9)	2.0465(9)	0.96(10)	1.04(10)	0.54(10)	X-ray, 77 K	Misra *et al.* (1983)
Danburite	III	2.0021(9)	2.0101(9)	2.0465(9)	0.92(10)	1.00(10)	0.50(10)	X-ray, 77 K	Misra *et al.* (1983)
Danburite	IV	2.0020(9)	2.0101(9)	2.0464(9)	0.92(10)	1.04(10)	0.50(10)	X-ray, 77 K	Misra *et al.* (1983)
Danburite	V	2.0016(9)	2.0115(9)	2.0506(9)	0.89(10)	1.00(10)	0.54(10)	X-ray, 77 K	Misra *et al.* (1983)
Danburite	VI	2.0014(9)	2.0170(9)	2.0508(9)	0.89(10)	1.04(10)	0.68(10)	X-ray, 77 K	Misra *et al.* (1983)
Danburite	VII	1.9981(9)	2.0202(9)	2.0471(9)	0.89(10)	1.04(10)	0.68(10)	X-ray, 77 K	Misra *et al.* (1983)
Danburite	I-IV	2.0057	2.0120	2.0495	0.94	1.03	0.52	γ-ray, 300 K	Novozhilov *et al.* (1988)
Danburite	VIII	2.0060	2.0196	2.0352	0.75	0.75	0.52	γ-ray, 300 K	Novozhilov *et al.* (1988)
Zircon	$[BO_4]^0$	2.003859(2)	2.012714(2)	2.047430(2)	–0.4884(3)	–0.5193(2)	–0.1904(3)	X-ray, 15 K	Walsby *et al.* (2000)

*, Hyperfine constants of ^{10}B.

danburite (Bershov and Martirosyan 1970; Misra *et al.* 1983; Novozhilov *et al.* 1988) originate from strongly distorted B–O–B linkages, in which one of the B–O bonds is elongated and the B atom is relaxed towards the three-oxygen plane to form a BO_3 group. Shkrob and Tarasov (2000) concluded that the hole of BOHCs in danburite is trapped in the 2*p* orbital of the non-bridging oxygen atom of the BO_3 group, hence representing a $[BO_3]^{2-}$ center. Walsby *et al.* (2000) acknowledged that their proposed $[BO_4]^0$ center in B-doped zircon has unexplained differences in comparison with the well-established $[AlO_4]^0$ center (Claridge *et al.* 1994). Pacchioni *et al.* (2001), on the basis of density functional theory (DFT) calculations, showed that a center of the $[BO_4]^0$ type is not stable in B-doped SiO_2.

In this contribution, we report on the results of a combined EPR and DFT study of a BOHC in datolite $CaBSiO_4(OH)$. The datolite structure consists of sheets of four- and eight-membered rings of alternating SiO_4 and $BO_3(OH)$ tetrahedra, with the sheets linked together by CaO_8 Thomson cubes (Fig. 3-1; Foit *et al.* 1973; Ivanov and Belokoneva 2007). Our single-crystal EPR data reported herein show that the BOHC in datolite has significantly different ^{11}B hyperfine constants from its counterpart reported by Bershov and Martirosyan (1970). Moreover, our experimental data and theoretical results allow us to confirm the BOHC center in datolite as the $[BO_4]^0$ type. In addition, the EPR spectra of gamma-ray-irradiated datolite show that the $[BO_4]^0$ center is accompanied by an atomic hydrogen center. Radiation-dose-dependence experiments allow us to not only establish the precursor of the $[BO_4]^0$ center but also determine its formation mechanism. Also, isochronal and isothermal annealing

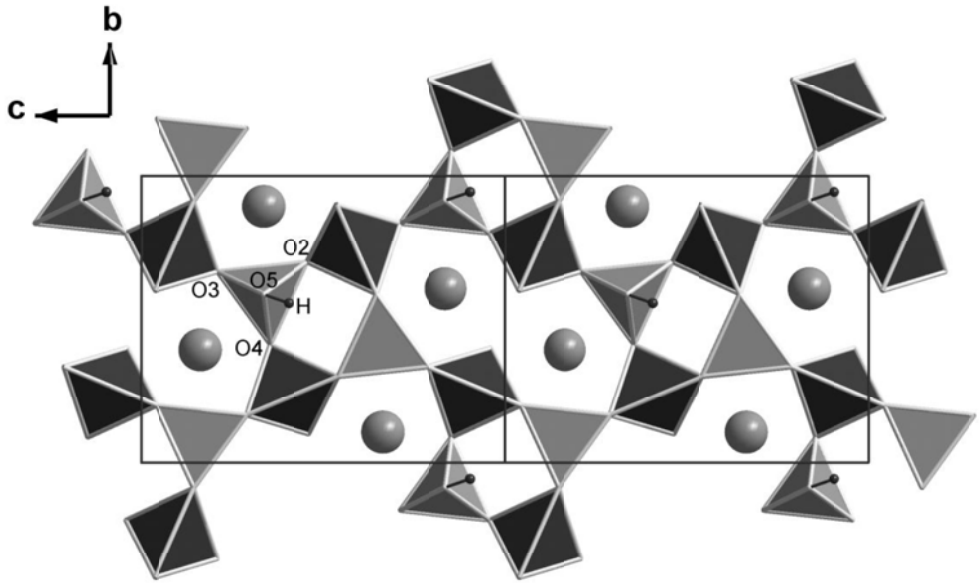

Figure 3-1 Structure of datolite projected to the (100) plane. Labels of the oxygen atoms of a BO_4 tetrahedron after Foit *et al.* (1973).

experiments provide information about the thermal stability and decay kinetics of the $[BO_4]^0$ center in datolite. These results for the $[BO_4]^0$ center in datolite are compared with other BOHCs in minerals and are discussed with relevance to the applications of borosilicate glasses for nuclear waste disposal.

3.2 SAMPLES, EXPERIMENTAL TECHNIQUES AND DFT CALCULATION

3.2.1 Datolite specimens and sample preparation

A suite of datolite samples from the University of Saskatchewan reference mineral collection was first investigated by reconnaissance single-crystal EPR studies. Subsequently, a sample from Bergen Hill (New Jersey, USA), which contains anhedral crystals of millimeters in size, was selected for detailed EPR measurements (see below). Specifically, several crystals (~1×1×2 mm) from this sample were chosen for single-crystal EPR measurements before and after gamma-ray irradiation. Other crystals were pulverized into powders for radiation-dose-dependence measurements and for isochronal and isothermal annealing experiments.

Gamma-ray-irradiation experiments were made at room temperature (~295 K) in a ^{60}Co cell with a dose rate of ~460 Gy/h. Thermal annealing experiments were made at atmospheric pressure in a Thermolyne muffle furnace. Isochronal annealing experiments (i.e. a constant duration of 10 minutes) were made sequentially on a gamma-ray-irradiated powder sample (~11.5 kGy) from 75 ºC to 400 ºC at a step of every 25 ºC. Isothermal annealing experiments at 200 ºC, 250 ºC, 300 ºC and 350 ºC were made on four gamma-ray-irradiated samples (~11.5 kGy).

3.2.2 EPR experiments

All EPR spectra were measured on a Bruker EMX spectrometer at the Saskatchewan Structure Sciences Centre, University of Saskatchewan, equipped with an automatic frequency controller, an ER4119 cavity, an ER218G1 goniometer with an angle uncertainty of ~0.2°, and an Oxford liquid-helium cryostat.

Reconnaissance single-crystal EPR measurements of datolite were made at various temperatures between 10 K and 295 K. Detailed single-crystal EPR spectra of gamma-ray-irradiated crystals (~3.2 kGy) from the Bergen Hill sample were collected for three rotation planes at 295 K and 10 K. Experimental conditions for spectral measurements at 295 K included a microwave frequency of ~9.36 GHz, modulation frequency of 100 kHz, modulation amplitude of 0.06 mT, microwave power of 2 mW, and spectral resolution of ~0.016 mT (i.e. 1,024 field data points over 16 mT). Experimental conditions at 10 K included a microwave frequency of ~9.40 GHz, modulation frequency of 100 kHz, modulation amplitude of 0.08 mT, and microwave power of 2 mW, and spectral resolution of ~0.01 mT (i.e. 1,024 field data points over 10 mT). At a few orientations, spectra for a scan range of 60 mT with a resolution of ~0.029 mT (i.e. 2,048 points over 60 mT) were also collected at both 295 K and 10 K. The angle intervals for all single-crystal measurements were 5°. Magnetic-field calibrations were made by use of the free radical α, γ-bis-diphenylene-β-phenyl allyl in benzene (BDPA; g = 2.0027) and the Bruker strong pitch (g = 2.0028) at 295 K and 10 K, respectively.

Powder EPR measurements were all made at 295 K by using ~200 mg samples in

amorphous silica tubes. Experimental conditions included microwave frequencies of ~9.38 GHz, modulation frequency of 100 kHz, modulation amplitude of 0.08 mT, microwave power of ~2 mW, and spectral resolutions of ~0.015 mT (i.e. 1,024 data points over a scan range of 15 mT) and ~0.029 mT (2,048 data points over 60 mT).

3.2.3 DFT calculations

DFT calculations used the supercell approach and hybrid functionals as implemented in CRYSTAL06 (Dovesi *et al.* 2006). All-electron basis sets used in this study are those known to be well-suited for periodic calculations and include the 86-511D21G of Valenzano *et al.* (2006) for Ca, the 8-41G** of Pisani *et al.* (1992) for Si, the 6-31G* of Gatti *et al.* (1994) for O, the [3s2p1] basis set with the d polarization function removed (Eichcorn *et al.* 1995) for H, and the def2-TZVP of Weigend and Ahlrichs (2005) for B, except that the diffuse functions with exponents <0.1 were left out along with the outmost d and the f functions to avoid linear correlation and integration problems in the calculations.

The thresholds for the overlap and penetration Coulomb integrals, the overlap for Hartree-Fock (HF) exchange integrals, and the two pseudo-overlaps for HF series were set to 10^{-7}, 10^{-7}, 10^{-7}, 10^{-7}, and 10^{-14} hartree, respectively, while a tight SCF tolerance of 10^{-7} hartree was chosen. These are all more accurate than the default values to improve the converged wave functions. The Pack-Monkhorst shrink factor for the single-cell geometry optimization was set to 8, giving a total of 170 *k* points in the irreducible Brillouin zone. The Fermi surface of the defect system is described by

the Gilat net (Dovesi *et al.* 2006) with the Pack-Monkhorst shrink factor doubled.

Calculations started with the construction and optimization of selected supercells (1×1×1, 1×2×2 and 2×2×1) for the perfect structure. Subsequently, defect was introduced to these optimized cells by removing one H atom from the O_3BOH group, and the whole structure was then fully optimized without any local symmetry restrictions. Also included in calculations was a 2×2×2 supercell, for which no geometry optimization was attempted. The ^{11}B hyperfine parameters (i.e. hyperfine coupling constants and nuclear quadrupole parameters) of the defect were obtained from each supercell calculation.

3.3 RESULTS

3.3.1 Single-crystal EPR spectra at 295 K

Reconnaissance single-crystal EPR spectra (now shown) reveal that datolite samples from various localities commonly contain a Fe^{3+} center, a Mn^{2+} center, and a quartet (i.e. four lines of approximately same intensity and equal spacing). The Fe^{3+} center (S = 5/2) is characterized by a strong peak at the effective g value of ~4.3, while the Mn^{2+} center is identified by the diagnostic ^{55}Mn hyperfine sextet (I = 5/2 and $A/g_e\beta_e$ = ~9 mT). The $^{55}Mn^{2+}$ sextet commonly shows significant overlaps with the quartet. Therefore, our investigation of the quartet led us to choose datolite crystals from the Bergen Hill sample, in which the Mn^{2+} center is not visible.

The quartet is invariably very weak in the spectra of as-is datolite but can be enhanced by gamma-ray irradiation. Spectra of gamma-ray-irradiated datolite also

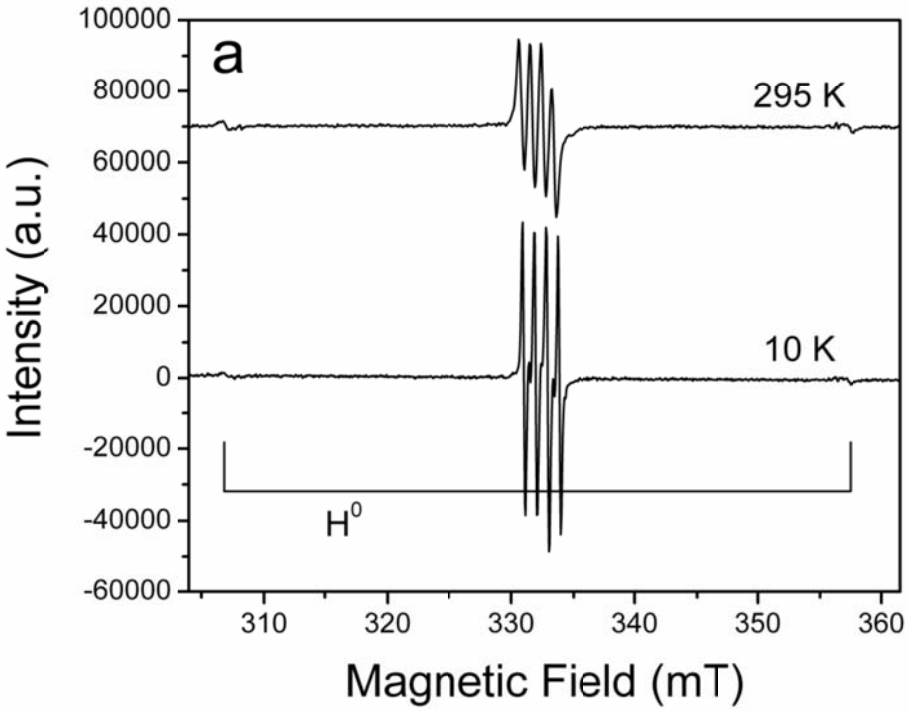

Figure 3-2a Representative single-crystal EPR spectra of gamma-ray-irradiated datolite measured at 295 K and 10 K with magnetic field approximately parallel to the crystallographic c-axis, showing the quartet ($[BO_4]^0$) and a doublet (H^0).

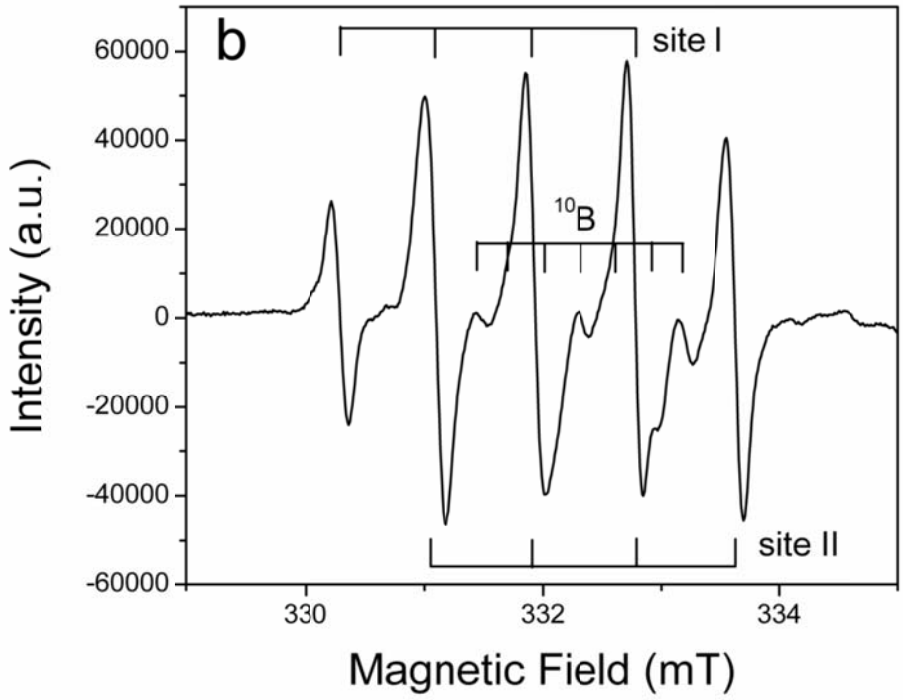

Figure 3-2b Representative single-crystal EPR spectra of gamma-ray-irradiated datolite measured at 10 K and crystal orientation at ($\theta = 49.1^{\circ}$, $\varphi = 25.4^{\circ}$), showing the quartet is split into two sets corresponding to two magnetically nonequivalent sites; also present are the weak lines attributable to hyperfine interaction with ^{10}B.

show a doublet with a separation of ~50 mT (Fig. 3-2a). This doublet, centered at the effective g value of ~2.00, is readily attributable to the atomic hydrogen center (H^0) on the basis of the characteristic ^1H hyperfine splitting. At a few orientations, the lines of the H^0 center occur as either irregular multiplets or narrowly spaced quartets of a total width of ~0.5 mT, suggesting a superhyperfine interaction with a neighboring nucleus of I = 3/2 (^{11}B?). However, the H^0 center is invariably low in intensity, even after ~70 kGy gamma-ray irradiation. Also, the H^0 center decays quickly at room temperature. Therefore, detailed measurements of the H^0 center were not attempted.

The quartet in all three rotation planes is split into at most two equivalent sets, although individual lines of these two sets commonly overlap. These spectral features are consistent with a single unpaired electron (S = 1/2) interacting with a nucleus with I= 3/2. The average line widths of individual peaks are ~0.25 mT. However, peak overlapping commonly results in significant line-broadening to as much as 0.5 mT.

3.3.2 Single-crystal EPR spectra at 10 K

Single-crystal EPR spectra of irradiated datolite measured at 10 K show that the average line width of the quartet, where peak overlapping is absent, is reduced to ~0.15 mT. At a few orientations, additional weak lines are now visible inside the quartet and are part of a seven-line feature (Fig. 3-2b). The splitting of the seven-line feature and the quartet have a constant ratio of ~0.333, which is in excellent agreement with the $g_n(^{10}B)/g_n(^{11}B)$ value = 0.335 (Morton and Preston 1978). Therefore, the strong quartet and the weak seven-line feature obviously arise from

hyperfine interactions with ^{11}B (I = 3/2, natural abundance of 80.1%) and ^{10}B (I = 3 and 19.9%), respectively. This result, together with calculated principal g values (see below), allows us to identify this center as a BOHC (Schirmer 2006). Unfortunately, the H^0 center remains weak in spectra measured at 10 K (Fig. 3-2a).

Figure 3-3 shows a representative roadmap of the BOHC in datolite at 10 K. Similar to those observed at 295 K, the quartet is split into at most two sets, while individual ^{11}B hyperfine lines commonly overlap between the two sets.

3.3.3 Spin-Hamiltonian parameters of the BOHC in datolite

The single-crystal EPR spectra of the BOHC in datolite can be described by a spin Hamiltonian of the form:

$$\boldsymbol{H_s} = \beta_e \mathbf{S} \bullet \mathbf{g} \bullet \mathbf{B} + \mathbf{I} \bullet \mathbf{A} \bullet \mathbf{S} + \mathbf{I} \bullet \mathbf{P} \bullet \mathbf{I} - g_n \beta_n \mathbf{I} \bullet \mathbf{B}$$

where β_e and β_n are the electron and nuclear magneton, respectively; **S** and **I** are the electron spin and nuclear spin operators, respectively; **g** is the Zeeman electron term; **B** is the external magnetic field; and **A** and **P** are the hyperfine and quadrupole terms for the ^{11}B nucleus. All data analyses, including angle corrections, optimization of spin-Hamiltonian parameters and spectral simulations, were made by use of the EPR-NMR software package of Mombourquette *et al.* (1996). The total numbers of line-position points from spectra measured at 295 K and 10 K were both 888. The corresponding sums of weighing factors were 486 and 566, respectively, when overlapping peaks (Figs 3-2b, 3-3) were assigned weighing factors of 0.1.

The software package EPR-NMR, which fits the spin-Hamiltonian parameters

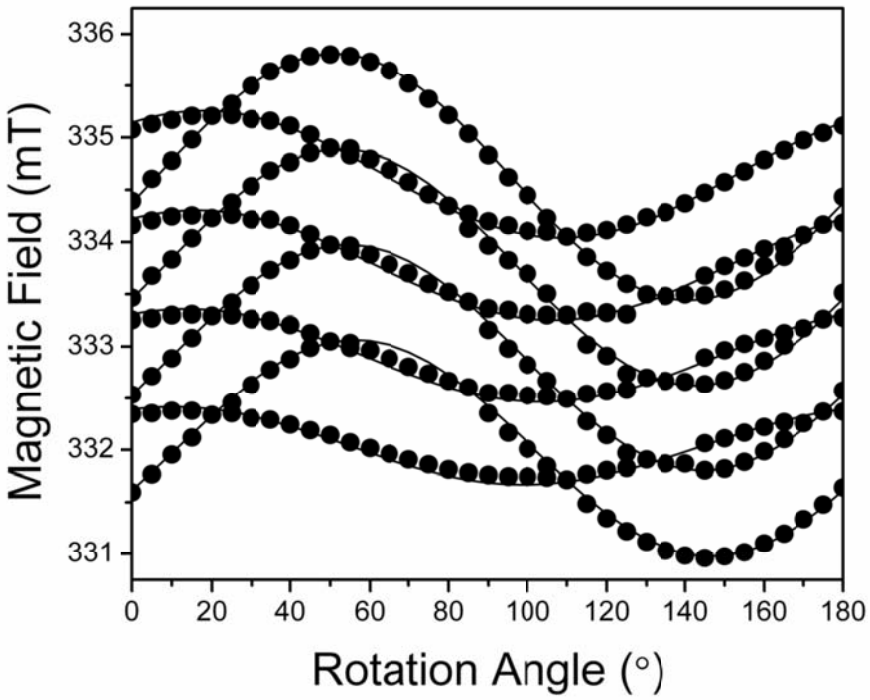

Figure 3-3 Line-position data versus rotation angle (i.e. roadmap) in a representative plane (the calculated plane normal $\theta = 81.7^{\circ}$ and $\varphi = 203.5^{\circ}$) measured at 10 K and ν = ~9.397 GHz: solid circles denote measured data points; solid lines represent predictions from spin-Hamiltonian parameters in Table 3-2.

and does angle corrections by iterations, has been proven to be capable of handling datasets without a "prior" knowledge of crystal orientation (Pan *et al.* 2008). This capability was crucial in this study, because the single-crystal spectra were measured on anhedral crystals. The calculated normals of the three rotation planes at 295 K are (θ = 52.1°, φ = 308.1°), (96.5°, 51.2°), and (84.1°, 333.0°), respectively. The normals of the three rotation planes at 10 K were (116.9°, 321.1°), (106.5°, 287.7°), and (81.7°, 203.5°), respectively. The final values of the root-mean-squares of weighted differences (RMSD) between the calculated and observed line positions at 295 K and 10 K were 0.055 mT and 0.042 mT, respectively. Both of these values are less than half of their respective average line widths. The signs of the hyperfine coupling constants cannot be determined from EPR data alone. Following previous experimental and theoretical results (Eachus and Symons 1968; Shkrob and Tarasov 2000; Pacchioni *et al.* 2001), we adopted a negative sign for the isotropic part of ^{11}B hyperfine. The nuclear quadrupole tensor *P*, which was included in the fitting of the 10 K dataset, was found to have a magnitude < 1% of the hyperfine constants and therefore cannot be determined precisely, and hence is not included in Table 3-2.

The fitted matrices **g** and **A**(^{11}B) at 295 K and 10 K are broadly similar (Table 3-2), and their small differences may be attributable to a minor temperature dependence in this range. Specifically, matrices **g** and **A**(^{11}B) are all only slightly off axial symmetry. The unique g_1 and A_1 axis are almost coaxial and are approximately along the <B–O5> direction (88.5°, 359.4°; Table 3-2). These results, including the negligible nuclear quadrupole effect (cf. Shkrob and Tarasov 2000), allow us to

Table 3-2 Spin-Hamiltonian parameters of the $[BO_4]^0$ center in γ-ray irradiated datolite at 10 K and 294 K

	Matrix (Y)			k	Principal values (Y_k)	Principal directions		RMSD (mT)
						θ_k(°)	φ_k(°)	
X-band EPR spectra at 10 K								
	2.04689(3)	–0.00698(2)	0.00200(1)	1	2.04817(3)	86.2(2)	350.6(2)	
G		2.00484(2)	–0.00257(1)	2	2.01179(2)	164.2(2)	67.3(2)	
			2.01134(1)	3	2.00310(2)	74.7(2)	81.6(2)	
	–0.424(7)	–0.109(3)	0.019(3)	1	–0.401(7)	88.0(3)	349.1(4)	0.042
A/$g_e\beta_e$		–0.962(2)	0.008(2)	2	–0.906(2)	171(3)	271(3)	
(mT)			–0.906(2)	3	–0.985(2)	98(3)	78(1)	
X-band EPR spectra at 295 K								
	2.04489(4)	–0.00499(2)	0.00212(2)	1	2.04572(4)	86.1(2)	352.1(2)	
G		2.00839(4)	–0.00185(1)	2	2.01130(2)	156.2(2)	73.3(2)	
			2.01078(2)	3	2.00705(4)	66.7(3)	83.8(2)	
	–0.462(11)	–0.049(3)	0.006(3)	1	–0.457(11)	89.3(3)	354.4(4)	0.055
A/$g_e\beta_e$		0.966(5)	0.012(2)	2	–0.926(3)	163(3)	263(1)	
(mT)			–0.930(3)	3	–0.975(5)	106(3)	84.2(4)	

θ_k and φ_k are the tilting angles from the crystallographic axes **c** and **a**, respectively.

identify this BOHC in datolite as a $[BO_4]^0$ center (see "Discussion" below).

3.3.4 Powder EPR spectra

Powder EPR spectra of as-is datolite show only a weak $[BO_4]^0$ signal, while those of gamma-ray-irradiated samples contain both the $[BO_4]^0$ center and the H^0 center. Figure 3-4 shows that the intensities of the $[BO_4]^0$ center and the H^0 center both grow with the increase of the irradiation time (i.e. gamma-ray dose).

Powder EPR measurements of the isochronally annealed datolite show that the $[BO_4]^0$ center remains essentially unaffected up to 175 °C but starts to decrease in intensity at 200 °C and is completely annealed out at 375°C (Fig. 3-5). The H^0center is bleached completely at 175°C. Gamma-ray irradiation (~11.5 kGy) restores the $[BO_4]^0$ and H^0 centers to ~69% and ~42% of their original intensities, respectively.

Powder EPR spectra of isothermally annealed datolite show that the decay of the $[BO_4]^0$ center does not follow a simple exponential law. Rather, the reciprocal of the normalized intensity (I_t/I_0; where subscripts *t* and *0* denote time *t* and 0 in seconds) correlates approximately linearly with the annealing time (Fig. 3-6a):

$$I_t/I_0 = 1 + \lambda t \qquad (3\text{-}2)$$

where λ is the specific decay constant at temperature T (K). This relationship suggests the thermal decay of the $[BO_4]^0$ center is of the second–order type (Ikeya 1993). Figure 3-6b shows that the specific decay constants calculated for the $[BO_4]^0$ center in the temperature range from 200°C to 350°C follow the Arrhenius relation:

$$\lambda = A\exp(-E/k_bT) \qquad (3\text{-}3)$$

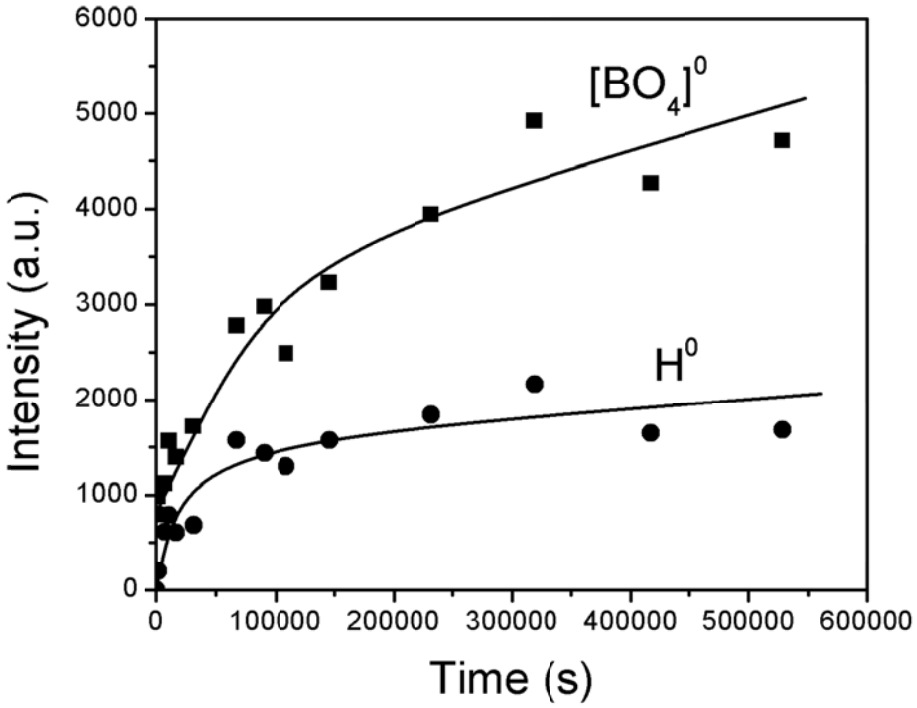

Figure 3-4 Plots of the intensities of the $[BO_4]^0$ and H^0 centers, measured as the peak-to-peak height in powder spectra, as a function of the gamma-ray-irradiation time (i.e., gamma-ray dose).

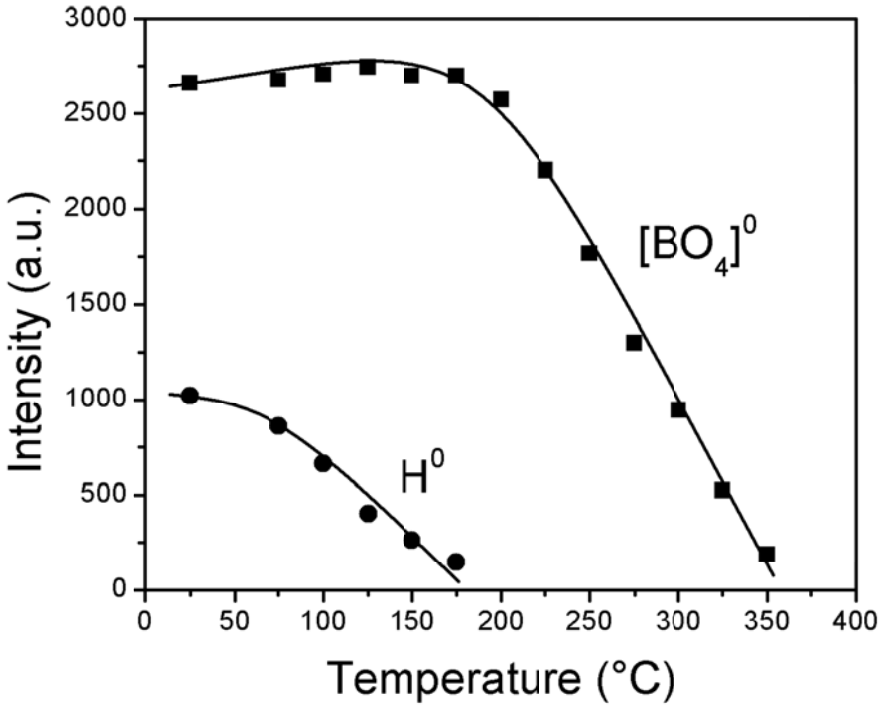

Figure 3-5 Intensities of the $[BO_4]^0$ and H^0 centers as a function of isochronal annealing temperature.

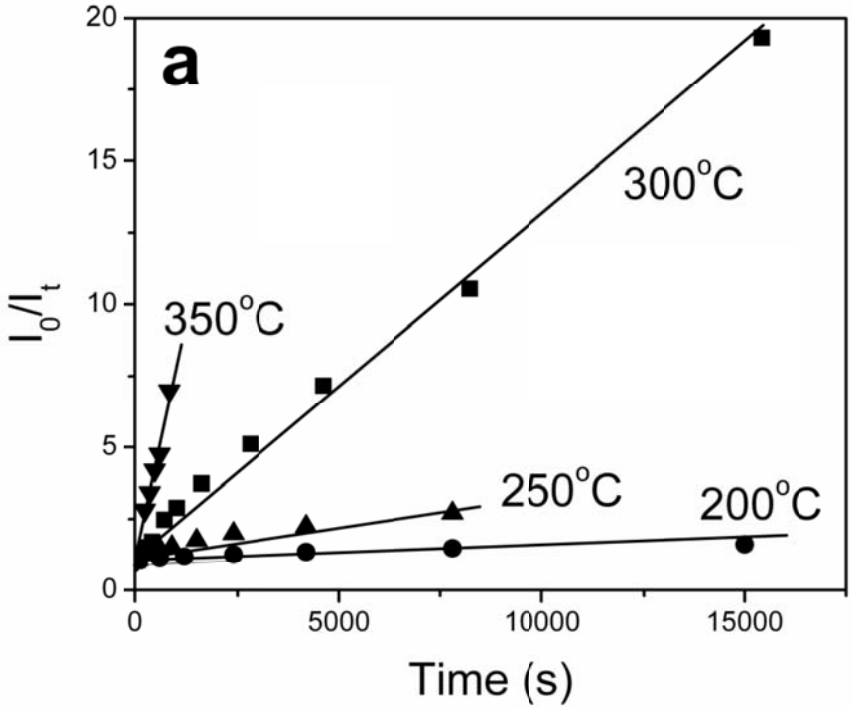

Figure 3-6a Plots of the reciprocal normalized intensity (I_0/I_t) versus annealing time (t) illustrating the second-order decay kinetics of the $[BO_4]^0$ center in datolite at 200 ℃, 250 ℃, 300 ℃, and 350 ℃.

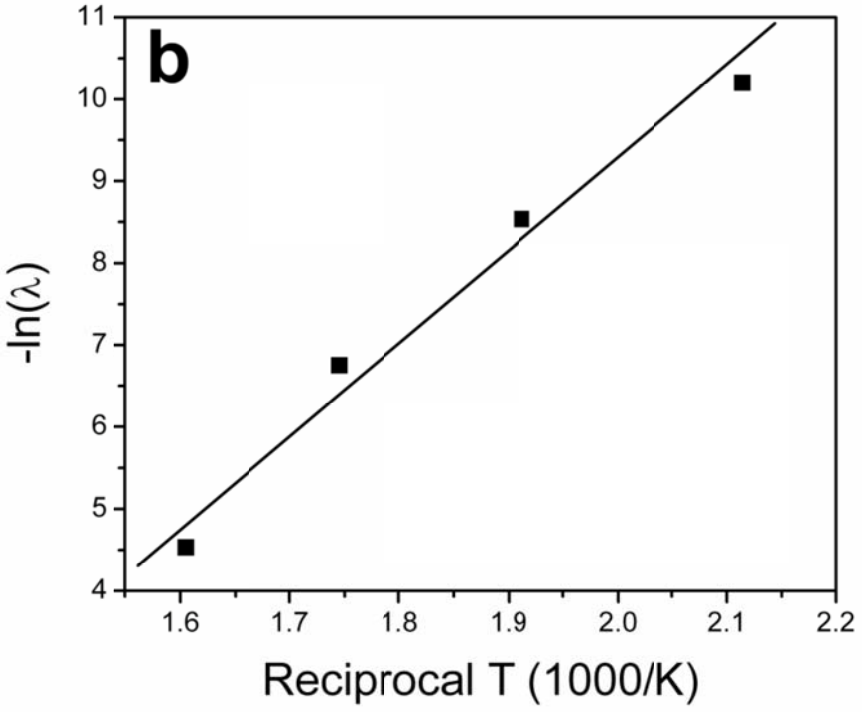

Figure 3-6b Arrhenius plots of decay constant [-ln (λ)] versus reciprocal temperature (1,000/T) for $[BO_4]^0$ center in datolite from 200 to 350 ℃.

where A is the pre-exponential factor; E is the activation energy; and k_b is the Boltzmann constant of 8.617×10^{-5} eV/K. The calculated activation energy is 0.96 eV. The pre-exponential factor A is meaningless in this case, because it is dependent on the initial concentration that was not determined in this study.

3.3.5 DFT results

DFT calculations using several hybrid functional shows that the B3PW functional of Perdew and Wang (1992) yielded the best results for the perfect structure of datolite (Table 3-3) and was subsequently adopted for all calculations made in this study. Particularly, our calculated unit-cell parameters and the fractional coordinates of all non-hydrogen atoms in the perfect structure of datolite are within ~0.34% of results from X-ray diffraction experiments (Foit *et al.* 1973; Table 3-3). Also, our results are notably better than those from previous WIEN2k calculations (Hansen *et al.* 2005). The hydrogen positions reported in the XRD studies of Foit *et al.* (1973) and Ivanov and Belokoneva (2007) yield unreasonably short <O–H> bond distances (Table 3-3) and therefore may be in significant error.

Relative to the $BO_3(OH)$ group in the perfect structure, the <B–O3> bond distance in the defect structure is increased by 0.01 Å, whereas the <B–O2>, <B-O4> and <B–O5> bonds are shortened by ~0.01 Å (Tables 3-3, 3-4). Mulliken population analysis shows that the unpaired spin of the defect is >85% localized on the O5 atom, while the remaining part is distributed among the other three oxygen atoms (Table 3-4). The calculated electron spin population and density on the center B atom are

Table 3-3 Comparison between the experimental and calculated unit-cell parameters and selected bond lengths in datolite

	Experimental		Calculated		
	XRD [a]	XRD[b]	PBE (Å)[c]	1×1×1[d]	1×2×2[d]
a(Å)	4.832(4)	9.636(6)	–	4.817	4.803
b(Å)	7.608(4)	7.620(4)	–	7.596	7.581
c(Å)	9.636(8)	4.839(3)	–	9.642	9.654
β(º)	90.40(7)	90.14(5)	–	90.56	90.62
B-O2	1.475(3)	1.4816(9)	1.488	1.486	1.486
B-O3	1.486(3)	1.4797(9)	1.484	1.481	1.483
B-O4	1.463(3)	1.4698(9)	1.480	1.471	1.470
B-O5	1.496(3)	1.4958(9)	1.503	1.494	1.491
O5-H	0.75(5)	0.89(2)	0.99	0.971	0.974

[a] Foit *et al.* (1973) in space group $P2_1/c$;
[b] Ivanov and Belokoneva (2007) in $P2_1/c$;
[c] WIEN2k PBE values from Hansen *et al.* 2005;
[d] CRYSTAL06 and B3PW of this study.

Table 3-4 Calculated spin population (*e*) and bond distances of the $[BO_4]^0$ center in datolite

Supercell	1 × 1 × 1[a]	1 × 2 × 2[a]	2 × 2 × 1[a]	2 × 2 × 2[b]
Spin density ($n_\alpha - n_\beta$)				
B	−0.0344	−0.0351	−0.0338	−0.0338
O2	0.0234	0.0212	0.0202	0.0125
O3	0.0612	0.0653	0.0637	0.0000
O4	0.0045	0.0048	0.0034	0.0064
O5	0.8557	0.8616	0.8544	0.8994
Bond distance (Å)				
B-O2	1.468	1.472	1.472	
B-O3	1.493	1.494	1.495	
B-O4	1.459	1.460	1.460	
B-O5	1.485	1.482	1.481	

[a] Defect introduced after geometry optimization;
[b] No geometry optimization for the 2×2×2 supercell.

Table 3-5 Comparison of experimental and calculated A (^{11}B) and nuclear quadrupole parameters of the $[BO_4]^0$ center in datolite

	Experimental		Calculated			
	295 K[a]	10 K[a]	1×1×1[b]	2×2×1[b]	1×2×2[b]	2×2×2[c]
a_{iso} (mT)	−0.786	−0.764	−0.7573	−0.7627	−0.7613	−0.7863
T_{zz} (mT)	0.329	0.363	0.3228	0.2782	0.3328	0.3014
T_{xx} (mT)	−0.189	−0.221	−0.1846	−0.1717	−0.1928	−0.1757
T_{yy} (mT)	−0.140	−0.142	−0.1382	−0.1148	−0.1400	−0.1257
eqQ/h (MHz)	-	-	0.3136	0.3167	0.3603	0.2221
η	-	-	0.4759	0.5326	0.4665	0.8527

[a] Experimental data from Table 3-2;
[b] Supercells with geometry optimization;
[c] 2×2×2 supercell without geometry optimization.

–0.034 and –0.0145 $e/bohr^3$, respectively. The calculated ^{11}B hyperfine constants and nuclear quadrupole parameters (eqQ/h and $\eta = |(P_1 - P_2)/P_3|$) are given in Table 3-5. It is also noteworthy that results from the $2 \times 2 \times 2$ supercell without geometry optimization are similar to those from the smaller supercells with full geometry optimization (Tables 3-4, 3-5).

3.4 DISCUSSION

3.4.1 Electronic structure of the $[BO_4]^0$ center in datolite

Bershov and Martirosyan (1970) reported a $[BO_4]^0$ center in datolite from Yakutiya, Russia. Their principal *g*-factor values are closely comparable to those of our study, and their maximum and minimum $A(^{11}B)$ values are similar to ours as well (Tables 3-1 and 3-2). However, their intermediate $A(^{11}B)$ value is approximately equal to the average of the other two values, resulting in a significant orthorhombic character. This is different from the approximately axial symmetry of the ^{11}B hyperfine matrix observed in our study (Table 3-2). It is uncertain where the $[BO_4]^0$ center reported by Bershov and Martirosyan (1970) is the same one investigated in this study or not.

The orientations of the g_1 and unique $A(^{11}B)$ axes suggest that the unpaired electron is largely localized in the $2p_z$ orbital of the hydroxyl oxygen atom O5 in the datolite structure. The isotropic component of $\mathbf{A}(^{11}B)$ suggests that ~1% of the unpaired spin is located on the B atom. DFT calculations provide further support for this model and show that 86.5% of the unpaired electron is localized on the O5 atom.

Also, the negative spin density on the B atom (Table 3-4) is attributable to electron polarization, which is common in paramagnetic systems. In addition, the calculated B3PW ^{11}B hyperfine coupling constants for the $[BO_4]^0$ center in datolite (Table 3-5) are in excellent agreement with results from EPR experiments (Table 3-2). Also, the calculated directions of the three $A(^{11}B)$ principal axes at (88.6°, 351.7°), (167.7°, 269.7°) and (102.2°, 81.3°) are in agreement with those determined from EPR experiments as well (Table 3-2).

Moreover, our calculated nuclear quadrupole parameters (*eqQ/h* and η) for the perfect structure can be compared with available data from MAS NMR experiments (Hansen *et al.* 2005). Specifically, our B3PW *eqQ/h* and η values of 0.157 MHz and 0.519 for the O_3BOH tetrahedral group in datolite are both close to the experimental results of 0.172(1) MHz and 0.647(5) (Hansen *et al.* 2005). In comparison, the calculated ^{11}B *eqQ/h* and η values of the $[BO_4]^0$ paramagnetic center in datolite are 0.31 MHz and 0.53, respectively, which are only slightly larger than those of the precursor O_3BOH tetrahedral group. In particular, the calculated *eqQ/h* value is typical of BO_4 tetrahedral groups (Shkrob and Tarasov 2000; Hansen *et al.* 2005 and references therein). Therefore, the calculated ^{11}B *eqQ/h* value provides additional support for the $[BO_4]^0$ structural model.

3.4.2 Formation mechanism

The facts that the $[BO_4]^0$ center in datolite increases systematically as a function of the radiation dose (Fig. 3-4) and, after thermal bleaching, can be restored by

gamma-ray irradiation suggest its origin related to radiation. The calculated spin-Hamiltonian parameters suggest that the $[BO_4]^0$ center in datolite apparently formed from the O_3BOH group by hole trapping on the hydroxyl oxygen atom after removal of its proton. This reaction can be written as follow:

$$O_3BOH \rightarrow [BO_4]^0 + H^0 \qquad (3\text{-}4)$$

This reaction is supported by the concurrent occurrence and growth of the $[BO_4]^0$ and H^0 centers during gamma-ray irradiation (Fig. 3-4). The presence of the $[BO_4]^0$ center in as-is datolite is probably attributable to natural radiation, whereas the absence of the H^0 center before irradiation can be explained by its decay at ambient temperature.

This formation mechanism is similar to that for the well-established $[AlO_4]^0$ center in quartz (Mackay 1963; Mackay *et al.* 1970; Nuttall and Weil 1981; Botis and Pan 2009). Mackay (1963) first detected the $[AlO_4/M^+]$ (where M = H, Li, Na) centers in quartz crystals that were irradiated and measured at 77 K. He noted that these centers lose the charge compensators on warming above 77 K, giving rise to the $[AlO_4]^0$ center. Therefore, the diamagnetic precursors to the $[AlO_4]^0$ center in quartz are $[AlO_4/M]$, including $[O_3AlOH]$ (Botis and Pan 2009). It is noteworthy that the H^0 center is commonly observed in quartz as well (Weil 1984). Similar but not identical mechanisms have also been proposed for the formation of the $[AlO_6]^0$ centers in several minerals, where the H^0 center is not present (Mao *et al.* 2010a, b and references therein).

3.4.3 Comparison with other BOHCs in minerals

The calculated $A(^{11}B)$ hyperfine constants of the $[BO_4]^0$ center in datolite are closely comparable to these of the most prevalent BOHCs in danburite (Bershov and Martirosyan 1970; Misra *et al.* 1983; Novozhilov *et al.* 1988; Table 3-1). These BOHCs in danburite were originally proposed to be $[BO_4]^0$ centers but were re-interpreted by Shkrob and Tarasov (2000) as $[BO_3]^{2-}$ centers. However, the large nuclear quadruple parameters (eqQ/h = 2.45-2.81 MHz and η = 0-0.23) from the ESEEM experiments of Shkrob and Tarasov (2000), which are indicative of trigonal B groups, are for the weakly coupled B nucleus in the most prevalent BOHCs in danburite. Also, their results of MNDO calculations (Figure 9 in Shkrob and Tarasov 2000) show the hole-trapping oxygen is part of the $[BO_4]$ group, fixed at ~0.245 nm away from the relaxed $[BO_3]$ group. Therefore, the results of Shkrob and Tarasov's (2000) are in fact consistent with the most prevalent BOHC in danburite being the $[BO_4]^0$ type, with the next-nearest B in a trigonal BO_3 group.

The $[BO_4]^0$ center in B-doped zircon (Walsby *et al.* 2000) has significantly smaller $A(^{11}B)$ hyperfine constants than its counterparts in datolite and danburite (Tables 3-1, 3-2). The experimental eqQ/h value of 1.34 MHz is notably larger than to those of its counterparts in datolite and danburite but remains significantly smaller than those typical of trigonal BO_3 groups (2.4-3.0; Shkrob and Tarasov 2000; Hansen *et al.* 2005), hence supporting the proposed $[BO_4]^0$ model (Walsby *et al.* 2000). Therefore, the spin-Hamiltonian parameters of $[BO_4]^0$ type centers in minerals may exhibit a significant variation. It is also noteworthy that the classic $[BO_3]^{2-}$ center in

calcite and the proposed $[BO_2]^0$ center in calcite and anhydrite have their principle g-factor values and $A(^{11}B)$ hyperfine constants broadly comparable to those of the $[BO_4]^0$ centers as well (Tables 3-1, 3-2).

3.4.4 Implications for BOHCs in borate and borosilicate glasses

Two types of BOHCs ($BOHC_1$ and $BOHC_2$ in Shkrob *et al.* 2000) in borate and borosilicate glasses are commonly distinguished on the basis of EPR spectra (Griscom *et al.* 1968; Griscom 1993; Kordas 2005). $BOHC_1$, which is observed in low-alkali glasses, is characterized by the presence of "five-line-plus-a-shoulder" in EPR spectra. $BOHC_2$ is present in high-alkali glasses and exhibits "4-line" spectra. Notwithstanding the continuing debates on the atomic and electronic structures of $BOHC_1$ and $BOHC_2$ (Griscom 1993; Shkrob *et al.* 2000; Kordas 2003, 2005; Kordas and Goldfarb 2008), identification of BOHCs in borate and borosilicate glasses can be made on the basis of their distinct spectral features. However, it is not uncommon that BOHCs in borate and borosilicate glasses, where they are incompletely resolved in powder EPR spectra, are interpreted on the basis of fitted principal g and $A(^{11}B)$ values (Kumar *et al.* 2004; Porwal *et al.* 2005; Kadam *et al.* 2008; Mohapatra *et al.* 2009). Our above discussion about BOHCs in minerals (Tables 3-1, 3-2) shows that identification and structural interpretation of BOHCs in borate and borosilicate glasses on the basis of principal g and $A(^{11}B)$ values must be exercised with caution.

Major concerns about the application of alkali borosilicate glasses for the encapsulation of high level nuclear wastes include the possibilities of enhanced cation

migration and volatilization related to radiation damage (Shkrob *et al.* 2000; Parkinson *et al.* 2007). Shkrob and Tarasov (2000) noted that radiation-induced BOHCs in danburite are associated with Ca vacancies and suggested that there is no direct linkage between hole trapping and the release of cations. Similarly, our results show that the formation of the $[BO_4]^0$ center in datolite does not involve Ca^{2+} cations but is related to the removal of H^+. We emphasize that H^+ is structurally different from the alkali modifiers (Li^+, Na^+, K^+, Rb^+ and Cs^+) in borosilicate glasses. Therefore, our study provides further evidence for the lack of enhanced cation migration associated with the formation of BOHCs in alkali borosilicate glasses. On the other hand, radiated-induced release of protons from hydroxyl groups may contribute to the prevalent volatilization process (Parkinson *et al.* 2007).

3.5 REFERENCES

Bacquet, G., Dugas, J., Belin, C. (1974): RPE de BO_2 dans la calcite synthetique irradiee. 18th AMPERE Congress, Nottingham.

Bershov, L.V., Marfunin, A.S. (1967): Electron-spin resonance of electron-hole centers in minerals. *Doklady Akademii nauk SSSR*, **173**: 410 (in Russian).

Bershov, L.V., Marfunin, A.S. (1981): On schemes of isomorphism of boron in alumosilicates, carbonates and sulfates according to electron-spin-resonance data. *Geokhimya*, **3**: 446-449.

Bershov, L.V., Martirosyan, V.O. (1970): Point defects in borosilicates danburite and datolite. *Soviet Physics Crystallography, USSR*, **14**: 823-825.

Botis, S.M. Pan, Y. (2009): First-principles calculations on the $[AlO_4/M^+]^0$ (M = H, Li, Na, K) defects in quartz and crystal-chemical controls on the uptake of Al. *Mineralogical Magazine*, **73**: 537-550.

Carboni, R., Pacchioni, G., Fanciulli, M., Giglia, A., Mahne, N., Pedio, M., Nannarone, S., Boscherini, F. (2003): Coordination of boron and phosphorous in borophosphosilicate glasses. *Applied Physics Letters*, **83**: 4312-4314.

Claridge, R.F.C., Mackle, K.M., Sutton, G.L.A., Tennant, W.C. (1994): 10K EPR of an oxygen-hole aluminum center, $[AlO_4]^0$, in x-irradiated zircon, $ZrSiO_4$. *Journal of Physics: Condensed Matter*, **6**: 10415-10422.

Deschanels, X., Peuget, S., Cachia, J.N., Charpentier, T. (2007): Plutonium solubility and self-irradiation effects in borosilicate glasses. *Progress in Nuclear Energy*, **49**: 623-634.

Dovesi R, Saunders VR, Roetti C, Orlando R, Zicovich-Wilson CM, Pascale F, Civalleri B, Doll K, Harrison NM, Bush IJ, D'Arco Ph, Llunell M (2006) CRYSTAL06 User's Manual, University of Torino, Torino. Italy.

http://www.crystal.unito.it

Eachus, R.S., Symons, M.C.R. (1968): Oxides and oxyions of non-metals. X. BO_3^{2-} impurity center in irradiated calcium carbonate. *Journal of the Chemical Society A: Inorganic, Physical, Theoretical*, **10**: 2438-2441.

Eichcorn, K., Treutler, O., Ohm, H., Hasar, M., Ahlrichs, R. (1995): Auxiliary basis sets to approximate coulomb potentials. *Chemical Physics Letters*, **240**: 283-290.

Foit, F.F.Jr., Phillips, M.W., Gibbs, G.V. (1973): A refinement of the crystal structure of datolite, $CaBSiO_4(OH)$. *The American Mineralogist*. **58**: 909-914.

Gatti, C., Saunders, V.R., Roetti, C. (1994): Crystal-field effects on the topological properties of the electron-density in molecular-crystals: the case of urea. *The Journal of Chemical Physics*, **101**: 10686-10696.

Griscom, D.L. (1993): Experimental Techniques of Glass Science, chap. 6, American Ceramic Society, Westerville OH, p 161.

Griscom, D.L., Taylor, P.C., Ware, D.A., Bray, P.J. (1968): ESR studies of lithium borate glasses and compounds γ irradiated at 77ºK: Evidence for a new interpretation of the trapped-hole centers associated with boron. *The Journal of Chemical Physics*,

48: 5158-5173.

Hansen, M.R., Madsen, G.K.H., Jakobsen, H.J., Skibsted, J. (2005): Refinement of borate structures from ^{11}B MAS NMR spectroscopy and density functional theory calculations of ^{11}B electric field gradients, *The Journal of Physical Chemistry A*, **109**: 1989-1997.

Ikeya, M. (1993): New applications of electron paramagnetic resonance: ESR dating, dosimetry, and spectroscopy. World Scientific, Singapore.

Ivanov, Y.V., Belokoneva, E.L. (2007): Multipole refinement and electron density analysis of natural borosilicate datolite using X-ray diffraction data. *Acta Crystallographica B*, **63**: 49-55.

Kadam, R.M., Seshagiri, T.K., Natarajan, V. and Godbole, S.V. (2008): Radiation induced defects in $BaBPO_5$: Ce and their role in thermally stimulated luminescence reactions: ESR and TSL investigations. *Nuclear Instruments and Methods in Physics Research B*, **266**: 5137-5143.

Kordas, G. (1999): Complementary use of cw-EPR, HYSCORE and pulse ENDOR spectroscopies for scanning the environment of unpaired states in a- and c-B_2O_3. *Journal of Non-Crystalline Solids*, **260**: 75-82.

Kordas, G. (2003): Equivalent exploitation of four-pulse one-dimensional ESEEM and HYSCORE spectroscopies for the elucidation of BOHC defects in borate glasses supported by quantum mechanical calculations. *Physical Review B*, **68**: 024202.

Kordas, G. (2005): On the structure of the BOHC in the borosilicate and borophosphosilicate glasses. *Journal of Non-Crystalline Solids*, **351**: 2358-2360.

Kordas, G., Goldfarb, D. (2008): Characterization of borate glasses by W-band pulse electron-nuclear double resonance spectroscopy. *Journal of Chemical Physics*, **129**: 154502.

Kumar, M., Kadam, R.M., Seshagiri T.K. Natarajan, V., Page, A.G. (2004): TSL and EPR studies of $SrBPO_5$ doped with CeO_2 and co-doped with CeO_2 and Sm_2O_3. *Journal of Radioanalytical and Nuclear Chemistry*, **262**: 633-637.

Lee, S., Bray, P.J. (1963): Electron spin resonance studies of irradiated glasses containing boron. *Journal of Chemical Physics*, **39**: 2863-2873.

Mackey, J.H. (1963): EPR study of impurity-related color centers in germanium-doped quartz. *Journal of Chemical Physics*, **39**: 74-83.

Mackey, J.H., Boss, J.W., Wood, D.E. (1970): EPR study of

substitutional-aluminum-related hole centers in synthetic α-quartz. *Journal of Magnetic Resonance*, **3**: 44-54.

Mao, M., Nilges, M.J. Pan, Y. (2010a): Radiation-induced defects in apophyllites. II. An O^- center and related O^-–O^- pairs in hydroxylapophyllite. *European Journal of Mineralogy*, **22**: 89-102.

Mao, M., Nilges, M.J., Pan, Y. (2010b) Single-crystal EPR and ENDOR study of an Al–O^- center in prehnite: Implications for aluminum-associated oxyradicals in layer silicates. *European Journal of Mineralogy*, **22**: 381-392.

Misra, S.K., Bandet, J., Bacquet, C., McEnally, T.E. (1983): Electron spin resonance studies of defect centers containing boron atoms in natural danburite crystals. *Physica Status Solidi. A, Applied Research*, **80**: 581-588.

Mohapatra, M., Kadam, R.M., Tomar, B.S., Mishra, R.K., Kaushik, C.P., Godbole, S.V., Raj, K., Manchanda, V.K. (2009): EPR investigations of electron beam irradiated Trombay waste base glass. *IOP Conference Series-Materials Science and Engineering*, **2**: 012022 (1-4).

Mombourquette, M.J., Weil, J.A. & McGavin, D.G. (1996): *EPR-NMR User's Manual*. Department of Chemistry, University of Saskatchewan, Saskatoon,

Saskatchewan.

Morton, J.R., Preston, K.F. (1978): Atomic parameters for paramagnetic resonance data. *Journal of Magnetic Resonance*, **30**: 577-582.

Novozhilov, A.I., Nosv. S.P., Gorbacheva, G.A., Samoilovich, M.I. (1988): EPR and optical absorption of color centers in danburite. *Mineral. Zh.* **10**: 85-88 (in Russian).

Nuttall, R.H.D., Weil, J.A. (1981): The magnetic properties of the oxygen–hole aluminum centers in crystalline SiO_2. I. $[AlO_4]^0$. *Canadian Journal of Physics*, **59**: 1696-1708.

Pacchioni, G., Vezzoli M., Fanciulli M. (2001): Electronic structure of the paramagnetic boron oxygen hole center in B-doped SiO_2. *Physical Review B*, **64**: 155201.

Pan, Y., Nilges, M.J., Mashkovtsev R.I. (2008): Radiation-induced defects in quartz. II. Single-crystal W-band EPR study of a natural citrine quartz. *Physics and Chemistry of Minerals*, **35**: 387-397.

Parkinson, B.D., Holland, D., Smith, M.E., Howes, M.E., Scales, C.R. (2007): Effect of minor additions on structure and volatilization loss in simulated nuclear

borosilicate glasses. *Journal of Non-Crystalline Solids*, **353**: 4076-4083.

Perdew, J.P., Wang, Y. (1992): Accurate and simple analytic representation of the electron-gas correlation energy. *Physical Review. B. Condensed Matter and Materials Physics*, **45**, 13244-13249.

Pisani, C., Dovesi, R., Orlando, R. (1992): Near-Hartree-Fock wave functions for solids: the case of crystalline silicon. *International Journal of Quantum Chemistry*, **42**: 5-33.

Porwal, N.K., Kadam, R.M., Seshagiri, T.K., Natarajan, V., Dhobale, A.R., Page, A.G. (2005): EPR and TSL studies on MgB_4O_7 doped with Tm: role of BO_3^{2-} in TSL glow peak at 470 K. *Radiation Measurements*, **40**: 69-75.

Schirmer, O.F. (2006): O- bound small polarons in oxide materials. *Journal of Physics: Condensed Matter*, **18**: 667-704.

Shkrob, I.A., Tarasov, V.F. (2000): On the structure of trapped hole in borosilicates. *Journal of Chemical Physics*, **113**: 10723-10732.

Shkrob, I.A., Tadjikov, B.M., Trifunac, A.D. (2000): Magnetic resonance studies on radiation-induced point defects in mixed oxide glasses: I. Spin centers in B_2O_3 and

alkali borate glasses. *Journal of Non-Crystalline Solids*, **262**: 6-34.

Taylor, P.C., Griscom, D.L., Bray, P.J. (1971): ESR studies of BO_3^{2-} ions in potassium borate ceramics. *Journal of Chemical Physics*, **54**: 748-760.

Valenzano, L., Torres, F.J., Doll, K., Pascale, F., Zicovich-Wilson, C.M., Dovesi, R. (2006): Ab initio study of the vibrational spectrum and related properties of crystalline compounds; the case of $CaCO_3$ calcite. *Zeitschrift fur Physikalische Chemie – International Journal of Research in Physical Chemistry & Chemical Physics*, **220**: 893-912.

Walsby, C.J., Lees, N.S., Tennant, W.C., Claridge, R.F.C. (2000): 15 K EPR of an oxygen-hole boron center, $[BO_4]^0$, in x- irradiated zircon. *Journal of Physics. Condensed Matter*, **12**: 1441-1450.

Webber, W.J., Ewing, R.C., Arnold, G.W., Angell, C.A., Cormack, A.N., Delaye, J.M., Griscom, D.L., Hobbs, L.W., Navrotsky, A., Price D.L., Stoneham, A.M., Weinberg, M.C. (1997): Radiation effects in glasses used for immobilization of high-level waste and plutonium disposition. *Journal of Materials Research*, **12**: 1946-1978.

Weigend, F., Ahlrichs, R. (2005): Balanced basis sets of split valence, triple zeta

valence and quadruple zeta valence quality for H to Rn: Design and assessment of accuracy, *Physical Chemistry Chemical Physics*, **7**: 3297-3305.

Weil, J.A. (1984): A review of electron spin spectroscopy and its applications to the study of paramagnetic defects in crystalline quartz. *Physics and Chemistry of Minerals*, **10**: 149-165.

Yasaitis, E.L., Smaller, B. (1953): Paramagnetic resonances in irradiated glasses. *Physical Review*, **92**: 1068-1069.

CHAPTER 4

Arsenic speciation in danburite ($CaB_2Si_2O_8$): A synchrotron XAS, single-crystal EPR and pulse ESEEM study

Gem-quality danburite containing 269 ppm As, from Charcas, San Luis Potosi, Mexico, has been investigated by synchrotron X-ray absorption spectroscopy (XAS), single-crystal electron paramagnetic resonance (EPR) and pulsed electron spin echo envelope modulation (ESEEM) spectroscopy. Arsenic K-edge X-ray absorption near-edge-structure (XANES) spectra show that the dominant oxidation state is +3, and modeling of the extended X-ray absorption fine structure (EXAFS) spectra suggests that As^{3+} mainly occupies the Si site. Single-crystal EPR spectra, measured before and after gamma-ray irradiation, reveal three arsenic-associated electron centers (I, II and III). Centers I and II have similar principal electron Zeeman g values and principal ^{75}As hyperfine constants [I: A_1/h = 732.9(1) MHz, A_2/h = –300.7(2) MHz and A_3/h = –275.5(2) MHz; II: A_1/h = 741.6(1) MHz, A_2/h = –329.1(2) MHz and A_3/h = –311.4(2) MHz]. These parameters suggest that Centers I and II are varieties of the $[AsO_2]^{2-}$ radicals, formed from electron trapping on substitutional As^{3+} ions at the Si site. This model for the $[AsO_2]^{2-}$ radical is further supported by ^{11}B (and ^{10}B) superhyperfine parameters determined from pulsed ESEEM. Center III is the $[AsO_3]^{2-}$ radical on the basis of its characteristic ^{75}As hyperfine constants [A_1/h = 2406.0(1) MHz, A_2/h = 1903.4(1) MHz and A_3/h = 1892.1(1) MHz]. The $[AsO_3]^{2-}$ radical with its A_1 axis along the Si–O4 bond direction originated from electron

trapping on a $[AsO_4]^{3-}$ group after removal of the O4 atom during gamma-ray irradiation. Therefore, arsenic in the borosilicate danburite is present in both the +3 and +5 oxidation states and preferentially occupies the Si site.

4.1 INTRODUCTION

The mobility and bioavailability of arsenic in nature are largely controlled by its host minerals (Smedley and Kinniburgh 2002; O'Day 2006). Consequently, numerous studies have been devoted to determine the abundance and speciation of arsenic in various minerals. There is now a large body of compositional and structural data of As in many As-rich minerals (e.g., arsenides, sulfarsenides, arsenites and arsenates) and common As-bearing minerals (e.g., sulfides, phosphates, sulfates, and oxides; Smedley and Kinniburgh 2002; O'Day 2006). Rock-forming silicate minerals, however, were thought to contain only < 2.3 ppm As (Baur and Onishi 1969; Smedley and Kinniburgh 2002) and, therefore, have generally been ignored with respect to their roles as natural sinks for this element or their potential applications for the remediation of As in the environment, except that clay minerals and zeolite-group minerals have been investigated for their surface sorption capacities.

Several recent studies have reported substitutions of elevated amounts of As^{5+} for Si^{4+} in silicates (Filatov *et al.* 2004; Charnock *et al.* 2007; Mao *et al.* 2010, Nagashima and Armbruster 2010). We have also shown that As^{5+} can substitute for B^{3+} in borates (e.g., colemanite; Lin *et al.* 2011). As part of our investigation on radiation-induced defects in borates and borosilicates (Li *et al.* 2011, 2012), we have

measured single-crystal electron paramagnetic resonance (EPR) spectra of gem-quality danburite ($CaB_2Si_2O_8$ and space group *Pnam*), from Charcas, San Luis Potosi, Mexico, before and after gamma-ray irradiation. These EPR spectra reveal the presence of three well-resolved arsenic-associated oxyradicals. The crystal structure of danburite consists of a tetrahedral framework of ordered Si_2O_7 and B_2O_7 groups with Ca in irregular coordination (Fig. 4-1; Phillips *et al.* 1974). Of five distinct oxygen atoms, O1, O2 and O3 are bonded to both B and Si, whereas O4 and O5 are the bridging oxygen atoms of the Si_2O_7 and B_2O_7 groups, respectively. The calcium atoms and the bridging oxygen atoms O4 and O5 all lie in mirror planes normal to **c** at heights of 0.25 and 0.75 (Fig. 4-1; Phillips *et al.* 1974). The presence of both SiO_4 and BO_4 groups in danburite provides an opportunity for investigating possible intracrystalline partitioning of As between Si and B tetrahedral sites. Therefore, our EPR study of arsenic in danburite was expanded to include compositional and structural analyses by inductively coupled plasma mass spectrometry (ICP-MS), synchrotron X-ray absorption spectroscopy (XAS) and pulsed electron spin echo envelope modulation (ESEEM) spectroscopy. Results from these multiple spectroscopic techniques provide information about arsenic speciation and site preference in danburite.

4.2 SAMPLE AND EXPERIMENTAL TECHNIQUES

4.2.1 Sample description and sample preparation

A sample of gem-quality danburite (Charcas, San Luis Potosi, Mexico) from the

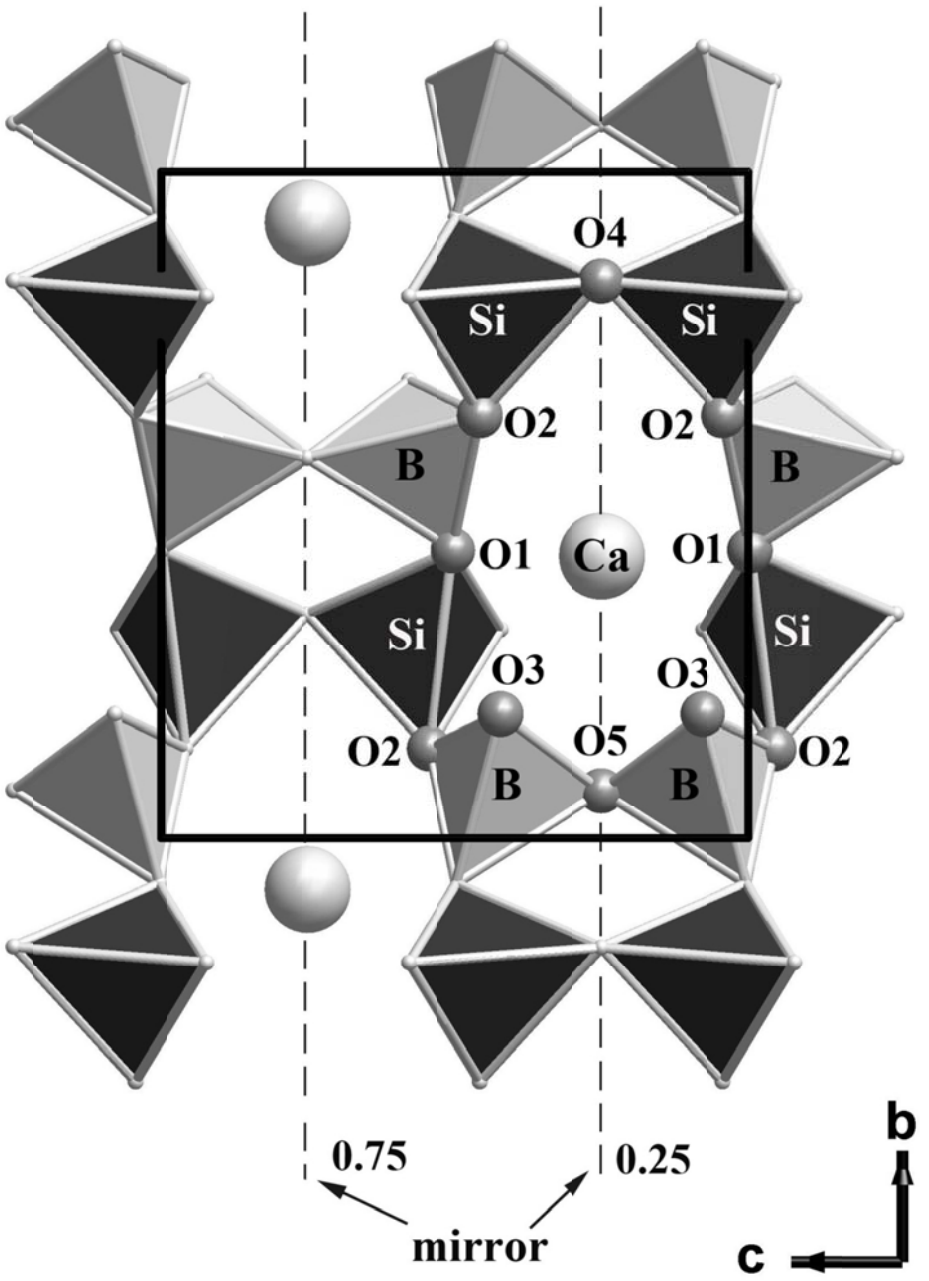

Figure 4-1 Crystal structure of danburite projected to (100) illustrating the linkage of the $[Si_2O_7]$ and $[B_2O_7]$ groups. Labels of the oxygen atoms after Phillips *et al.* (1974).

University of Saskatchewan reference mineral collection was investigated in this study. This sample contains prismatic crystals of danburite with well-developed {100}, {110), and {111} forms set in a matrix of pyrite and chalcopyrite. Several danburite crystals of ~3×1×1 mm were selected for single-crystal EPR measurements, before and after gamma-ray irradiation. Gamma-ray irradiation was carried out at room temperature in a ^{60}Co cell with a dose rate of ~460 Gy/h for doses up to ~22 kGy. Also, several crystals were first pulverized and then dissolved in HF-HNO_3 for trace element analysis by use of ICP-MS, on a Perkin Elan 5000 instrument at the Department of Geological Sciences, University of Saskatchewan.

4.2.2 Synchrotron X-ray absorption spectroscopy

Arsenic K-edge X-ray absorption spectra of danburite and five model compounds (arsenolite, orpiment, realgar, scorodite and As_2O_3 from Alfar Aesar) were measured at the super-conducting wiggler sourced HXMA Beamline (Jiang *et al.* 2007) at the Canadian Light Source, University of Saskatchewan. The HXMA Beamline was run under the mirror-monochromator-mirror mode with a Si (111) monochromator crystal and Rh mirror configuration. Arsenic K-edge spectra for the model compounds were collected in the transmission mode, whereas those for the danburite sample were collected in the fluorescence mode by using a 32 element Ge detector. The sizes of scan steps for the pre-edge, X-ray absorption near-edge structure (XANES), and extended X-ray absorption fine structure (EXAFS) regions were 10 eV/step, 0.25 eV/step, and 0.05 $Å^{-1}$/step, respectively.

4.2.3 Single-crystal EPR and ESEEM experiments

All X-band EPR measurements at room temperature (~295 K) were made on a Bruker EMX instrument at the Saskatchewan Structure Sciences Centre, University of Saskatchewan, equipped with an automatic frequency controller, a high-sensitivity ER4119 cavity, and a home-made goniometer with a precision of ~0.2º. Calibration of the magnetic field was made by use of the free radical α, γ-bis-diphenylene-β-phenyl allyl (BDPA) in benzene (g = 2.0027).

An as-is danburite crystal was chosen for detailed EPR measurements in three rotation planes: i.e. magnetic field **B** parallel to the (001), (010) and (110) faces. Experimental conditions included a microwave frequency of ~9.63 GHz, a microwave power of ~20 mW, a modulation frequency of 100 kHz, and a modulation amplitude of 0.1 mT. Spectral resolutions of the three planes (001), (010) and (110) were 0.022 mT (2,048 field data points over 45 mT), 0.049 mT (2,048 points over 100 mT) and 0.027 mT (2,048 points over 55 mT), respectively.

Single-crystal EPR measurements of a gamma-ray-irradiated danburite (~22 kGy) were made in two rotation planes: i.e., magnetic field **B** parallel to the (001) and (110) faces. Experimental conditions were similar to those described above, except that three spectra of different scan widths and spectral resolutions were collected at each crystal orientation. Specifically, spectra in the (001) plane were measured for three scan widths of 260 mT, 100 mT and 8 mT at corresponding spectral resolutions of 0.063 mT, 0.024 mT and 0.008 mT. Spectra in the (110) plane were collected at scan widths of 270 mT, 55 mT and 8 mT with spectral resolutions of 0.066 mT, 0.054 mT

and 0.008 mT, respectively. Also, the wide-scan (260 mT and 270 mT) and the narrow-scan (8 mT) spectra were measured with a microwave power of 63 mW.

ESEEM spectra at 80 K were collected on a Bruker E580-10 Elexsys with a liquid He Oxford CF935 cryostat. Spectra were obtained with a three-pulse scheme ($\pi/2 - \tau - \pi/2 - T - \pi/2 -$ echo) and four-step phase cycling (4,096 points @ 8ns steps). Time domain ESEEM spectra were baseline corrected, zero-filled, apodized, and Fourier transformed to give frequency domain spectra. Because three-pulsed ESEEM gives rise to blind-spots that arise from an oscillating τ dependence, ESEEM spectra were also recorded as a function of τ and later summed (16spectra @ 16ns steps). ESEEM spectra at a rotation angle of every 15° were collected on a crystal mounted with the rotation axis approximately perpendicular to the (110) face. Angle corrections (~2º) were calculated by simulating the corresponding continuous-wave spectra.

4.3 RESULTS

4.3.1 Danburite crystals and composition

Danburite crystals investigated in this study were colorless and transparent, but became brownish in color after gamma-ray irradiation. ICP-MS analysis yielded 17,700 ppm Zn, 7,200 ppm Al, 1,120 ppm Sr, 274 ppm Ti, 269 ppm As, 169 ppm Fe, 119 ppm Mn, 30 ppm Cu, 24 ppm Ba, and 22 ppm Pb. Other trace elements are below the detection limits of ~0.1 ppm.

4.3.2 Arsenic K-edge XANES and EXAFS spectra

The As K-edge XANES spectrum shows that As^{3+} is the dominant oxidation state in danburite (Fig. 4-2). Modeling of the As K-edge EXAFS spectrum of danburite (Fig. 4-3) has been made for all three possible occupancies of As at the tetrahedral B and Si sites and the nine-coordinated Ca site, using the program FEFF7.02 (Rehr and Albers 2000). The calculated nearest-neighbor Fourier-transform-magnitude peaks for As at the Si and B sites (Fig. 4-3) are slightly shorter than the first magnitude peak in the experimental spectrum, because modeling was based with the ideal structure that ignores the local structure perturbation from the occupancy of the As atom. Nevertheless, the overall agreements for the peaks at ~1.3-1.4 Å (phase-uncorrected distance) between modeling and the experimental spectrum suggest that As resides at the tetrahedral B or Si site, or both. However, the calculated magnitude peak of the first coordination shell based on As at the Si site is closer to the experimental data than that from As at the B site, hence favoring the former. Modeling also shows that the two As-O subshells for As at the Ca site will have their Fourier transform magnitude peaks at ~2.0 Å and 3.1 Å (Fig. 4-3). However, the second As-O sub-shell has a much weaker signal than the first shell, because of cancellation of the back-scattering signal among the different As-O paths of the shell and the long R distance. The first-sub-shell magnitude peak at ~ 2.0 Å for As at the Ca site can account for the second peak in the experimental spectrum, which cannot be explained by As at either the Si or B site.

R-space-curve fitting was performed by using XAFS software WINXAS version

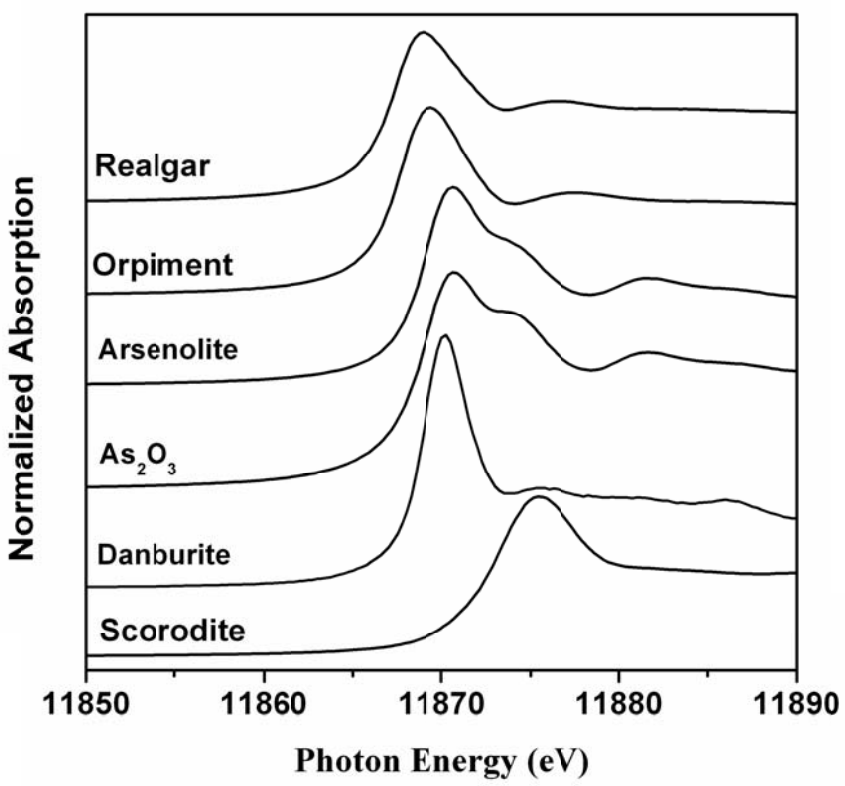

Figure 4-2 Comparison of the As K-edge XANES spectra of danburite and five model compounds showing that As in the former is dominantly of the +3 oxidation state.

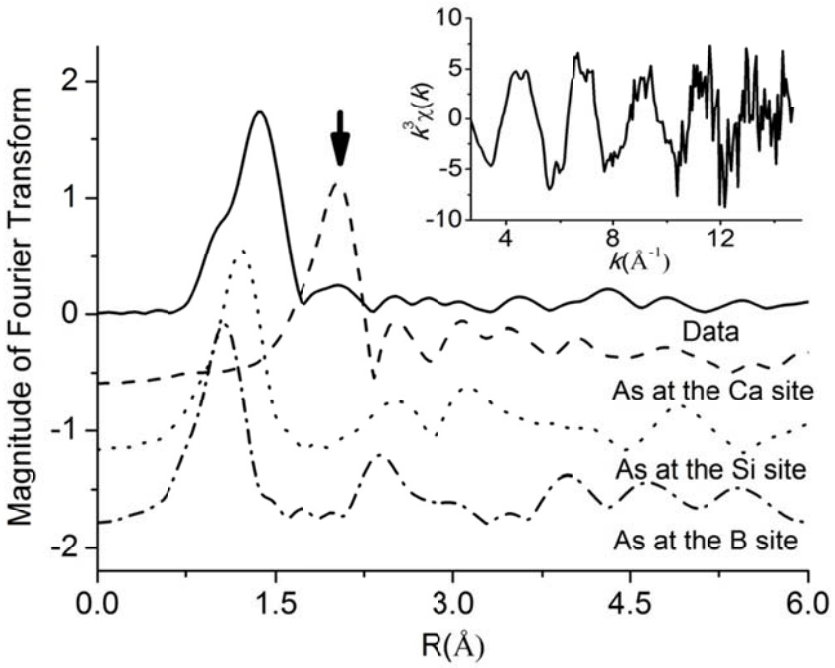

Figure 4-3 The As K-edge EXAFS spectra (solid lines) of danburite in R and *k* (insert) spaces. Also shown for comparison are FEFF modeled XAFS for As at the Ca, Si, and B sites. The As-O scattering for As at the Ca site is marked by an arrow. Fourier transformation was performed over the *k* range of 2.7-14.7 Å^{-1}.

2.3 (Ressler 1997). Initially, the first Fourier transform peak at ~1.4 Å was fitted in the window of 1.0-1.8 Å by using the FEFF calculated amplitude and phase for As at the Si and B sites (Fig. 4-4a). The transform for the experimental data was performed by using a Gaussian window function over *k* range of 2.7-14.7 $Å^{-1}$ with the window parameter of 30%. The fitted parameters are summarized in Table 4-1. The calculated R_{As-O} values from the two structural models are similar at 1.77-1.80 Å (Table 4-1). However, the residual for the model with As at the B site is 4.7 times larger than that for As at the Si site. Also, calculations for As at the Si site yield better agreements for the peak position and line shape in both magnitude and imaginary part of the Fourier transform than those for As at the B site (Fig. 4-4a). Also, the fit for the model of As at the B site does not appear to have any physical meaning beyond the first-shell R region. Therefore, fitting of the EXAFS spectrum also favors the model with As at the Si site.

In addition to the first-shell fittings above, modeling has been performed over the R region from 1.0 to 2.3 Å to include the next-nearest-neighbor shell. Again, two structural models were considered: one with As at the Si and Ca sites and another having As at the B and Ca sites (Fig. 4-4b). For reasons discussed above, only the first shell of the Ca coordination (i.e., As-O_1) was included. Table 4-1 shows that the two models yielded similar CN, R, and σ^2 values for both As-O and As-O_1 scattering paths. However, the model with As at the Si and Ca sites yielded a residual 27% smaller than that with As at the B and Ca sites, again favoring As mainly at the Si site (Table 4-1). Also, the calculated CN_{As-O1} value of ~2 is consistent with As at the Ca site as well.

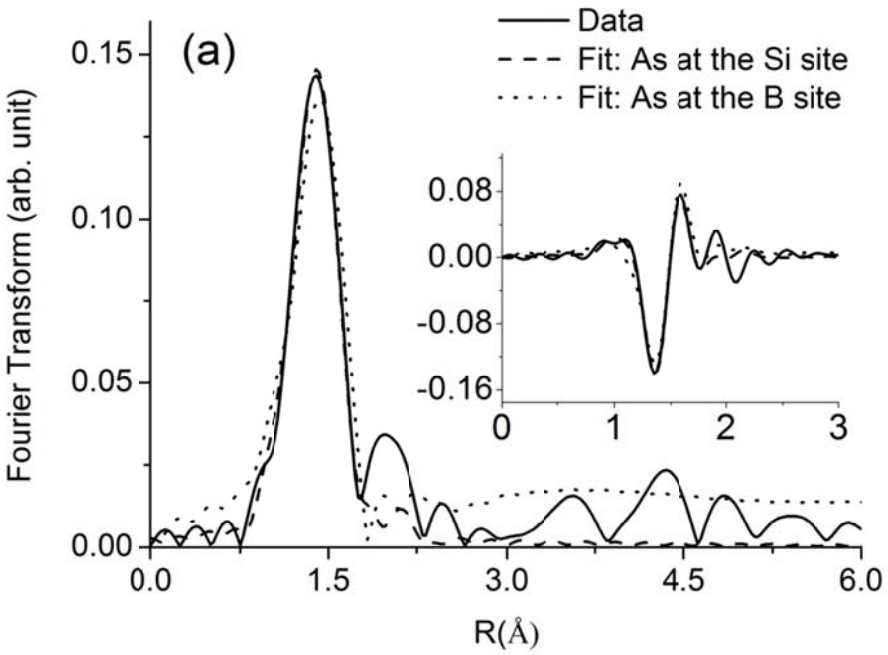

Figure 4-4a R-space curve fittings of the magnitude (and imaginary part in insert) of the As K-edge EXAFS spectrum of danburite comparison with those from the first-shell fits for As at the Si or B site.

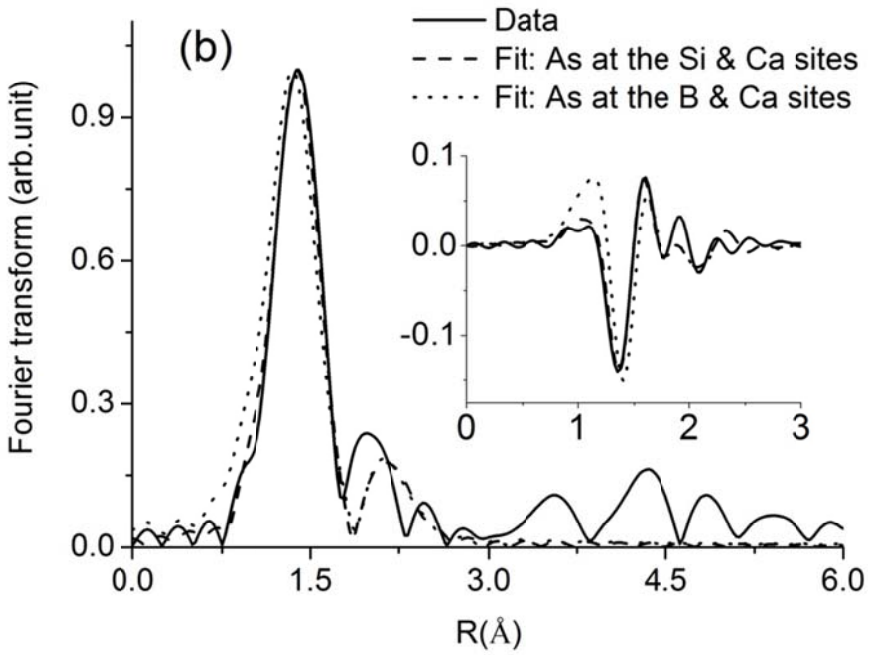

Figure 4-4b R-space curve fittings of the magnitude (and imaginary part in insert) of the As K-edge EXAFS spectrum of danburite comparison with those from the two-shell fits for As at the Si and Ca sites or the B and Ca sites.

Table 4-1 Arsenic *k*-edge XAFS fitting results

		As-O[a] tetrahedron coordination			As-O_1[b] Ca site coordination			
		CN_{As-O}	R_{As-O} (Å)	σ_{As-O} (Å^2)	CN_{As-O1}	R_{As-O1} (Å)	σ_{As-O1} (Å^2)	Residual
1st shell fit	B site	3.0	1.80	0.0029				14.4
	Si site	4.2	1.77	0.0033				3.1
2 shell fit	B site	4.0	1.77	0.0029	1.9	2.60	0.0030	16.7
	Si site	3.9	1.76	0.0026	2.1	2.57	0.0031	13.2

a. As-O single scattering within SiO4 and BO4 tetrahedron;
b. As-O1 single scattering of the first sub shell of the Ca site.

The calculated molar ratio between As at the Ca and Si sites is 0.3:1. We acknowledge that our calculated occupancies for As at the Ca and Si sites may contain significant uncertainties owing to the correlations between CN and σ^2.

4.3.3 Single-crystal X-band EPR spectra

Previous single-crystal EPR studies of danburite, including crystals from Charcas, have established a series of boron-associated oxygen hole centers (BOHCs; Bershov and Marfunin 1967; Misra *et al.* 1983; Novozhilov *et al.* 1988; Shkrob and Tarasov 2000). Single-crystal EPR spectra of as-is danburite measured in this study also contain a BOHC similar to that reported by Bershov and Marfunin (1967). Single-crystal EPR spectra of gamma-ray-irradiated danburite reveal additional BOHCs, similar to those reported by Misra *et al.* (1983) and Novozhilov *et al.* (1988). No attempt has been made to re-investigate these BOHCs here.

In addition to the BOHC of Bershov and Marfunin (1967), single-crystal EPR spectra of as-is danburite, measured with **B** parallel to a crystallographic axis, also reveal two quartets (i.e. two sets of four lines with approximately same separation and equal intensity; labeled I and II in Figure 4-5a). Center I has a significantly higher intensity than Center II in spectra of as-is crystals (Fig. 4-5a) and is enhanced slightly by gamma-ray irradiation. However, Center II is readily enhanced by gamma-ray irradiation and becomes stronger than Center I after only ~1 kGy gamma-ray irradiation (Fig. 4-5b). These two quartets have average line widths of ~0.5 and ~0.7 mT, respectively, and are split into four sets of each with **B** away from

crystallographic axes (Fig. 4-6a, 4-6b and 4-6c). These spectral features suggest that Centers I and II both represent a simple spin (S=1/2) interacting with an I=3/2 nucleus with a natural isotope abundance of ~100%. At various crystal orientations, the main absorption lines of Centers I and II are accompanied by numerous weak lines (Fig. 4-5c), which are attributable to "forbidden transitions" arising from a nucleus with a considerable nuclear quadrupole effect. These spectral features together with the presence of As from the ICP-MS analysis allow us to identify Centers I and II as two arsenic-associated oxyradicals.

In addition, narrow scans show that the broad lines of Centers I and II at most orientations appear as either irregular multiplets or well-resolved quartets with a splitting of up to 0.25 mT (Fig. 4-5d), suggesting a superhyperfine interaction with a neighboring I = 3/2 nucleus. These superhyperfine structures have been confirmed by pulsed ESEEM to arise from interaction with a neighboring ^{11}B nucleus (see below).

The wide-scan EPR spectra of gamma-ray-irradiated danburite also contain a third quartet (III; Fig. 4-5b), with much larger separations than Centers I and II. This quartet is too split into four sets when **B** is away from crystallographic axes. This site splitting, however, is resolved only for the transition lines at the lowest and highest magnetic fields (Fig. 4-6d), which have an average line width of ~0.6 mT. Site splitting for the two middle-transition lines are usually not resolved, resulting in broad peaks. This quartet, which is also consistent with a single spin S = 1/2 interacting with a nucleus of I = 3/2 and a natural isotope abundance of ~100%, is interpreted to represent another arsenic-associated oxyradical.

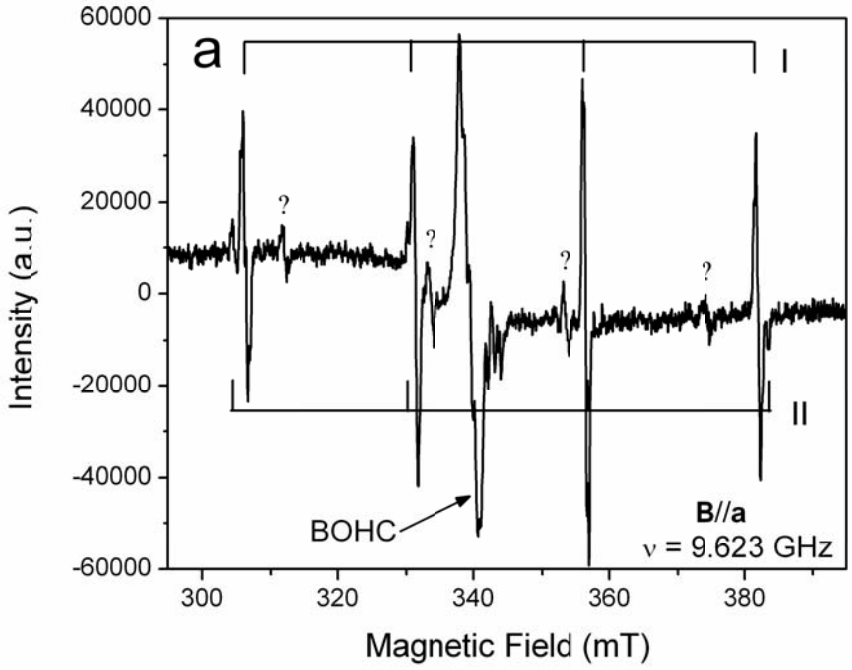

Figure 4-5a Representative single-crystal EPR spectra of as-is danburite illustrating the presence of BOHC and Center I. Note that Center II and another quartet (marked by ?) are also visible but very weak.

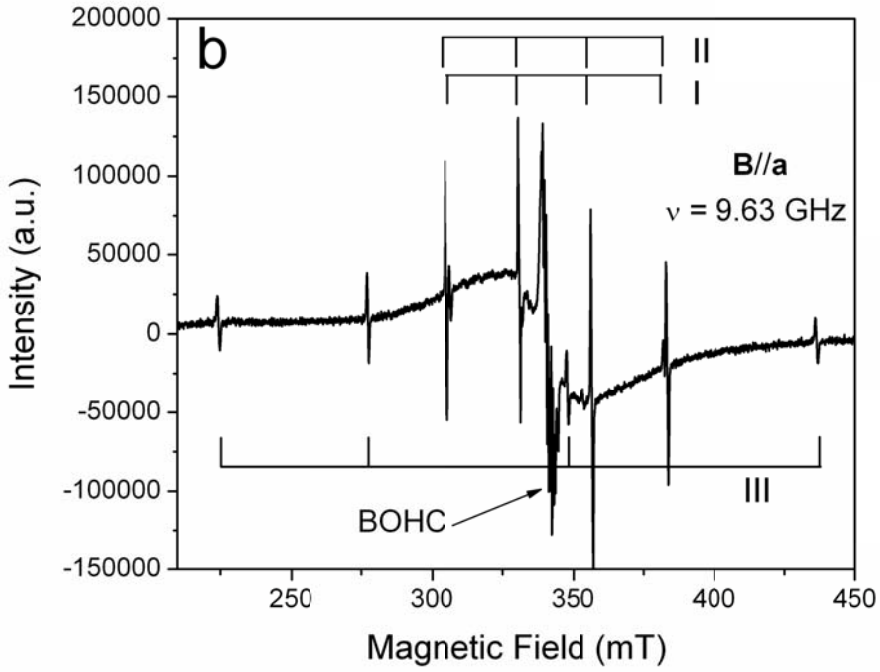

Figure 4-5b Representative single-crystal EPR spectra of gamma-ray-irradiated danburite showing the marked growth of Center II and the addition of Center III, whereas Center I remains essentially unchanged in intensity relative to that in Figure 4-5a.

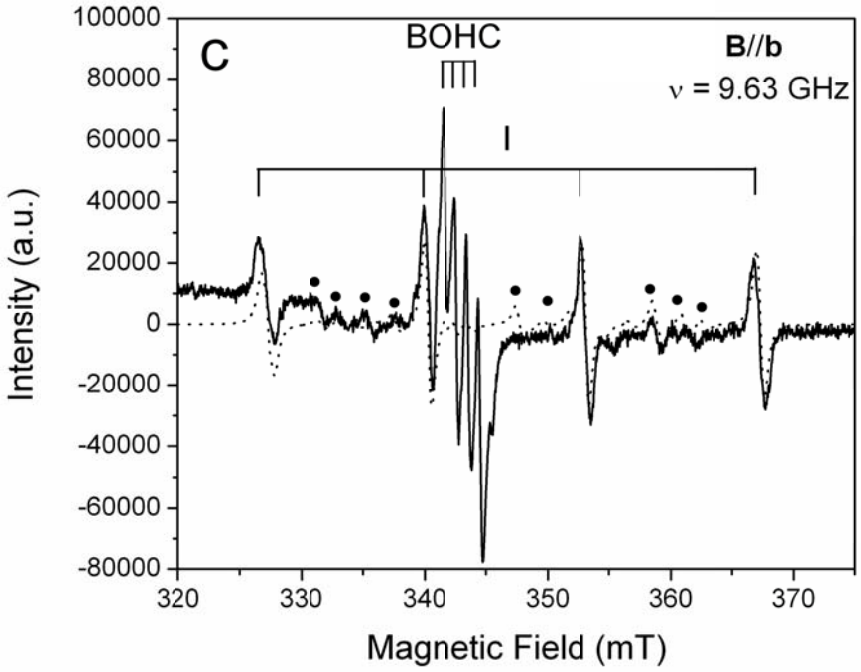

Figure 4-5c Representative single-crystal EPR spectra of as-is danburite showing that the weak "forbidden transitions" lines (marked by solid circles) of Center I are reproduced by the spin Hamiltonian parameters in Table 4-2.

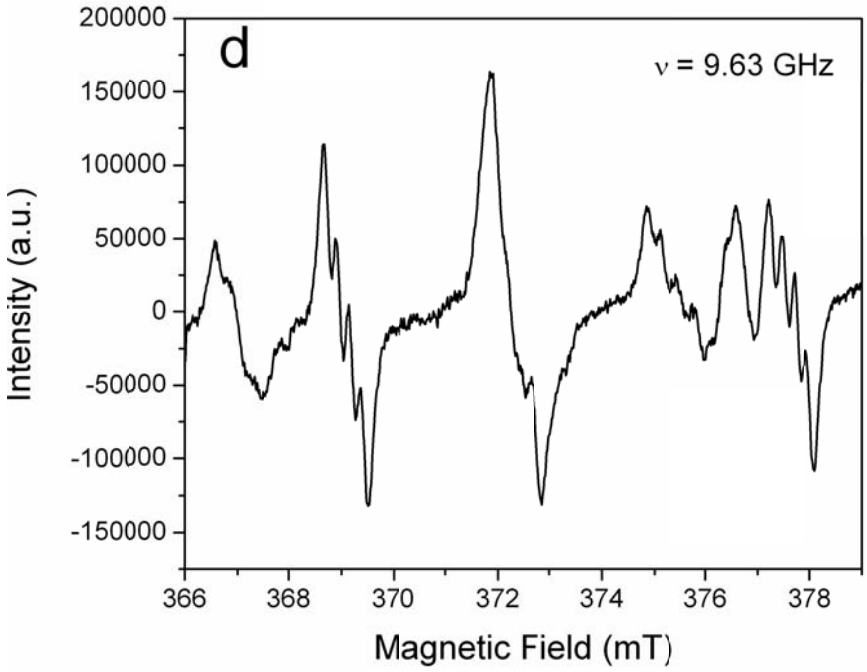

Figure 4-5d Representative single-crystal EPR spectra of gamma-ray-irradiated danburite (narrow scan) showing that the high-field lines of Centers I and II appear as either irregular multiplets or well-resolved quartets arising from interaction with a neighboring ^{11}B nucleus.

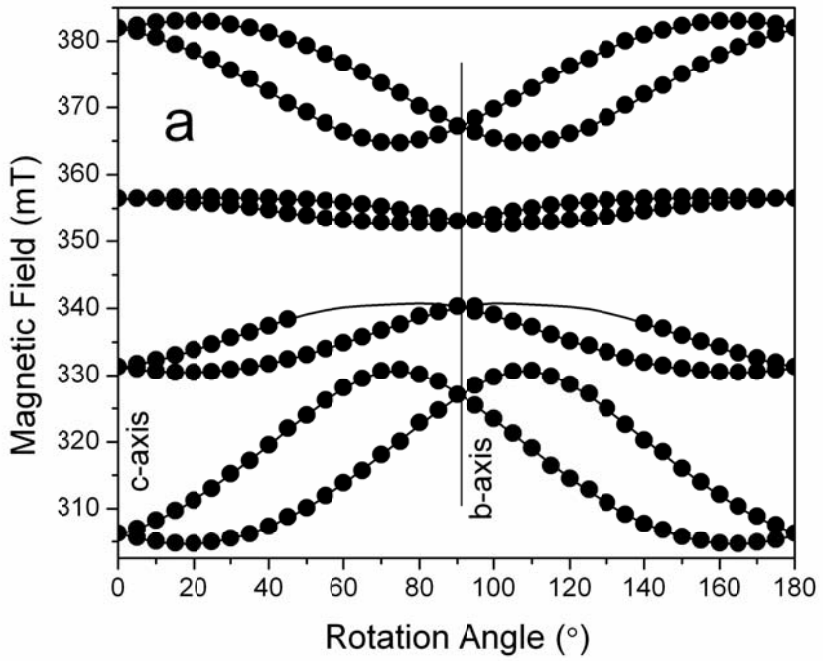

Figure 4-6a Representative line-position data versus rotation angles (i.e. roadmaps) for Center I in the (010) plane at $\nu = 9.622$ GHz.

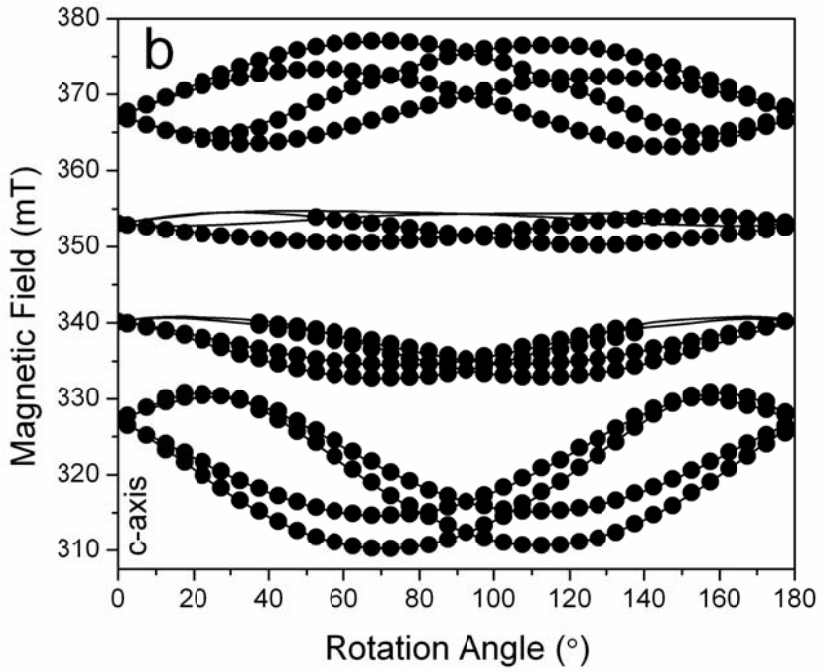

Figure 4-6b Representative line-position data versus rotation angles (i.e. roadmaps) for Center I in the (110) plane at $\nu = 9.627$ GHz.

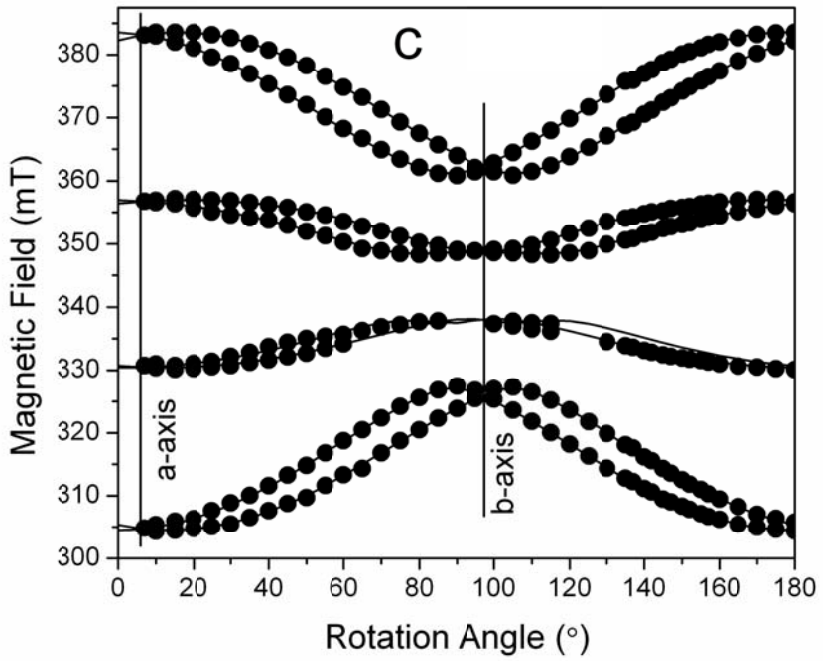

Figure 4-6c Representative line-position data versus rotation angles (i.e. roadmaps) for Center II in the (001) plane at ν = 9. 627 GHz.

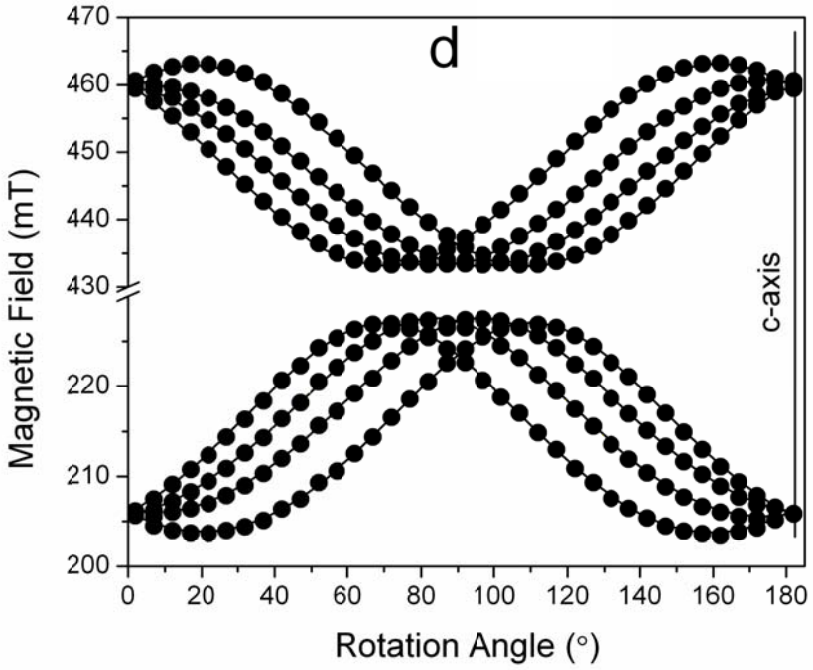

Figure 4-6d Representative line-position data versus rotation angles (i.e. roadmaps) for the low- and high-field hyperfine transitions of Center III in the (110) plane at ν = 9.627 GHz.

4.3.4 Spin-Hamiltonian parameters of the three Arsenic-associated oxyradicals

The spin Hamiltonian for the three Arsenic-associated oxyradicals, ignoring the incompletely-resolved ^{11}B superhyperfine structures of Centers I and II, can be written as:

$$\boldsymbol{H_s} = \beta_e \mathbf{S} \bullet \mathbf{g} \bullet \mathbf{B} + \mathbf{I} \bullet \mathbf{A} \bullet \mathbf{S} + \mathbf{I} \bullet \mathbf{P} \bullet \mathbf{I} - g_n \beta_n \mathbf{I} \bullet \mathbf{B}$$

where β_e and β_n are the electronic (Bohr) and nuclear magnetons, respectively; and a scalar g_n value of 0.959647 is adopted for ^{75}As. Iterative fittings for all three centers, using the software package EPR-NMR (Mombourquette *et al.* 1996), were made first by inclusion of matrices **g** and **A**, and were accompanied by steps of angle corrections. The nuclear quadrupole tensor **P** (^{75}As) was added in the final stages and was fitted together with **g** and **A**.

Specifically, single-crystal EPR spectra measured in three rotation planes of an as-is danburite were used for the fitting of Center I. Narrow- and wide-scan spectra collected in two rotation planes of a gamma-ray-irradiated crystal were used for the fittings of Centers II and III, respectively. The total numbers of line-position data points from the main absorption lines of Centers I, II and III are 1,541, 858 and 1,066, respectively. All line-position data points for Centers I and II were assigned an equal weighting factor of 1.0. However, line-position data points in the crossover regions of magnetically nonequivalent sites of Center III were assigned a weighing factor of 0.4, resulting in a sum of weighted factors of 972.4.

The signs of hyperfine coupling constants cannot be determined from EPR data alone. The observed magnitudes of the ^{75}As hyperfine structures of Centers I and II

are similar to those of either the neutral AsO_2 radical (Knight *et al.* 1995) or the $[AsO_2]^{2-}$ radical (Marshall and Serway 1969). We prefer to denote the former as the $[AsO_2]^0$ to specify its net charge and its diamagnetic precursor $[AsO_2]^-$ with an As^{5+} ion. The $[AsO_2]^0$ radical is known to have a small amount of the unpaired spin in the As 4*s* orbital, resulting in a considerable isotropic component of its ^{75}As hyperfine (Knight *et al.* 1995). The $[AsO_2]^{2-}$ radical, on the other hand, has the unpaired spin largely in the As 4*p* orbital, giving rise to a negligible isotropic component of the ^{75}As hyperfine (Marshall and Serway 1969). Fittings have been made for both of these schemes and yielded indistinguishable root-mean-squares of weighted differences (RMSD) between the calculated and observed line positions (i.e., both 0.07 for Center I and both 0.08 mT for Center II). The calculated normals of the three rotation planes of the as-is danburite are (90.0º, 90.0º), (2.0º, 92.6º) and (92.0º, 44.8º), which are all close to the ideal values (90º, 90º), (0º, 90º) and (90º, 42.6º) of the (010), (001) and (110) planes. The calculated normals of the two rotation planes used for the fitting of Center II are (0º, 349.1º) and (90.0º, 44.3º), which are too close to the ideal normals of the (001) and (110) planes.

Spectral simulations also showed that spin Hamiltonian parameters obtained from the $[AsO_2]^0$ and $[AsO_2]^{2-}$ models both provide excellent predictions for the observed spectra of Centers I and II, including excellent reproductions of all "forbidden transition" lines (Fig. 4-5b) that were not used in the fittings. The presence of dominantly As^{3+} as revealed by the As K-edge XANES spectrum leads us to favor Centers I and II to represent the $[AsO_2]^{2-}$ radicals. Admittedly, the fitted A(^{75}As)

hyperfine constants from the $[AsO_2]^{2-}$ model give b = 344 and 357 MHz, which exceed the b_0 value of 334 MHz (Morton and Preston 1978).

The observed magnitude of the ^{75}As hyperfine structure of Center III is within the range reported for the $[AsO_3]^{2-}$ radical (Serway and Marshall 1966; Dalal *et al.* 1972; Xu 1992; Pöppl *et al.* 1994; Pan 2012). Therefore, our fitting of Center III started with parameters typical of the $[AsO_3]^{2-}$ and converged readily to give the RMSD value of 0.07 mT. The calculated normals of the experimental (001) and (110) planes at (177.9°, 2.0°) and (89.1°, 43.3°), respectively, are slightly away from the ideal values (180°, 0°) and (90°, 42.6°).

In particular, the **g** matrix for the $[AsO_3]^{2-}$ radical is orthorhombic in symmetry, whereas the **A(**^{75}As) matrix is of approximately axial symmetry. The orientation of the unique **A** axis (20.8°, 203.3°) is approximately along the Si–O4 bond direction (21.5°, 203.3°). The nuclear quadrupole tensor P is negligibly small and hence is difficult to determine precisely (Table 4-4)

.

4.3.5 Pulsed ESEEM Spectra

Each of the four ^{75}As hyperfine lines of Centers I and II is split into four, consistent with site splitting of the D_2 crystal symmetry. The exciting field was set on one of the outer pair of lines on the high field ^{75}As group for Center II, and ESEEM spectra were recorded as a function of the rotation angle. Due to spectral overlap, it was not possible to follow for the inner pair of lines, but data were collected at a few selected orientations where the inner lines were well resolved and used to refine the

analysis. Also due to spectral overlap, lines for Center I could not be readily followed, however, a selected number of orientations/lines of Center I could be found and ESEEM spectra were measured. Also, near the c-axis, transitions for Center I overlap enough with those of Center II so that peaks for Center I could be observed in what are nominally ESEEM spectra of Center II. ESEEM spectra were simulated using SIMEND (Nilges *et al*. 2009). The calculated Hamiltonian matrices included all the ^{75}As, ^{10}B and ^{11}B hyperfine and quadrupole terms:

$$\boldsymbol{H_s} = \beta_e \mathbf{B} \bullet \mathbf{g} \bullet \mathbf{S} + \mathbf{I}^{\mathbf{As}} \bullet \mathbf{A}^{\mathbf{As}} \bullet \mathbf{S} - g_n{}^{\mathbf{As}} \beta_n \mathbf{B} \bullet \mathbf{I}^{\mathbf{As}} + \mathbf{I}^{\mathbf{As}} \bullet \mathbf{P}^{\mathbf{As}} \bullet \mathbf{I}^{\mathbf{As}} + \mathbf{I}^{\mathbf{B}} \bullet \mathbf{A}^{\mathbf{B}} \bullet \mathbf{S} - g_n{}^{\mathbf{B}} \beta_n \mathbf{B} \bullet \mathbf{I}^{\mathbf{B}} + \mathbf{I}^{\mathbf{B}} \bullet \mathbf{P}^{\mathbf{B}} \bullet \mathbf{I}^{\mathbf{B}}$$

Dead-time effects were simulated using a FFT routine (Keijzers *et al*. 1987). Because the observed modulations were weak, the contributions from the ^{10}B and ^{11}B nuclei could be considered independently.

ESEEM spectra (Fig. 4-7) show the presence of a pair of lines centered about the ^{11}B nuclear frequency of ~5.2 MHz. These peaks arise from the excitation of the EPR lines of Center II. Because the splitting varies from ~6 to ~10 MHz, the low frequency branch is observed at frequencies less than 3 MHz and thus tends to overlap with the corresponding ^{10}B peaks which are centered about 1.7 MHz, where the ^{10}B peaks were simulated using the constants from ^{11}B fittings (Table 4-3) and adjusted by the known ratios of nuclear and quadrupole moments. At certain orientations the two ^{10}B can be seen to split into as many as three lines. This arises from the small nuclear quadrupole splitting (Table 4-3). Also observed are $\Delta m_I = 2$ and 3 hyperfine transitions in the range of 15-20 MHz, and 25-30 MHz, respectively.

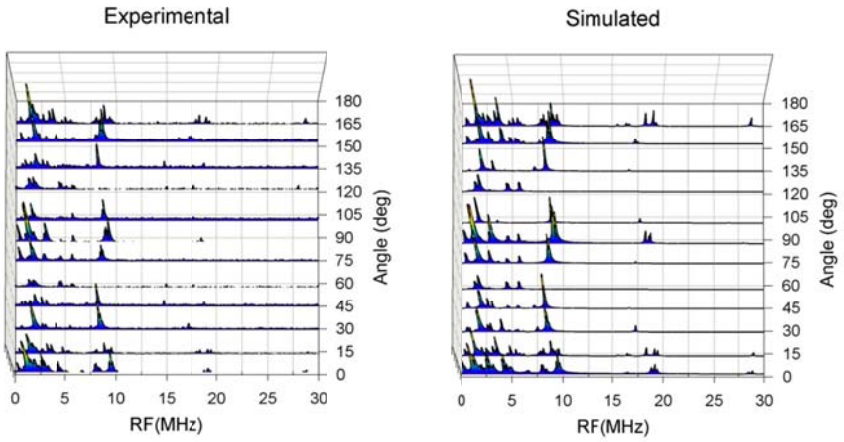

Figure 4-7 Stacked plots of the ^{11}B and ^{10}B portion of the experimental and simulated three-pulse, Fourier-transform ESEEM spectra of Centers I and II in danburite as a function of rotation angles. Intensity in the vertical axis unlabelled (arbitrary unit).

The low-frequency branch occurs in the range of 0 to 3 MHz and differs from the high-frequency branch. Because of the near cancellation of hyperfine and nuclear Zeeman, the resonant ENDOR frequency is found to be sensitive to the second-order effects. This includes not only second-order coupling to ^{75}As nucleus, but also asymmetry in the ^{11}B hyperfine matrix. The best fitting of the position of the low-frequency peak was obtained with an asymmetric ^{11}B hyperfine matrix. Although the ^{11}B is expected to be slightly asymmetric due to the non-coincidence to the **g** and ^{11}B hyperfine matrices, the observed asymmetry is quite large, especially in light of the small anisotropy in **g**. It is not clear where the measured asymmetry is correct or is a result of some unaccounted for second-order interactions.

The ESEEM intensity for an axial or near axial hyperfine coupling is expected to be minimal for orientations parallel and perpendicular to the unique A axis. In Figure 4-7, the intensity of the pair of the ^{11}B peaks spectra for 60° and 120° is close to zero. At these orientations a pair of peaks split by ~1 MHz and centered at the ^{11}B nuclear frequency is still observed. This pair of peaks can also be observed at a number of other orientations and are assigned to the next-nearest-neighbor B. Fitting, assuming an axial hyperfine matrix, gives a much smaller hyperfine coupling (Table 4-3) and a distinctly different orientation for the unique A axis.

Fitting of the limited ESEEM data for Center I gave ^{11}B hyperfine couplings (Table 4-2) that are ~2/3 those of Center II, but the directions of the unique A axes for Centers I and II are almost the same. As with Center II, a small ^{11}B quadrupole tensor is observed. The low-frequency branch of the ^{11}B hyperfine for Center I is

significantly far away from the near cancellation condition, unlike Center II, and as such the ESEEM spectra could be fitted with a symmetric hyperfine matrix (Table 4-2).

4.4 DISCUSSION

4.4.1 Structural models and formation mechanisms for the two $[AsO_2]^{2-}$ radicals

The best-fit matrices **g** and **A**(^{75}As) of the two $[AsO_2]^{2-}$ radicals are similar and are only slightly away from axial symmetry. Centers I and II differ only slightly in their principal A values. The most salient feature of the two $[AsO_2]^{2-}$ radicals is that their unique g and A (^{75}As) axes are approximately perpendicular to the O3–Si–O4 plane in the ideal danburite structure. This result suggests that these two radicals formed from substitutional As^{3+} ions at the Si site. This structural model for the two $[AsO_2]^{2-}$ radicals is further supported by the ^{11}B superhyperfine parameters determined from pulsed ESEEM (Tables 4-2 and 4-3), arising from the nearest-neighbor B nucleus (I and II) and the next-nearest-neighbor B nucleus as well (II; Fig. 4-1).

One possible origin is that an As^{3+} ion substitutes for a Si^{4+} ion and is accompanied by two missing oxygen atoms (O1 and O2) and a next-nearest-neighbor Ca vacancy: i.e. an –O3–As^{3+}–O4– configuration or the $[AsO_2]^{-}$ group. The diamagnetic $[AsO_2]^{-}$ group relative to the unperturbed $[SiO_4]^{2-}$ group is deficient by one negative charge and, therefore, represents an ideal candidate for trapping an electron to form the $[AsO_2]^{2-}$ radical during ionization irradiation. Note that both

Table 4-2 Spin Hamiltonian parameters of $[AsO_2]^{2-}$ (I) in danburite from EPR and ESEEM

Matrix	Matrix Y			Principal values		Principal direction	
				k	Y_k	θ_k (°)	φ_k (°)
(X-band at 295 K)							
g	1.99614(3)	–0.00164(3)	0.00705(3)	1	1.99827(3)	75.2(2)	351.3(6)
		1.99474(4)	0.00412(5)	2	1.99551(4)	77.4(2)	84.7(5)
			1.974195)	3	1.97129(3)	19.5(2)	213.5(2)
A(^{75}As)/h (MHz)	633.4(2)	108.1(3)	283.6(2)	1	732.9(2)	73.1(2)	6.8(2)
		–262.5(3)	39.2(2)	2	–274.6(3)	80.6(2)	99.7(2)
			–212.6(3)	3	–299.9(3)	19.4(2)	217.6(6)
P(^{75}As)/h (MHz)	–28.3(2)	–9.0(2)	–3.5(3)	1	30.0(2)	81.0(3)	99.3(2)
		27.9(2)	4.1(2)	2	0.0(2)	10.5(2)	247(1)
			–0.4(2)	3	–30.0(2)	84.6(2)	95.3(2)
ESEEM at 80 K[a]							
P(^{11}B)/h (MHz)	–0.011	0.016	–0.007	1	0.066	9.5	351.9
		0.063	0.001	2	–0.013	80.4	168.1
			–0.052	3	–0.053	89.3	258.2
A(^{11}B)/h (MHz)	4.69	0.72	–1.12	1	7.74	40.0	231.5
		4.99	–1.43	2	4.11	100.3	154.0
			6.22	3	4.04	128.1	252.2

Polar angle θ is relative to the crystallographic axis c, and azimuth angle φ is relative to axis a. (θ, φ) is equivalent to (180-θ, 180+φ)

a) notes A(^{10}B) = A(^{11}B) *0.335; P(^{10}B) = P(^{11}B) *0.416.

Table 4-3 Spin Hamiltonian parameters of $[AsO_2]^{2-}$ (II) in danburite from EPR and ESEEM

Matrix	Matrix Y			Principal values		Principal direction	
				k	Y_k	θ_k (°)	φ_k (°)
X-band at 295 K							
g	1.99749(4)	–0.00116(2)	0.00386(6)	1	1.99812(4)	82.5(2)	353.9(2)
		1.99216(4)	0.00406(6)	2	1.99292(4)	78.2(2)	85.4(3)
			1.97191(5)	3	1.97053(5)	13.9(2)	232.2(2)
A(^{75}As)/h (MHz)	689.8(3)	145.4(3)	179.5(4)	1	742.6(3)	80.1(2)	8.2(2)
		–289.0(3)	25.2(4)	2	–310.1(2)	87.3(2)	277.7(7)
			–296.8(2)	3	–328.4(3)	10.2(1)	172(2)
P(^{75}As)/h (MHz)	23.5(7)	5.7(2)	6.7(6)	1	27.2(7)	67.2(3)	8.5(2)
		–32.1(5)	7.6(6)	2	6.6(9)	24.8(7)	163(1)
			8.6(9)	3	–33.8(5)	80.4(4)	274.5(2)
X-band EPR and ESEEM at 80 K[a]							
g	1.99676	–0.00108	0.00360	1	1.99734	83.6	99.1
		1.99377	0.00442	2	1.99458	77.8	187.7
			1.97211	3	1.97070	13.9	36.4
A(^{75}As)/h (MHz)	695.7	137.5	176.4	1	745.1	80.3	82.1
		–289.4	30.8	2	–306.8	77.6	169.9
			–305.4	3	–337.3	15.9	28.9
P(^{75}As)/h (MHz)	–28.0	–12.6	–3.3	1	33.4	76.6	348.9
		29.5	6.0	2	4.4	13.8	1.5
			5.8	3	–37.8	87.2	79.6
A'(^{11}B)/h (MHz)	7.09	0.116	-0.78	1	10.59[b]	39.4	233.4
	1.29	7.41	-1.69	2	6.54	96.5	151.3
	-1.72	-1.81	8.82	3	6.19	128.7	246.5
P'(^{11}B)/h (MHz)	–0.014	0.000	0.006	1	0.066	84.4	87.6
		0.065	0.015	2	–0.013	98.8	176.7
			–0.051	3	–0.053	10.4	209.7
A"(^{11}B)/h (MHz)	-0.01	0.44	0.15	1	1.58	72	73
		1.28	0.48	2	-0.15	68	170
			0.01	3	-0.15	29	308

Polar angle θ is relative to the crystallographic axis c, and azimuth angle φ is relative to axis a. (θ, φ) is equivalent to (180-θ, 180+φ)

a) $A(^{10}B) = A(^{11}B) * 0.335$; $P(^{10}B) = P(^{11}B) * 0.416$

b) Principal values and directions obtained on the symmetrized hyperfine matrix.

Table 4-4 Spin Hamiltonian parameters of the $[AsO_3]^{2-}$ center in danburite from EPR at 295 K

Matrix	Matrix Y			Principal values		Principal direction	
				k	Y_k	θ_k (°)	φ_k (°)
g	2.00246(3)	0.00119(2)	–0.00076(4)	1	2.00539(3)	87.5(7)	247.2(5)
		2.00490(3)	0.00014(4)	2	2.00258(4)	51.1(9)	155.2(9)
			2.00165(3)	3	2.00103(3)	38.9(9)	340.3(8)
A(^{75}As)/h (MHz)	1945.2(1)	29.2(1)	–152.0(1)	1	2406.0(1)	20.8(2)	203.3(2)
		1914.9(1)	–74.1(1)	2	1903.4(1)	75.0(2)	72.4(5)
			2341.5(1)	3	1892.1(1)	75.7(2)	338.5(5)
P(^{75}As)/h (MHz)	0.4(10)	0.8(8)	2.8(9)	1	2.8(9)	49(6)	37(73)
		0.9(11)	2(1)	2	1.6(9)	90(36)	127(44)
			–1.4(9)	3	–4.4(9)	40(6)	217(14)

Polar angle θ is relative to the crystallographic axis c, and azimuth angle φ is relative to axis a. (θ, φ) is equivalent to (180-θ, 180+φ)

varieties of the $[AsO_2]^{2-}$ radicals grow with increasing gamma-ray doses, consistent with a radiation-induced origin. The occurrences of these two radicals in as-is crystals are probably attributed to natural irradiation.

Shkrob and Tarasov (2000) noted that structural distortion associated with a neighboring Ca vacancy leads to the two B atoms of the B_2O_7 group to become symmetrically nonequivalent, resulting in the appearances of BOHCs in pairs. Similarly, local distortion associated with a Ca vacancy would make the two Si atoms of the Si_2O_7 group symmetrically nonequivalent, hence explaining the presence of two $[AsO_2]^{2-}$ radicals in this mineral.

4.4.2 Structural model and formation mechanism for the $[AsO_3]^{2-}$ radical

The identification of the $[AsO_3]^{2-}$ radical in danburite is based on the characteristic principal A (^{75}As) values (Serway and Marshall 1966; Dalal *et al.* 1972; Xu 1992; Pöppl *et al.* 1994; Pan 2012). The orientations of the unique g and A axes suggest that this radical in danburite formed from the removal of the bridging O4 atom, with the unpaired spin localized between the oxygen vacancy and the As atom. The experimental A (^{75}As) hyperfine constants (Table 4-4) give a = 2067 MHz and b = 171 MHz, suggesting that ~14% and 51% of the unpaired spin are localized on the arsenic 4*s* and 4p_z orbitals (and the remaining part largely at the oxygen vacancy). Therefore, this type center is similar to many of the other well-established oxygen-vacancy electron centers in various minerals (e.g., E_1' center in quartz; Jani et al. 1983). In this case, the absence of observed ^{17}O and ^{29}Si hyperfine structures can

be attributed to the low abundances of these two isotopes (0.038% and 4.67%, respectively). Similarly, the closest boron nucleus to O4 is ~3.2 Å, hence yielding a ^{11}B superhyperfine structure too small to be resolved by EPR. Attempts to detect the expected ^{11}B superhyperfine structure were not successful, probably owing to the much lower abundance of this center relative to the two $[AsO_2]^{2-}$ radicals (Fig. 4-5b).

Therefore, the $[AsO_3]^{2-}$ radical in danburite can be considered to form from electron trapping on an $[AsO_4]^{3-}$ anion group substituting for the $[SiO_4]^{2-}$ group after removal of the O4 oxygen atom during gamma-ray irradiation. Unlike the $[AsO_2]^{2-}$(I) and $[AsO_2]^{2-}$(II) radicals above, the central arsenic in the $[AsO_3]^{2-}$ radical is in the +5 valence state (Pan 2012). This EPR detection of As^{5+} in danburite, which is not visible in the XAFS spectrum, is another testament to the unsurpassed sensitivity of the EPR technique for structural studies of dilute paramagnetic species.

4.4.3 Local structural environments of As in borosilicates and silicates

The As content of 269 ppm in danburite from Charcas, San Luis Potosi, Mexico, is within the range observed in hemimorphite from various Pb-Zn-Cu deposits worldwide (Mao *et al.* 2010) but is substantially higher than the maximum value of ~3 ppm reported for common silicates (Smedley and Kinniburgh 2002). Significant amounts of As are known to occur in several rare arsenosilicates (e.g. mediate, kraisslite, mcgovernite and nelenite). Also, the substitution of As^{5+} for Si^{4+} in silicates is now well established (Filatov *et al.* 2004; Charnock *et al.* 2007; Mao *et al.* 2010, Nagashima and Armbruster 2010). To the best of our knowledge, however, our XAFS

and EPR results from danburite provide the first compelling evidence for the substitution of As^{3+} for Si^{4+} in silicates. For example, kraisslite, mcgovernite and nelenite of the friedelite group contain still higher amounts of As^{3+} and As^{5+} (Dunn and Nelen 1981; Dunn *et al.* 1988), but their crystal structures remain unknown. Similarly, elevated As contents documented in other silicates are mainly As^{5+} and are generally interpreted to represent surface absorption or contamination from impurities phases (Hattori *et al.* 2005; Pascua *et al.* 2005).

Finally, our XAFS and EPR spectra show that both As^{3+} and As^{5+} preferentially occupy the Si site in the borosilicate danburite. We wish to emphasize that the common $[AsO_3]^{3-}$ and $[AsO_4]^{3-}$ groups are diamagnetic and can be detected by EPR only after they gain or lose one electron during irradiation. Therefore, the absence of any As^{3+} species at the Ca site by the EPR technique does not necessarily contradict the result from modeling of EXAFS spectra. In any case, our results from danburite show that the speciation and local structural environments of arsenic in silicates are complex. Further studies are needed to better understand factors that affect the uptake of arsenic in silicates and their potential applications as sinks and for remediation of arsenic contamination in surface environments.

4.5 REFERENCES

Baur, W.H., Onishi, B.-M.H. (1969): Arsenic. In Handbook of Geochemistry. Wedepohl, K.H. (Editor). Springer-Verlag, Berlin, 33-A-1 - 33-O-5.

Bershov, L.V., Marfunin, A.S. (1967): Electron-spin resonance of electron-hole centers in minerals. *Doklady Akademii nauk SSSR*, **173**: 410 (in Russian).

Charnock, J.M., PolyaO, D.A., Gault, A.G., Wogelius, R.A. (2007): Direct EXAFS evidence for incorporation of As^{5+} in the tetrahedral site of natural andraditic garnet. *The American Mineralogist*, **92**: 1856-1861.

Dalal, N.S., Dickinson, J.R., McDowell, C.A. (1972): Electron paramagnetic resonance studies of X-irradiated KH_2AsO_4, KD_2AsO_4, RbH_2AsO_4, RbD_2AsO_4, CsH_2AsO_4, $NH_4H_2AsO_4$, and $ND_4D_2AsO_4$ (ferroelectrics and antiferroelectrics). *The Journal of Chemical Physics*, **57**: 4254-4265.

Dunn, P.J., Francis, C.A., Innes, J. (1988): A mcgovernite-like mineral and leucophoenicite from the Kombat mine, Namibia. *The American Mineralogist*, **73**: 1182-1185.

Dunn, P.J., Nelen, J.A. (1981): Kraisslite and mcgovernite: new chemical data. *The American Mineralogist*, **65**: 957-960.

Filatov, S.K., Krivovichev, S.V., Burns, P.C., Vergasova, L.P. (2004): Crystal structure of filatovite, $K[(Al,Zn)_2(As,Si)_2O_8]$, the first arsenate of the feldspar group. *European Journal of Mineralogy*, **16**: 537-543.

Geoffroy, M., Llinares, A. (1979): ESR study of radiation-damage in a single-crystal of sodium dimethyl arsenate. *Helvetica Chimica Acta*, **62**: 1605-1613.

Hattori, K., Takahashi, Y., Guillot, S., Johanson B. (2005): Occurrence of arsenic(V) in forearc mantle serpentinites based on X-ray absorption spectroscopy study. *Geochimica et Cosmochimica Acta*, **69**: 5585-5596.

Jani, M.G., Bossoli, R.B., Halliburton, L.E. (1983): Further characterization of the E_1' center in crystalline SiO_2. *Physical Review B*, **27**: 2285-2293.

Jiang, D.T., Chen, N., Sheng, W. (2007): Wiggler-based hard X-ray spectroscopy beamline. *AIP Conference Proceedings*, **879**: 800-803.

Keijzers, C. P., Reijerse, E. J., Stam, P., Dumont, M. F., Gribnau, M. C. M. (1987): MAGRES: A general program for electron spin resonance, ENDOR and ESEEM. *Journal of the Chemical Society. Faraday Transactions*, **83**, 3493–3503.

Knight, L.B., Jones, G.C., King, G.M., Babb, R.M., Mckinley, A.J. (1995): Electron spin resonance and theoretical studies of the PO_2 and AsO_2 radicals in neon matrices at 4 K: Laser vaporization and x-irradiation radical generation techniques. *Journal of Chemical Physics*, **103**: 497-505.

Li, R., Li, Z., Mao, M., Pan, Y. (2011): Single-crystal EPR and DFT studies of a $[BO_4]^0$ center in datolite: Electronic structure, formation mechanism and implications. *Physics and Chemistry of Minerals*, **38**: 33-43.

Li, R., Li, Z., Pan Y. (2012): Single-crystal EPR and DFT study of a $^{VI}Al\text{-}O^{-}\text{-}^{VI}Al$ center in jeremejevite: Electronic structure and ^{27}Al hyperfine constants. *Physics and Chemistry of Minerals*, **39**, 491-501.

Lin, J., Pan, Y., Chen, N., Mao, M., Li, R., Feng, R. (2011): Arsenic incorporation in colemanite from borate deposits: Data from ICP-MS, μ-SXRF, XAFS and EPR analyses. *Canadian Mineralogist*, **49**: 809-822.

Lin, W.C., Mcdowell, C.A. (1964): Electron spin resonance of x-ray irradiated single crystal of disodium hydrogen arsenate $Na_2HAsO_4 \bullet 7H_2O$. *Molecular Physics*, **7**: 223.

Mao, M., Lin, J., Pan, Y. (2010): Hemimorphite as a natural sink for arsenic in zinc deposits and related mine tailings: Evidence from single-crystal EPR spectroscopy and hydrothermal synthesis. *Geochimica et Cosmochimica Acta*, **74**: 2943-2956.

Marshall, S.A., Serway, R.A. (1969): Electron spin resonance absorption spectrum of the AsO_2^{2-} molecule-ion in γ-irradiated single-crystal calcite. *The Journal of Chemical Physics*, **50**: 435-439.

Misra, S.K., Bandet, J., Bacquet, C., McEnally, T.E. (1983): Electron spin resonance studies of defect centers containing boron atoms in natural danburite crystals. *Physica Status Solidi. A. Applied Research*, **80**: 581-588.

Mombourquette, M.J., Weil, J.A., McGavin, D.G. (1996): *EPR-NMR User's Manual*. Department of Chemistry, University of Saskatchewan, Saskatoon, Saskatchewan.

Morton, J.R., Preston, K.F. (1978): Atomic parameters for paramagnetic resonance data. *Journal of Magnetic Resonance*, **30**: 577-582.

Nagashima, M., Armbruster, T. (2010): Ardennite, tiragalloite and mediate: structural control of $(As^{5+},V^{5+},Si^{4+})O_4$ tetrahedra in silicates. *Mineralogical Magazine*, **74**: 55-71.

Nilges, M. J., Pan, Y., Mashkovtsev, R. I. (2009): Radiation-induced defects in quartz. III. W-band EPR, ENDOR and ESEEM study of a peroxy radical. *Physics and Chemistry of Minerals*, **36**, 61-73.

Novozhilov, A.I., Nosv. S.P., Gorbacheva, G.A., Samoilovich, M.I. (1988): EPR and optical absorption of color centers in danburite. *Mineral. Zh.* **10**: 85-88 (in Russian).

O'Day, P.A. (2006): Chemistry and mineralogy of arsenic. *Elements*, **2**: 77-83.

Pan, Y. (2012): Arsenic speciation in rock-forming minerals determined by EPR spectroscopy. In: Arsenic: Sources, Environmental Impact, Toxicity and Human Health - A Medical Geology Perspective (A. Masotti, ed.), Nova Science Pub Inc (in press)

Pascua, C., Charnock, J., Polya, D.A., Sato, T., Yokoyama, S., Minato, M. (2005): Arsenic-bearing smectite from the geothermal environment. *Mineralogical Magazine*, **69**, 897-906.

Phillips, M.W., Gibbs, G.V., Ribbe, P.H. (1974): The crystal structure of danburite: a comparison with anorthite, albite, and reedmergnerite. *American Mineralogist*, **59**: 79-85.

Pöppl, A., Tober, O., Völkel, G. (1994): ESR study of the AsO_3^{2-} radical in γ-irradiated betaine arsenate. *Physical Status Solidi B*, **183**: K63-K66.

Rehr, J.J., Albers, R.C. (2000): Theoretical approaches to x-ray absorption fine structure. *Reviews of Modern Physics*, **72**: 621-654.

Ressler, T. (1997): WinXAS: A new software package not only for the analysis of energy-dispersive XAS data. *Journal de Physique IV*, **7(C2)**: 269-270.

Serway, R.A., Marshall, S.A. (1966): Electron spin resonance absorption spectrum of the AsO_3^{2-} molecule ion in γ–irradiated single–crystal calcite. *Journal of Chemical Physics*, **45**: 2309-2314.

Shkrob, I.A., Tarasov, V.F. (2000): On the structure of trapped hole in borosilicates. *Journal of Chemical Physics*, **113**: 10723-10732.

Smedley, P.L., Kinniburgh, D.G. (2002): A review of the source, behaviour and distribution of arsenic in natural waters. *Applied Geochemistry*, **17**: 517-568.

Xu, R. (1992): EPR studies of AsO_3^{2-} centers in $MgNH_4PO_4 \cdot 6H_20$ (struvite) crystals. *Physical Status Solidi B*, **172**: K15-K18.

CHAPTER 5

Single-crystal EPR and DFT study of a ^{VI}Al–O^{-}–^{VI}Al center in jeremejevite: electronic structure and ^{27}Al hyperfine constants

Single-crystal electron paramagnetic resonance (EPR) spectra of a gem-quality jeremejevite, $Al_6B_5O_{15}(F,OH)_3$, from Cape Cross, Namibia, reveal an S = 1/2 hole center characterized by an ^{27}Al hyperfine structure arising from interaction with two equivalent Al nuclei. Spin-Hamiltonian parameters obtained from single-crystal EPR spectra at 295 K are as follows: g_1 = 2.02899(1), g_2 = 2.02011(2), g_3 = 2.00595(1); $A_1/g_e\beta_e$ = −0.881(1) mT, $A_2/g_e\beta_e$ = −0.951(1) mT, and $A_3/g_e\beta_e$ = −0.972(2) mT, with the orientations of the g_3- and A_3- axes almost coaxial and perpendicular to the Al−O−Al plane; and those of the g_1- and A_1- axes approximately along the Al−Al and Al−OH directions, respectively. These results suggest that this aluminum-associated hole center represents hole trapping on a hydroxyl oxygen atom linked to two equivalent octahedral Al^{3+} ions, after the removal of the proton (i.e., a ^{VI}Al–O^{-}–^{VI}Al center). Periodic *ab initio* UHF and DFT calculations confirmed the experimental ^{27}Al hyperfine coupling constants and directions, supporting the proposed structural model. The ^{VI}Al–O^{-}–^{VI}Al center in jeremejevite undergoes the onset of thermal decay at 300 ºC and is completely bleached at 525 ºC. These data obtained from the ^{VI}Al–O^{-}–^{VI}Al center in jeremejevite provide new insights into analogous centers that have been documented in several other minerals.

5.1 INTRODUCTION

Aluminum-associated oxygen hole centers are common radiation-induced defects in oxides, aluminosilicates, and other minerals, and have attracted much attention, because they have a host of applications from dosimeters to geochronometers, exert important influences on the catalytic and other properties of their host materials, and have direct relevance to nuclear waste disposal (Adrian *et al.* 1985; Ikeya 1993; Clozel *et al.* 1995; To *et al.* 2005; Mao *et al.* 2010). For example, radiation-induced defects involving hole trapping on a single oxygen atom (O^-) bonded to a nearest-neighbor Al atom in tetrahedral and octahedral coordinations are commonly denoted as $[AlO_4]^0$ and $[AlO_6]^0$, respectively (Nuttall and Weil 1981; To *et al.* 2005; Schirmer 2006; Dias *et al.* 2009; Mao *et al.* 2010). Other types of aluminum-associated oxygen hole centers involving hole trapping on two oxygen atoms in a superoxide configuration (O_2^-) linked to a nearest- or next-nearest-neighbor Al have been reported as well (Nilges *et al.* 2008, 2009; Pan *et al.* 2008, 2009).

Similarly, O^- centers associated with two neighboring Al atoms are known as well. Of these, the $^{IV}Al{-}O^-{-}^{IV}Al$ centers involving hole trapping on a bridging oxygen between two AlO_4 tetrahedra have been reported in feldspars and zeolites (Ioffe and Yanchevskaya 1968; Marfunin and Bershov 1970; Speit and Lehmann 1976, 1982; Matyash *et al.* 1982; Hofmeister and Rossman 1985; Wichterlová *et al.* 1988; Petrov *et al.* 1989; Petrov 1994; Mittani *et al.* 1999) and received particular interests, because they provide direct evidence for the violation of Al avoidance rule (Loewenstein

1954). However, their characteristic ^{27}Al hyperfine structures were generally assumed to be isotropic (Table 5-1) and had not been quantitatively analyzed. Similarly, Barklie *et al.* (1983) reported an ^{IV}Al–O^{-}–^{IV}Al center in β-alumina and determined its ^{27}Al hyperfine constants and quadrupole parameters from EPR and electron nuclear double resonance (ENDOR) spectra by assuming an axial symmetry (Table 5-1).

Also, centers of the ^{VI}Al–O^{-}–^{VI}Al type involving hole trapping on an oxygen atom linked to two octahedral coordinated Al atoms have been proposed to occur in kaolinite (i.e., the "B-centers", Clozel *et al.* 1995). However, the structural model of this defect in kaolinite remains controversial because of limited data available from the powder EPR techniques (Clozel *et al.* 1995; Köksal *et al.* 2004). Similarly, Krambrock *et al.* (2004) and da Silva *et al.* (2005) reported the occurrences of ^{VI}Al–O^{-}–^{VI}Al centers in gamma-ray irradiated elbaite and neutron-irradiated topaz (Table 5-1). These authors noted several challenges in quantitative analysis for the spin-Hamiltonian parameters of these ^{VI}Al–O^{-}–^{VI}Al centers: (1) large number of nuclear transitions arising from interaction with two I = 5/2 ^{27}Al nuclei, (2) severe overlapping among these nuclear transitions (i.e., only 11 lines for two equivalent ^{27}Al nuclei), and (3) small anisotropy of the ^{27}Al hyperfine structures (da Silva *et al.* 2005). For example, Krambrock *et al.* (2004) obtained the ^{27}Al hyperfine constants for the ^{VI}Al–O^{-}–^{VI}Al center in elbaite (Table 5-1) from ENDOR spectra by assuming the axial symmetry observed in the EPR spectra.

During the course of our single-crystal EPR investigation on radiation-induced defects in borates and borosilicates (Li *et al.* 2011), we have measured a sample of

Table 5-1 Examples of aluminum-associated oxygen hole centers

Host	Center	Principal *g*-factor values			Principal A (^{27}Al) values (mT)			References
		g_1	g_2	g_3	$A_1/g_e\beta_e$	$A_2/g_e\beta_e$	$A_3/g_e\beta_e$	
Quartz	$[AlO_4]^0$	2.060208(2)	2.008535(2)	2.001948(2)	−0.6127(3)	−0.6187(3)	−0.5037(3)	Nuttall and Weil (1981)
Prehnite	$[AlO_6]^0$	2.04868(1)	2.02357(1)	2.00242(1)	−0.615(2)	−0.750(2)	−0.758(2)	Mao *et al.* (2010)
Albite	^{IV}Al−O−^{IV}Al: c_0	2.065(0)	2.023(2)	2.000(6)	~0.89	~0.89	~0.89	Petrov *et al.* (1989)
Albite	^{IV}Al−O−^{IV}Al: c_0	2.077(8)	2.026(2)	1.998(1)	~0.89	~0.89	~0.89	Petrov *et al.* (1989)
Albite	^{IV}Al−O−^{IV}Al: d_0	2.056(2)	2.013(7)	2.009(0)	~0.89	~0.89	~0.89	Petrov *et al.* (1989)
Albite	^{IV}Al−O−^{IV}Al: c_m	2.076(1)	2.026(2)	1.998(5)	~0.89	~0.89	~0.89	Petrov *et al.* (1989)
β-alumina	^{IV}Al−O−^{IV}Al	2.0340(6)	2.0018(6)	2.0018(6)	0.76(1)	0.86(4)	0.86(4)	Barklie *et al.* (1983)
Kaolinite	^{VI}Al−O$^-$−^{VI}Al	2.040(5)	2.020(5)	2.002(5)	0.71	0.77	0.84	Clozel *et al.* (1995)
Elbaite	^{VI}Al−O$^-$−^{VI}Al	2.050(3)	2.050(3)	2.002(2)	−0.79	−0.85	−0.85	Krambrock *et al.* (2004)
Topaz	^{VI}Al−O$^-$−^{VI}Al	2.1287(3)	2.0091(4)	1.9985(4)	0.90	0.90	1.05	da Silva *et al.* (2005)

gem-quality jeremejevite $Al_6B_5O_{15}(F, OH)_3$ from Cape Cross, Namibia, and encountered a new oxygen hole center with a ^{27}Al hyperfine structure arising from interaction with two Al nuclei. The structure of jeremejevite (space group $P6_3/m$) consists of $Al(O, F)_6$ octahedra and BO_3 triangles, and the $Al(O, F)_6$ octahedra share edges to form chains along the **c**-axis (Fig. 5-1; Golovastikov *et al.* 1955; Rodellas *et al.* 1983). Our single-crystal EPR spectra suggest that this aluminum-associated oxygen hole center in jeremejevite is of the $^{VI}Al–O^{-}–^{VI}Al$ type. Moreover, we have succeeded in obtaining ^{27}Al hyperfine parameters of the $^{VI}Al–O^{-}–^{VI}Al$ center by a combination of "trial-and-error" spectral simulations and conventional fitting of angular-dependence line-position data from single-crystal EPR spectra. In addition, we have performed periodic density functional theory (DFT) calculations to confirm the experimental ^{27}Al hyperfine coupling constants and to provide additional information for the geometry and electronic structure of the $^{VI}Al–O^{-}–^{VI}Al$ center in jeremejevite. These results obtained from the $^{VI}Al–O^{-}–^{VI}Al$ center in jeremejevite provide new insights into analogous defects in other minerals (Clozel *et al.* 1995; Krambrock *et al.* 2004; da Silva *et al.* 2005).

5.2 SAMPLE, EXPERIMENTAL TECHNIQUES AND DFT CALCULATIONS

5.2.1 Jeremejevite crystal and sample preparation

A gem-quality jeremejevite crystal of pale blue color and hexagonal prismatic form (~2 mm × 2 mm × 10 mm in size) from Cape Cross, Namibia, was investigated in this study. Foord *et al.* (1981) noted that jeremejevite from this locality is

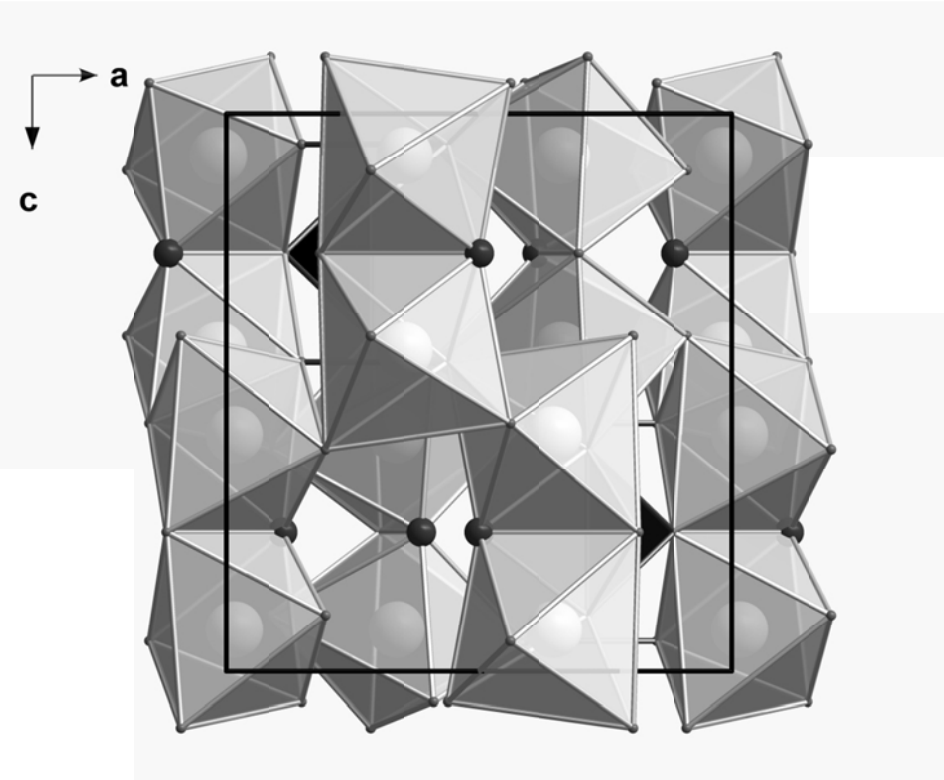

Figure 5-1 Crystal structure of jeremejevite illustrating that [AlO_5F] octahedral share edges to form chains along the **c**-axis (data from Rodellas *et al.* 1983). *Solid black spheres* represent F atoms.

compositionally zoned and interpreted its "cornflower blue" coloration in the rim to either "cation-trapped" or "inorganic-radical-trapped" electrons or holes. Foord *et al.* (1981) also confirmed the presence of the OH group in the jeremejevite crystals from Namibia by the use of optical spectroscopic data. In our study, the large crystal was cut into three pieces (~ 2 mm × 2 mm × 3 mm each) for single-crystal EPR measurements. Isochronal annealing experiments for one of these pieces at atmospheric pressure and a constant duration of 10 minutes each step were made in a Thermolyne muffle furnace for the temperature range from 100 ºC to 525 ºC at a step of every 25 ºC. Gamma-ray irradiation of the annealed crystal was made at room temperature in a ^{60}Co cell with a dose rate of ~ 460 Gy/hr for up to 5 days.

5.2.2 Single-crystal EPR experiments

All single-crystal EPR spectra were measured on a Bruker EMX spectrometer at the Saskatchewan Structural Sciences Centre, University of Saskatchewan, equipped with an automatic frequency controller, an ER4119 cavity, an Oxford liquid helium-liquid nitrogen cryostat, and an ER218G1 goniometer with an angle uncertainty of ~0.2°.

Single-crystal EPR measurements were taken at temperatures from 295 K to 85 K. Crystal alignment was accomplished by use of its prismatic form. Detailed single-crystal EPR spectra were collected for two orthogonal rotation planes: one perpendicular to the crystallographic axis **c** and another parallel to the **c**-axis. Experimental conditions for spectral measurements included a microwave frequency

of ~9.39 GHz, modulation frequency of 100 kHz, modulation amplitude of 0.1 mT, microwave power of 2 mW, spectral resolution of ~0.02 mT (i.e., 1,024 data points over 20 mT), and angle interval of 5°. Magnetic field calibrations were made by the use of free radical α, γ-bis-diphenylene-β-phenyl allyl in benzene (BDPA; g = 2.0027).

Single-crystal EPR measurements of jeremejevite after each step of isochronal annealing were made at room temperature with the magnetic field $\mathbf{B} // \mathbf{a}$. Crystal alignment of this type was made first by the use of prismatic form and then adjusted on the basis of coalesce of magnetically nonequivalent site in this orientation.

5.2.3 Computation methodology

Periodic DFT calculations have been done using the supercell approach and hybrid functionals from open-shell B3LYP (Becke 1993a) to BHHLYP (Becke 1993b), UHF and PBE0 (Adamo and Barone 1999) as implemented in CRYSTAL06 (Dovesi *et al.* 2006). All-electron basis sets used in this study are those known to be well suitable for periodic calculations, and they are the 8-511G* of Gatti *et al.* (1994) for Al, standard 6-31G* for O, 7-311G of Nada *et al.* (1993) for F, and the def2-TZVP of Weigend and Ahlrichs (2005) for B, except that diffuse functions with exponents <0.1 were removed with the outmost d and the f functions to avoid linear correlation and integration problems in the calculations.

The thresholds for the overlap and penetration Coulomb integrals, the overlap for Hartree-Fock (HF) exchange integrals, and the two pseudo-overlaps for HF series were set to 10^{-8}, 10^{-8}, 10^{-8}, 10^{-8}, and 10^{-18} hartree, respectively, while a tight SCF

tolerance of 10^{-8} hartree was chosen. Moreover, the extra-large grid (XLGRID) that employs the pruned (75,974) grid for each atom was used, which is much more accurate than the default (55,434) grid in description of the optimized charge and spin densities as well as the defect structures in the crystal. The Pack-Monkhorst shrink factor was set to 6 for the unit-cell geometry optimization and 4 for a 116-atoms supercell containing two primitive cells, giving a total of 112 and 36 *k* points in the irreducible Brillouin zone, respectively. The same shrink factor was doubled for the Gilat net to describe the Fermi surface of the system (Dovesi *et al.* 2006).

The atomic coordinates of jeremejevite reported by Rodellas *et al.* (1983) were used for the optimization of the perfect structure $Al_6B_5O_{15}F_3$. The resulting optimized structure was used in the subsequent defect calculations with one central F atom replaced by an O atom. From the converged spin densities for the defect, ^{27}A1 and ^{17}O hyperfine and quadrupole coupling constants were calculated.

5.3 RESULTS

5.3.1 Single-crystal EPR spectra

Reconnaissance single-crystal EPR spectra of jeremejevite reveal the presence of an Fe^{3+} center ($S = 5/2$) at the effective *g*-factor value of 4.28 and a multiplet at $g = \sim 2$ (Fig. 5-2). However, measurements down to 85 K did not detect any notable improvement in the signal-to-noise ratio of the multiplet. Consequently, our detailed single-crystal EPR measurements for the two rotation planes were taken at 295 K.

Figure 5-2a shows that the multiplet at $g = \sim 2$ measured with the magnetic field **B**

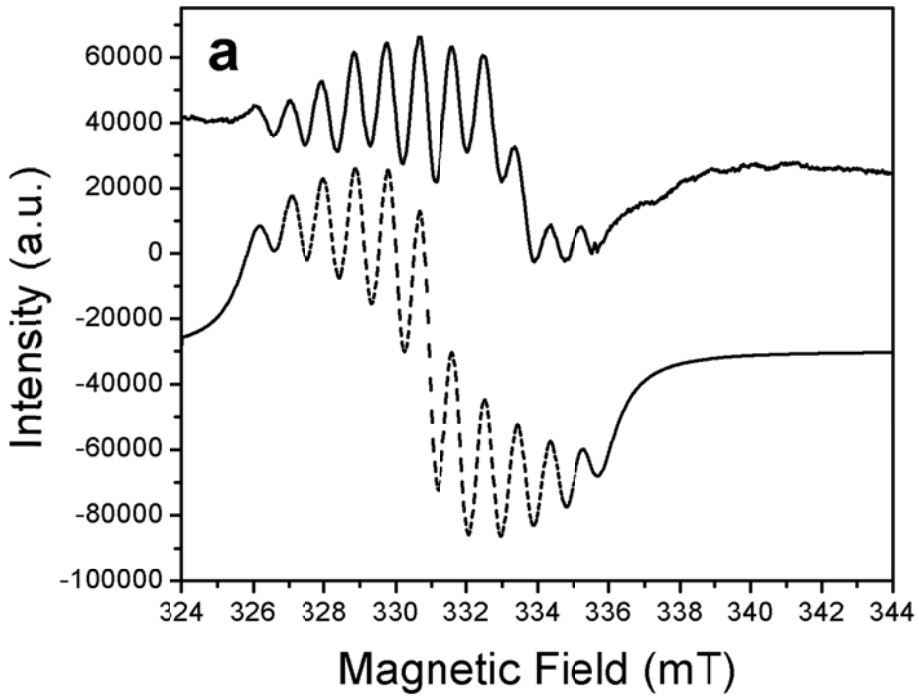

Figure 5-2a Representative single-crystal EPR spectra (*solid line*) measured at 295 K and microwave frequency (ν) of ~9.39 GHz with magnetic field approximately parallel to the **c**-axis. Also shown for comparison are simulated spectra (dashed lines) at the same crystal orientations.

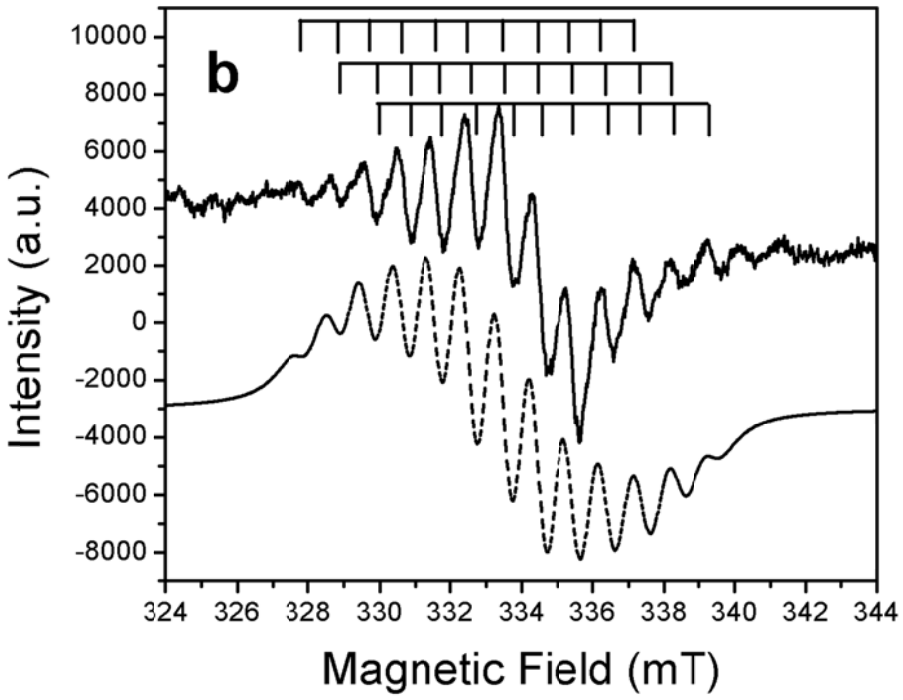

Figure 5-2b Representative single-crystal EPR spectra (*solid line*) measured at 295 K and microwave frequency (ν) of ~9.39 GHz with magnetic field is approximately 10° away from **a**-axis. Also shown for comparison are simulated spectra (dashed lines) at the same crystal orientations. Note that additional *weak lines* (?) in the high field are of uncertain origin.

approximately parallel to the crystallographic axis **c** consists of 11 equidistant lines, with the relative intensities of 1:2:3:4:5:6:5:4:3:2:1. These lines are attributable to hyperfine interaction of a single unpaired electron (S = 1/2) with two equivalent I = 5/2 nuclei of ~100% natural abundance. Considering the crystal structure and composition of jeremejevite, these nuclei are identified as ^{27}Al. This hyperfine structure, together with fitted principal g values (see below), allows us to identify the center as an aluminum-associated oxygen hole center of the Al−O$^-$−Al type.

Away from crystallographic axes, however, the EPR spectra are complicated. For example, the spectrum measured with **B^a** =10° consists of 13 lines, which have been shown by spectral simulations to arise from three sets of 11 lines (Fig. 5-2b). These three sets of 11 lines are observed in both rotation planes (Fig. 5-3) and are attributable to three magnetically nonequivalent sites, indicative of a C_{2h} symmetry of this defect (Rae 1969). The average line widths of individual peaks are ~0.48 mT, which are attributable to both unsolved site splittings and overlapping hyperfine lines.

5.3.2 Spectral simulations and optimization of spin-Hamiltonian parameters

The single-crystal EPR spectra of the Al−O$^-$−Al center in jeremejevite can be described by a spin-Hamiltonian of the form:

$$\boldsymbol{H_S} = \beta_e \mathbf{S} \bullet \mathbf{g} \bullet \mathbf{B} + \sum_{i=0}^{2} \mathbf{I} \bullet \mathbf{A} \bullet \mathbf{S} + \sum_{i=0}^{2} \mathbf{I} \bullet \mathbf{P} \bullet \mathbf{I} - g_n \beta_n \mathbf{I} \bullet \mathbf{B}$$

where β_e and β_n are the electron and nuclear magneton, respectively; **S** and **I** are the electron-spin and nuclear-spin operators, respectively; **g** is the Zeeman electron term; **A** is the nuclear hyperfine term; and **P** is the nuclear quadrupole tensor. All spectral

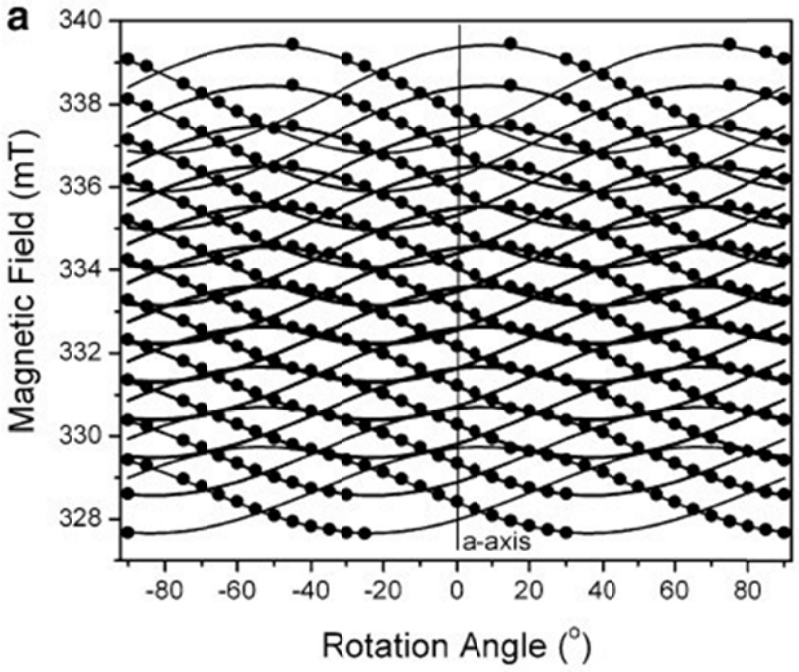

Figure 5-3a Line-position data versus rotation angle (i.e., roadmap) of the $^{VI}Al{-}O^{-}{-}^{VI}Al$ center in jeremejevite in (0001) crystal face measured at 295 K and ν = ~9.39 GHz. *Solid circles* represent experimental data points; and *solid lines* are predicted from spin-Hamiltonian parameters in Table 5-2.

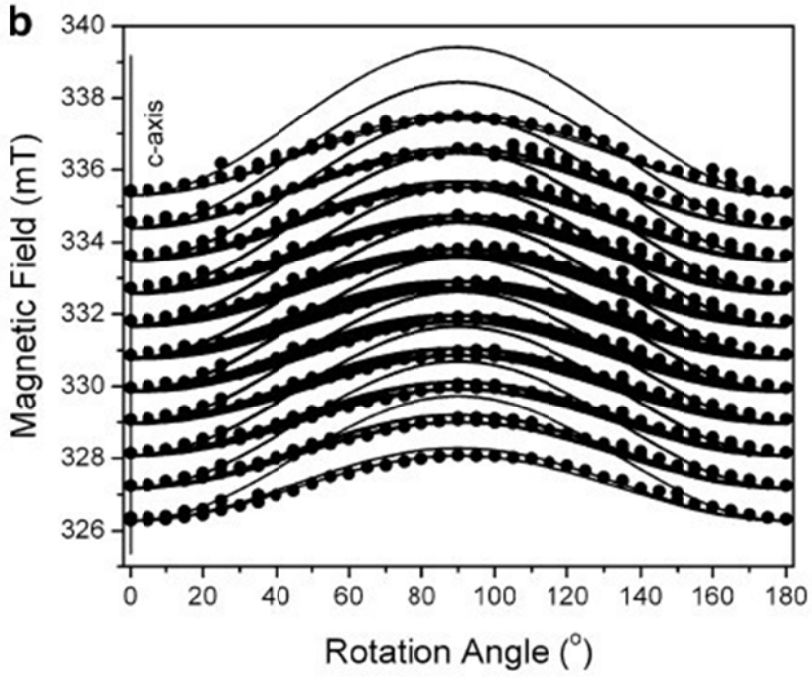

Figure 5-3b Line-position data versus rotation angle (i.e., roadmap) of the $^{VI}Al{-}O^{-}{-}^{VI}Al$ center in jeremejevite in a rotation plane parallel to the **c**-axis measured at 295 K and ν = ~9.39 GHz. *Solid circles* represent experimental data points; and *solid lines* are predicted from spin-Hamiltonian parameters in Table 5-2.

simulations and optimization of spin-Hamiltonian parameters were made by the use of a modified version of the EPR-NMR software package (Mombourquette *et al.* 1996). Specifically, initial spectral analysis commenced with interpreted main absorption lines (i.e., ignoring the ^{27}Al hyperfine splitting; see also da Silva *et al.* 2005 and taking the normal directions of the two rotation planes at (θ = 0°,φ = 0°) and (90°, 40°), where θ and φ are the tilting angles relative to crystallographic axes **c** and **a**, respectively). This analysis with steps of angle corrections allowed us to obtain the matrix **g** and determine the actual orientations of the two measured planes at (1.0°, 1.4°) and (90.2°, 40.5°), indicating only minor crystal misalignments for the two rotation planes.

Subsequently, spectral simulations with "trial" **A** (^{27}Al) matrices and "zero" **P** (^{27}Al) tensors were made for all measured crystal orientations to (1) confirm the site assignments used during the fitting of the matrix **g** and (2) determine the nuclear transitions arising from the two ^{27}Al nuclei. Finally, conventional fittings of spin-Hamiltonian parameters were made with line-position data points from experimental spectra and transition labels from spectral simulations. The total numbers of line-position data points used for fitting in the rotation group C_6 is 4,036. The final value of the root-mean-squares of weighted differences (RMSD) between the calculated and observed line positions is 0.047 mT (Table 5-2), which is only one-tenth of the average line width at ~0.48 mT. The signs of the hyperfine coupling constants cannot be determined from fitting of EPR spectra alone. Following previous experimental and theoretical results (Nuttall and Weil 1981; Krambrock *et al.* 2004;

Table 5-2 Spin-Hamiltonian parameters of the ^{VI}Al–O^{-}–^{VI}Al center in jeremejevite at 295 K

	Matrix (Y)			k	Principal values (Y_k)	Principal directions		RMSD (mT)
						θ_k (°)	φ_k (°)	
	2.01484(1)	0.00684(1)	0.00000(1)	1	2.02899(1)	0.0(2)	252.4*	
g		2.01122(2)	0.00000(1)	2	2.02011(2)	90.0(9)	37.6(2)	
			2.02899(1)	3	2.00595(1)	90.0(2)	127.6(2)	
	−0.946(1)	0.024(2)	0.030(1)	1	-0.881(1)	41(1)	39(1)	
^{27}Al$_1$ $\mathbf{A_1}/g_e\beta_e$ (mT)		−0.945(2)	0.019(1)	2	-0.951(1)	51(1)	245(5)	0.047
			−0.912(1)	3	-0.972(2)	77(3)	144(3)	
	−0.946(1)	0.024(1)	−0.030(1)	1	−0.881(1)	40(1)	219(1)	
^{27}Al$_2$ $\mathbf{A_2}/g_e\beta_e$ (mT)		−0.945(2)	−0.019(1)	2	−0.951(1)	51(1)	65(5)	
			−0.912(2)	3	−0.972(2)	77(3)	324(3)	

Results reported here are for one of six symmetrically equivalent sites in the rotation group C_6. Polar angle θ is relative to the crystallographic axis **c**, and azimuth angle φ is relative to axis **a**. (θ, φ) is equivalent to (180 − θ, 180 + φ).
* Azimuth angle is meaningless at θ ≈ 0°.

Nilges *et al.* 2009; Botis and Pan 2010), we adopted a negative sign for the isotropic part of the ^{27}Al hyperfine constants. Note that nuclear quadrupole effects are negligible and therefore not included in Table 5-2. Further spectral simulations (Fig. 5-2) show that the fitted spin-Hamiltonian parameters (Table 5-2) reproduce the observed EPR spectra very well.

The fitted matrix **g** is of rhombic symmetry, whereas the two equivalent matrices **A** (^{27}Al) are approximately axial in symmetry (Table 5-2). In particular, the orientations of the g_3 and A_3 principal axes are approximately coaxial and are perpendicular to the Al−F−Al plane in the ideal jeremejevite structure (Fig. 5-1). The orientation of the g_1-axis along the **c**-axis is also consistent with the Al−Al direction; and the orientations of the two A_1-axes at (41º, 39º) and (40º, 219º) are close to the <Al−F> bond directions (37.9°, 33.5°) and (37.9°, 213.5°) (Fig. 5-1). These relationships confirm the Al−O$^-$−Al center in jeremejevite to involve two octahedral coordinated Al atoms, hence the notation ^{VI}Al−O$^-$−^{VI}Al.

5.3.3 Thermal stability

Single-crystal EPR measurements of isochronally annealed jeremejevite show that the ^{VI}Al−O$^-$−^{VI}Al center remains unaffected up to 275 ºC but starts to decrease in intensity at 300 ºC and is completely annealed out at 525 ºC (Fig. 5-4). Interestingly, the blue coloration of this sample is similar in thermal behavior (i.e., completely bleached at 525 ºC). Therefore, a linkage between this color and the ^{VI}Al−O$^-$−^{VI}Al center is tempting (cf., da Silva *et al.* 2005) but requires further studies. Single-crystal

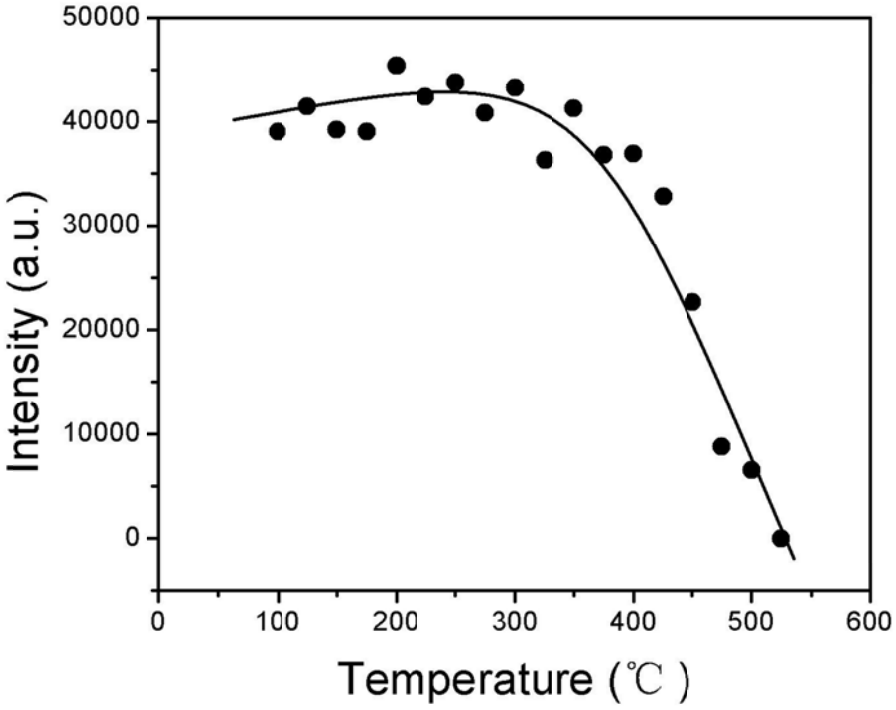

Figure 5-4 Intensities of the $^{VI}Al{-}O^{-}{-}^{VI}Al$ center (i.e., peak-to-peak height of the lowest-field hyperfine line from 295 K single-crystal EPR spectra measured at magnetic field parallel to an **a**-axis) as a function of isochronal annealing temperature from 100 to 525℃.

EPR measurements of this annealed crystal after gamma-ray irradiation for a dose of up to 55.2 kGy reveal the presence of a $[BO_3]^{2-}$ center (Eachus and Symons 1968; Bershov and Marfunin 1981; Li and Pan 2011). However, there is no evidence for any restoration of the $^{VI}Al–O^{-}–^{VI}Al$ center or the blue color. One plausible explanation for the failure to restore the $^{VI}Al–O^{-}–^{VI}Al$ center by gamma-ray radiation is the formation of competing paramagnetic centers such as the $[BO_3]^{2-}$ center.

5.3.4 UHF and DFT results

Table 5-3 shows that calculated unit-cell parameters, bond distances and angles using various functionals are all in agreement with experimental data (Foord *et al.* 1981; Rodellas *et al.* 1983). Calculations for the defective structure have been performed for both the primitive cell and the 116-atoms supercell. These calculations show that the supercell size has minimal effects on the calculated defect structure. Therefore, only results from the 116-atoms supercell are presented herein. Table 5-4 reports the Al-O bond distances and spin populations of the $^{VI}Al–O^{-}–^{VI}Al$ center in jeremejevite. The most notable change is that the Al-O_F bond distances are 0.037-0.048 Å longer than the original Al-F bond. All calculations also show >90% of the unpaired spin is localized on the substitutional oxygen atom at the F site (Fig. 5-5, Table 5-4) and that the two Al atoms contain small negative spin arising from spin polarization.

Table 5-5 shows that the calculated A (^{27}Al) hyperfine constants and orientations of the two Al atoms are in agreement with experimental data. The largest

Table 5-3 Comparison between experimental and theoretical unit-cell constants and selected bond lengths and angles of ideal jeremejevite ($Al_6B_5F_3O_{15}$)

	XRD[a]	XRD[b]	B3LYP	BHHLYP	UHF	PBE0
a (Å)	8.556	8.5571	8.570	8.524	8.556	8.551
c	8.175	8.1763	8.211	8.171	8.199	8.194
c/a	0.9555	0.9555	0.9582	0.9585	0.9584	0.9583
V ($Å^3$)	518.29	518.49	522.25	514.17	519.81	518.88
Al−O_1 (Å)	1.917	−	1.916	1.909	1.922	1.911
Al−O_2	1.891	−	1.890	1.879	1.886	1.886
$Al-O_2^{v}$	1.905	−	1.905	1.895	1.903	1.902
$Al-O_3^{xi}$	1.931	−	1.945	1.935	1.946	1.939
$Al-O_1^{xii}$	1.863	−	1.865	1.856	1.861	1.863
Al−F	1.810	−	1.813	1.799	1.793	1.811
Al−F−Al (°)	104.17	−	105.67	106.11	107.2	105.4

Labels of the oxygen atoms after Rodellas *et al.* (1983)
a Rodellas *et al.* (1983)
b Foord *et al.* (1981)

Table 5-4 Calculated bond distances and spin populations of the ^{VI}Al–O^{-}–^{VI}Al center in jeremejevite using a 116 atom supercell

	B3LYP		BHHLYP		UHF		PBE0	
	d (Å)	Spin (e)	*d* (Å)	Spin (e)	*d* (Å)	Spin (e)	*d* (Å)	Spin (e)
Al_1	–	−0.011	–	−0.013	–	−0.016	–	−0.012
O_F	1.852	0.934	1.847	0.982	1.858	1.016	1.852	0.951
O_1^{xii}	1.870	0.000	1.847	0.000	1.855	0.000	1.861	0.000
O_2	1.909	0.015	1.885	0.008	1.901	0.004	1.899	0.013
O_2^{v}	1.926	0.023	1.897	0.012	1.921	0.007	1.911	0.019
O_1	1.924	0.000	1.898	0.000	1.914	−0.001	1.913	0.000
O_3^{xi}	1.964	0.001	1.933	0.000	1.955	−0.001	1.948	0.001
Al_2	–	−0.011	–	−0.013	–	−0.016	–	−0.012
O_F	1.852	0.934	1.847	0.982	1.858	1.016	1.852	0.951
O_1^{xii}	1.870	0.000	1.847	0.000	1.855	0.000	1.861	0.000
O_2	1.908	0.015	1.886	0.008	1.901	0.004	1.899	0.013
O_2^{v}	1.927	0.023	1.896	0.012	1.921	0.007	1.910	0.019
O_1	1.925	0.000	1.897	0.000	1.914	−0.001	1.913	0.000
O_3^{xi}	1.964	0.001	1.934	0.000	1.954	−0.001	1.949	0.001

Labels of oxygen atoms are same as those in Table 5-3.

Table 5-5 Calculated ^{27}Al and ^{17}O hyperfine and quadruple coupling constants of the ^{VI}Al–O^{-}–^{VI}Al center in jeremejevite using a 116 atom supercell

	B3LYP	BHHLYP	UHF	PBE0			Experimental		
	Value	Value	Value	Value	θ	φ	Value	θ	φ
$^{27}Al_1$									
$a_{iso}/g_e\beta_e$ (mT)	−0.780	−0.786	−0.990	−0.774	–	–	−0.934	–	–
$A_1/ g_e\beta_e$	−0.692	−0.705	−0.950	−0.687	39.0	40.4	−0.881	41	39
$A_2/ g_e\beta_e$	−0.825	−0.828	−1.012	−0.819	54.9	250.4	−0.951	51	245
$A_3/ g_e\beta_e$	−0.823	−0.826	−1.007	−0.817	75.1	149.6	−0.972	77	144
$P_1/ g_e\beta_e$	0.012	0.011	0.012	0.011	59.2	259.9	–	–	–
$P_2/ g_e\beta_e$	0.001	0.001	0.001	0.001	72.4	159.0	–	–	–
$P_3/ g_e\beta_e$	−0.014	−0.012	−0.013	−0.012	36.5	43.6	–	–	–
$^{27}Al_2$									
$a_{iso}/g_e\beta_e$ (mT)	−0.779	−0.786	−0.989	−0.774	–	–	−0.934	–	–
$A_1/ g_e\beta_e$	−0.691	−0.705	−0.950	−0.687	39.0	220.4	−0.881	40	219
$A_2/ g_e\beta_e$	−0.824	−0.828	−1.011	−0.819	55.0	70.7	−0.951	51	65
$A_3/ g_e\beta_e$	−0.822	−0.826	−1.006	−0.817	74.9	329.8	−0.972	77	324
$P_1/ g_e\beta_e$	0.012	0.011	0.012	0.011	59.2	79.9	–	–	–
$P_2/ g_e\beta_e$	0.001	0.001	0.001	0.001	72.4	339.0	–	–	–
$P_3/ g_e\beta_e$	−0.014	−0.012	−0.013	−0.012	36.5	223.6	–	–	–
$^{17}O_F$									
$a_{iso}/g_e\beta_e$ (mT)	−3.330	−3.651	−4.961	−3.308	–	–	−2.594[a]	–	–
$A_1/ g_e\beta_e$	0.933	0.751	−0.546	0.999	90.0	131.4	1.527	–	–
$A_2/ g_e\beta_e$	0.919	0.731	−0.576	0.980	0.0	306.4	1.788	–	–
$A_3/ g_e\beta_e$	−11.842	−12.435	−13.761	−11.902	90.0	41.4	−11.098	–	–
$P_1/ g_e\beta_e$	−0.025	−0.026	−0.027	−0.0235	90.0	41.5	–	–	–
$P_2/ g_e\beta_e$	0.015	0.015	0.015	0.014	90.0	131.5	–	–	–
$P_3/ g_e\beta_e$	0.011	0.012	0.012	0.011	0.0	202.1	–	–	–

Calculated orientations for the four methods are similar and only from PBE0 are given here: and are tilting angles relative to crystallographic axes **c** and **a**, respectively.

[a] Also included for comparison are A (^{17}O) data for the $[AlO^4]^0$ center in quartz from Nuttall and Weil (1981).

discrepancies are the isotropic values (16-17% under-estimation from B3LYP, PBE0 and BHHLYP, but 6% over-estimation from UHF), signifying difficulties in accurate calculations for the small spin polarization. Also included in Table 5-5 are ^{27}Al nuclear quadrupole parameters and ^{17}O hyperfine constants and quadrupole parameters.

5.4 DISCUSSION

5.4.1 Electronic structure and formation mechanism

The structural model of the ^{VI}Al−O^{-}−^{VI}Al center in jeremejevite, with an unpaired spin trapped on a substitutional oxygen atom at the F site between two octahedral coordinated Al atoms, is supported by close matches between the fitted orientations of principal g and A (^{27}Al) axes and those of the Al−O−Al configuration in the ideal structure. Similar relationships have been reported for the well-established $[AlO_4]^0$ center in quartz (Nuttall and Weil 1981), which represents a hole trapped on an oxygen atom linking two Si sites with one of the Si^{4+} cations replaced by an Al^{3+} ion. In particular, Nuttall and Weil (1981) noted that the orientations of the g_1 and A_3 (^{27}Al) axes of the $[AlO_4]^0$ center in quartz are approximately along the Al−Si and Al−O directions, respectively. Also, the axis of the oxygen *p*-orbital component of the unpaired electron wave function for the $[AlO_4]^0$ center in quartz is perpendicular to the Al−O−Si plane (Nuttall and Weil 1981).

Results of periodic DFT calculations (Tables 5-4 and 5-5; Fig. 5-5) provide further support for the structural model of the ^{VI}Al−O^{-}−^{VI}Al center in jeremejevite.

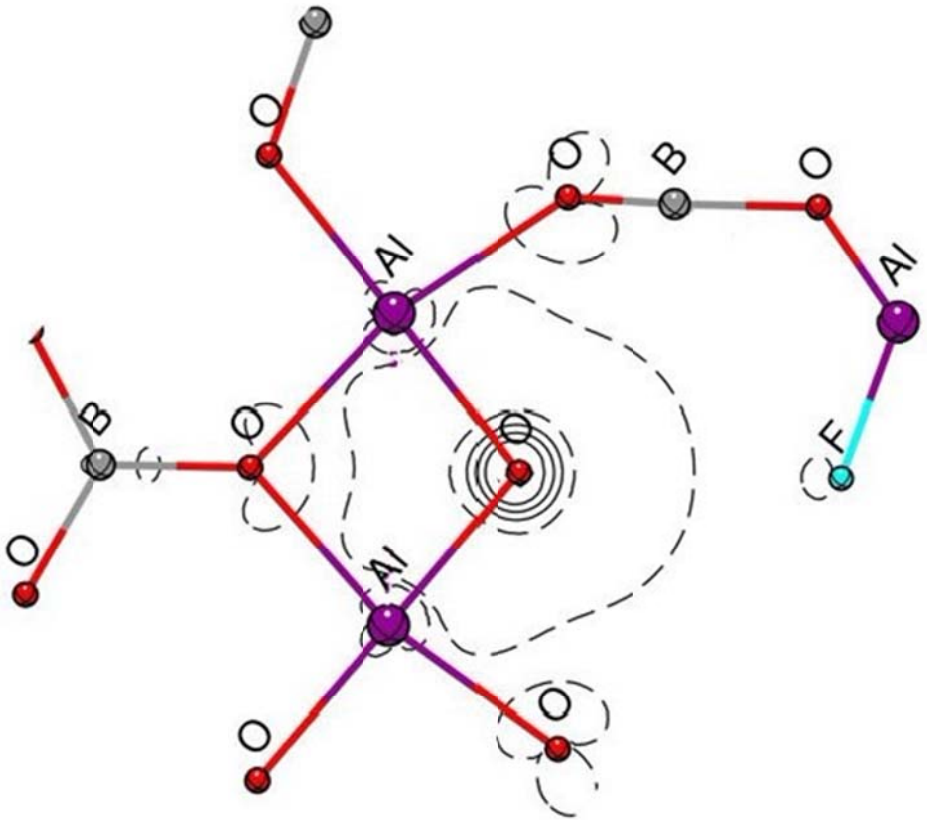

Figure 5-5 Contour map of calculated spin distribution in the Al−O_F−Al plane, illustrating that spin is largely localized on the P_z orbital of the substitutional oxygen atom at the F site. The separation between the isodensity curves is 0.05 e/Bohr^3. *Continuous* and *dashed lines* denote positive and negative values, respectively.

For example, the experimental ^{27}Al hyperfine coupling constants and orientations have been reasonably well reproduced by periodic DFT calculations (Table 5-5). Also, the calculated ^{17}O hyperfine coupling constants for the $^{VI}Al{-}O^{-}{-}^{VI}Al$ center in jeremejevite are closely comparable to experimental values for the $[AlO_4]^0$ center in quartz (Table 5-5; Nuttall and Weil 1981). In addition, the increase of the $Al{-}O_F$ bond distance relative to the Al−F bond is similar to those reported for $[AlO_4]^0$ and $[AlO_6]^0$ centers (e.g., Nuttall and Weil 1981; Mao *et al.* 2010).

For the O^- type radical with the unpaired electron in the oxygen 2*P* orbital (Fig. 5-5), the deviations of the principal *g* values g_x, g_y and g_z from the free-spin value are due to the admixture of P_x and P_y into the ground state by spin-orbital coupling (Slichter 1963) and can be written as follows:

$$\Delta g_x \approx -2\lambda/\Delta E_1 \quad (5\text{-}2a)$$

$$\Delta g_y \approx -2\lambda/\Delta E_2 \quad (5\text{-}2b)$$

$$\Delta g_z \approx 0 \quad (5\text{-}2c)$$

where λ is the oxygen spin-orbit coupling of O^- (= −135 cm^{-1}; Bartram *et al.* 1965), and ΔE_1 and ΔE_2 are the electron excitation energies between the ground state and those formed by moving a hole from the P_z orbital to the P_x and P_y orbitals, respectively. The g_3 value is close to the free electron value and its orientation is approximately perpendicular to the Al−O−Al plane (Table 5-2; Fig. 5-5). Therefore, this axis corresponds approximately to the direction of the ground state P_z orbital. From the experimental values of Δg_x = 0.0267 and Δg_y = 0.0178, we obtain (ΔE_1 = 10,112 cm^{-1} (1.25 eV) and ΔE_2 = 15,168 cm^{-1} (1.88 eV).

Foord *et al.* (1981) noted that F in jeremejevite from Cape Cross, Namibia, is partially replaced by the hydroxyl group. One possible mechanism for the formation of the oxygen hole center in jeremejevite is then trapping of an unpaired spin on the hydroxyl oxygen atom after removal of its proton via a reaction of the following type:

$$O_5Al(OH)AlO_5 \rightarrow O_5AlO\bullet AlO_5 + H^0 \quad (5\text{-}3)$$

where • denotes the unpaired electron. Similar formation mechanisms have been proposed for various $[AlO_4]^0$ and $[AlO_6]^0$ centers (Nuttall and Weil 1981; Dias *et al.* 2009; Mao *et al.* 2010). In particular, Krambrock *et al.* (2004) reported the presence of both the $^{VI}Al{-}O^{-}{-}^{VI}Al$ and atomic hydrogen H^0 centers in gamma-ray-irradiated elbaite. The absence of the H^0 center in jeremejevite may be explained by decay at ambient temperature. Alternatively, the hydrogen atoms either may form diamagnetic molecules such as H_2 or are trapped at other impurities (da Silva *et al.* 2005; Mao *et al.* 2010) However, it remains uncertain why the $^{VI}Al{-}O^{-}{-}^{VI}Al$ center in jeremejevite, after thermal bleaching, cannot be restored by gamma-ray irradiation.

5.4.2 Comparison with other aluminum-associated oxygen hole centers

Similarities in the electronic structure between the $^{VI}Al{-}O^{-}{-}^{VI}Al$ in jeremejevite and the $[AlO_4]^0$ center in quartz have been discussed above. One apparent difference between centers of the $[AlO_6]^0$ and $[AlO_4]^0$ types is their relaxation time. Specifically, centers of the $[AlO_4]^0$ type are commonly detectable only at cryogenic temperatures owing to line broadening arising from spin hoping among similar oxygen atoms at elevated temperatures (Nuttall and Weil 1981). Centers of the $[AlO_6]^0$ type are

commonly detectable at room temperature (Requardt *et al.* 1982; Yu *et al.* 1995; Dias *et al.* 2009; Mao *et al.* 2010), suggesting that the unpaired spin remains localized on a single oxygen atom at this temperature. This difference appears to extend to the $^{VI}Al–O^{-}–^{VI}Al$ and $^{IV}Al–O^{-}–^{IV}Al$ varieties as well. For example, Petrov *et al.* (1989) noted that the $^{IV}Al–O^{-}–^{IV}Al$ centers in albite are observed only at <260 K. On the other hand, all $^{VI}Al–O^{-}–^{VI}Al$ centers in kaolinite, tourmaline, topaz, and jeremejevite are detectable at room temperature (Clozel *et al.* 1995; Krambrock *et al.* 2004; da Silva *et al.* 2005), although the former three are all better resolved at low temperatures.

Marfunin (1979) classified two types of O^{-} centers on the basis of the location of the unpaired electron: (1) in the σ orbital yielding $g_{//} \leq g_e$ and $g_{\perp} > g_e$, and (2) in the π nonbonding orbital, resulting in $g_{//}$ and $g_{\perp}$ switch places ($g_{\perp} \leq g_e$ and $g_{//} > g_e$). In axial symmetry, the two lowest orbitals are completely degenerate. However, Schirmer (2006) noted that the Jahn-Teller effect introduces a slight rhombicity, which can account for the rhombic matrix **g** observed for the $^{VI}Al–O^{-}–^{VI}Al$ center in jeremejevite (Table 5-2). Marfunin (1979) noted that the second group involves hole trapping on a bridging oxygen atom to compensate for the positive charge deficiency arising from one of the cations being replaced by a lower-charged cation. Not surprisingly, the $^{VI}Al–O^{-}–^{VI}Al$ centers in jeremejevite, kaolinite, and topaz all involve hole trapping on a bridging oxygen atom between two octahedral coordinated Al atoms and hence belong to Marfunin's (1979) second type. The $^{VI}Al–O^{-}–^{VI}Al$ center in elbaite, on the other hand, involves hole trapping on the O1 site in the structural

channels formed by Si_6O_{18} (Krambrock *et al.* 2004), consistent with its experimental *g* values characteristic of Marfunin's (1979) first type (Table 5-1).

The proposed $^{VI}Al{-}O^{-}{-}^{VI}Al$ centers (Table 5-1) are also similar in thermal stability. For example, Krambrock *et al.* (2004) and da Silva *et al.* (2005) showed that the $^{VI}Al{-}O^{-}{-}^{VI}Al$ centers in elbaite and topaz are stable up to ~250 and ~500 ℃, respectively. Clozel *et al.* (1994) noted that the B center in kaolinite is completely removed by heating at 300 ℃ for 2 h. The $^{VI}Al{-}O^{-}{-}^{VI}Al$ center in jeremejevite, when subject to isochronal annealing for 10 min each step, undergoes onset of thermal decay at ~300 ℃ and is completely bleached at 525 ℃ (Fig. 5-4).

These similarities suggest that the geometric and electronic model of the $^{VI}Al{-}O^{-}{-}^{VI}Al$ center in jeremejevite can be extended to its analogous defects in other minerals. This is particularly important to the "B centers" in kaolinite, which remains controversial (Clozel *et al.* 1994, 1995; Köksal *et al.* 2004). Clozel *et al.* (1995), in their comprehensive study of the B-center in kaolinite, reported X- and Q-band powder EPR spectra measured at 77 and 150 K, including those from the oriented film method. Clozel *et al.* (1995) showed that the Q-band spectra of the B center consist of three groups of 11 lines with an intensity ratio of 1:2:3:4:5:6:5:4:3:2:1 and have one of its principal axes perpendicular to the ab plane. Clozel *et al.* (1995) interpreted the 11-line feature to represent a hyperfine feature arising from a hole trapped on an oxygen atom interacting with two equivalent octahedral ^{27}Al nuclei (i.e., $^{VI}Al{-}O^{-}{-}^{VI}Al$), but was uncertain whether it forms from irradiation resulting in charge imbalance by the occurrence of a vacancy or impurities in the octahedral or

tetrahedral layers. Also, Clozel *et al.* (1995) was unable to determine whether the hole-trapping oxygen is one of the two oxygen atoms or one of the four hydroxyl oxygen atoms coordinated to an octahedral Al atom. On the basis of a detailed study on an $[AlO_6]^0$ center in prehnite, Mao *et al.* (2010) suggested that the B center in kaolinite forms from hole trapping on one of the hydroxyl oxygen atoms after removal of the proton during irradiation. The $^{VI}Al–O^{-}–^{VI}Al$ center in jeremejevite has the orientations of the g_1- and g_2-axes approximately parallel and perpendicular to the Al−Al direction. In the kaolinite structure, all four hydroxyl oxygen atoms of each Al octahedron are shared with a neighboring Al octahedron in the ab plane. Therefore, a $^{VI}Al–O^{-}–^{VI}Al$ center formed from hole trapping on one of these four hydroxyl oxygen atoms has its g_1- and g_2-axes approximately parallel and perpendicular to the ab plane, respectively, explaining Clozel *et al.*'s (1995) results that one principal *g*-axis is perpendicular to the ab plane.

5.5 REFERENCES

Adamo, C., Barone, V. (1999): Accurate excitation energies from time-dependent density functional theory: assessing the PBE0 model for organic free radicals. *Chemical Physics Letters*, **314**: 152-157.

Adrian, F.J., Jeite, A.N., Spaeth, J.M. (1985): Theory of indirect hyperfine interactions of oxygen-aluminum defects in ionic crystals. *Physical Review. B. Condensed Matter and Materials Physics*, **31**: 3923-3931.

Barklie, R.C., Niklas, J.R., Spaeth, J.M., Bartram, R.H. (1983): ENDOR and EPR of defects in relatively stoichiometric β-alumina. *Journal of Physics. C. Solid State Physics*, **16**: 579-590.

Bartram, R.H., Swenberg, C.E., Fournier, J.T. (1965): Theory of trapped-hole centers in aluminum oxide. *Physical Review*, **139**: A941-A951.

Becke, A.D. (1993a): A new mixing of Hartree-Fock and local density-functional theories. *The Journal of Chemistry Physics*, **98**: 1372–1377.

Becke, A.D. (1993b): Density-functional thermochemistry. III. The role of exact exchange. *The Journal of Chemistry Physics*, **98**: 5648–5652.

Bershov, L.V., Marfunin, A.S. (1981): On schemes of isomorphism of boron in alumosilicates, carbonates and sulfates according to electron-spin-resonance data. *Geokhimya*, **3**: 446-449.

Botis, S.M., Pan, Y. (2010): Theoretical modeling of the Al paramagnetic center and its precursors in stishovite. *Physics and Chemistry of Minerals*, **37**: 119-127.

Clozel, B., Allard, T., Muller, J.P. (1994): Nature and stability of radiation-induced defects in natural kaolinite: new results and a reappraisal of published works. *Clays*

and Clay Minerals, **42**: 657-666.

Clozel, B., Gaite, J.M., Muller, J.P. (1995): Al−O^{-}−Al paramagnetic defects in kaolinite. *Physics and Chemistry of Minerals*, **22**: 351-356.

da Silva, D.N., Guedes, K.J., Pinheiro, M.V.B., Spaeth, J.M., Krambrock, K. (2005): The microscopic structure of the oxygen-aluminum hole center in natural and neutron irradiated blue topaz. *Physics and Chemistry of Minerals*, **32**: 436-441.

Dias, L.N., Pinherio, M.V.B., Krambrock, K. (2009): Radiation-induced defects in euclase: formation of O^{-} hole and Ti^{3+} electron centers. *Physics and Chemistry of Minerals*, **36**: 519-525.

Dovesi, R., Saunders, V.R., Roetti, C., Orlando, R., Zicovich-Wilson, C.M., Pascale, F., Civalleri, B., Doll, K., Harrison, N.M., Bush, I.J., D'Arco, Ph., Llunell, M. (2006): CRYSTAL06 User's Manual, University of Torino, Torino. Italy. http://www.crystal.unito.it

Eachus, R.S., Symons, M.C.R. (1968): Oxides and oxyions of non-metals. X. BO_3^{2-} impurity center in irradiated calcium carbonate. *Journal of the Chemical Society. A. Inorganic, Physical, Theoretical*, **10**: 2438-2441.

Foord, E.E., Erd, R.C., Hunt, G.R. (1981): New data for jeremejevite. *Canadian Mineralogist*, **19**: 303-310.

Gatti, C., Saunders, V.R., Roetti, C. (1994): Crystal-field effects on the topological properties of the electron-density in molecular-crystals. The case of urea. *The Journal of Chemical Physics*, **101**: 10686-10696.

Golovastikov, N.I., Belova, J.N., Belov, N.V. (1955): Crystal structure of jeremejevite. *Zap Vses Mineral O (Leningrad)*, **84**: 405-414.

Hofmeister, A.M., Rossman, G.R. (1985): A model for the irradiative coloration of smoky feldspar and the inhibiting influence of water. *Physics and Chemistry of Minerals*, **12**: 324-332.

Ikeya, M. (1993): New applications of electron paramagnetic resonance: ESR dating, dosimetry, and spectroscopy. World Scientific, Singapore.

Ioffe, V.A., Yanchevskaya, I.S. (1968): Electron paramagnetic resonance and thermoluminescence of irradiated single crystals of the aluminosilicates $NaAlSi_3O_8$ and $LiAlSiO_4$. *Soviet Physics Solid State, USSR*, **10**: 370-374.

Köksal, F., Koseoglu, R., Saka, I., Basaran, E., Sener, F. (2004): Electron

paramagnetic resonance of natural and gamma-irradiated alunite and kaolin mineral powders. *Radiation Effects and Defects in Solids*, **159**: 393-398.

Krambrock, K., Pinheiro, M.V.B., Guedes, K.J., Medeiros, S.M., Schweizer, S., Spaeth, J.M. (2004): Correlation of irradiation-induced yellow color with the O^- hole center in tourmaline. *Physics and Chemistry of Minerals*, **31**:168-175.

Li, R., Li, Z., Mao, M., Pan, Y. (2011): Single-crystal EPR and DFT studies of a $[BO_4]^0$ center in datolite electronic structure, formation mechanism and implications. *Physics and Chemistry of Minerals*, **38**: 33-43.

Li, Z., Pan, Y. (2011): First-principles study of boron oxygen hole centers in crystals: electronic structures and nuclear hyperfine and quadrupole parameters. *Physical Review. B***84**: 115112.

Lowenstein, W. (1954): The distribution of aluminum in the tetrahedral of silicates and aluminates. *The American Mineralogist*, **39**: 92-96.

Mao, M., Nilges, M.J., Pan, Y. (2010): Single-crystal EPR and ENDOR study of an $Al\text{-}O^-$ center in prehnite: implications for aluminum-associated oxyradicals in layer silicates. *European Journal of Mineralogy*, **22**: 381-392.

Marfunin, A.S. (1979): Spectroscopy, luminescence and radiation centers in minerals. Chapter 7, Springer, Berlin.

Marfunin, A.S., Bershov, L.V. (1970): Paramagnetic centers in feldspar and their possible crystallochemical and petrological significance (in Russian). *Doklady Akademii Nauk SSSR*, **193**: 412-414.

Matyash, I.V., Bagmut, N.N., Litovchenko, A.S., Proshko, V.Y.A. (1982): Electron paramagnetic resonance study of new paramagnetic centers in microcline-perthites from pegmatites. *Physics and Chemistry of Minerals*, **8**: 149-152.

Mittani, J.C.R., Matsuoka, M., Watanabe, S. (1999): ESR and TL studies of feldspar. *Radiation Effects and Defects in Solids*, **149**: 175-181.

Mombourquette, M.J., Weil, J.A., McGavin, D.G. (1996): EPR-NMR User's Manual. Department of Chemistry, University of Saskatchewan, Saskatoon, Saskatchewan.

Nada, R., Catlow, C.R.A., Pisani, C., Orlando, R. (1993): An ab-initio Hartree-Fock perturbed-cluster study of neutral defects in LiF. *Modeling and Simulation in Materials Science and Engineering*, **1**: 165–187.

Nilges, M.J., Pan, Y., Mashkovtsev, R.I .(2008): Radiation-damaged-induced defects

in quartz. I. Single-crystal W-band EPR study of hole centers in an electron-irradiated quartz. *Physics and Chemistry of Minerals*, **35**: 103-115.

Nilges, M.J., Pan, Y., Mashkovtsev, R.I. (2009): Radiation-induced defects in quartz. III. W-band EPR, ENDOR and ESEEM study of a peroxy radical. *Physics and Chemistry of Minerals*, **36**: 61-73.

Nuttall, R.H.D., Weil, J.A. (1981): The magnetic properties of the oxygen-hole aluminum centers in crystalline SiO_2. I. $[AlO_4]^0$. *Canadian Journal of Physics*, **59**: 1696-1708.

Pan, Y., Nilges, M.J., Mashkovtsev, R.I. (2008): Radiation-induced defects in quartz. II. Single-crystal W-band EPR study of a natural citrine quartz. *Physics and Chemistry of Minerals*, **35**: 387-397.

Pan, Y., Nilges, M.J., Mashkovtsev, R.I. (2009): Radiation-induced defects in quartz: Multifrequency EPR study and DFT modeling of new peroxy radicals. *Mineralogical Magazine*, **73**: 521-537.

Petrov, I. (1994): Lattice-stabilized CH_3, C_2H_5, NO_2, and O^{1-} radicals in feldspar with different Al-Si order. *The American Mineralogist*, **79**: 221-239.

Petrov, I., Agel, A., Hafner, S.S. (1989): Distinct defect centers at oxygen positions in albite. *The American Mineralogist*, **74**: 1130-1141.

Rae, A.D. (1969): Relationship between experimental Hamiltonian and point symmetry of a paramagnetic species in a crystal. *The Journal of Chemical Physics*, **50**: 2672-2685.

Requardt, A., Hill, F., Lehmann, G. (1982): A firmly localized hole center in the mineral brazilianite $NaAl_3[PO_4]_2(OH)_4$. *Zeitschrift fur Naturforschung Section A*, **37**: 280-286.

Rodellas, C., Garcia-Blanco, S., Vegas, A. (1983): Crystal structure refinement of jeremejevite ($Al_6B_5F_3O_{15}$). *Zeitschrift fur Kristallographie*, **165**: 255-260.

Schirmer, O.F. (2006): O^- bound small polarons in oxide materials. *Journal of Physics. Condensed Matter*, **18**: R667-R704.

Slichter, C.P. (1963): Principles of Magnetic Resonance. New York: Harper and Row, p183.

Speit, B., Lehmann, G. (1976): Hole centers in the feldspar sanidine. *Physica Status Solidi*, **36A**: 471-481.

Speit, B., Lehmann, G. (1982): Radiation defects in feldspars. *Physics and Chemistry of Minerals*, **8**:77-82.

To, J., Sokol, A.A., French, S.A., Kaltsoyannis, N., Catlow, C.R. (2005): Hole localization in $[AlO_4]^0$ defects in silica materials. *The Journal of Chemical Physics*, **122**: 144704.

Weigend, F., Ahlrichs, R. (2005): Balanced basis sets of split valence, triple zeta valence and quadruple zeta valence quality for H to Rn: Design and assessment of accuracy. *Physical Chemistry Chemical Physics*, **7**: 3297-3305..

Wichterlová, B., Nováková, J., Prášil, Z. (1988): Structure of defects in γ-irradiated ZSM-5 and Y zeolites: an e.s.r. study. *Zeolites*, **8**:117-121.

Yu, J., Lee, C., Liu, K., Liu, C., Huang, Y., Payne, D.A., Li, K. (1995): Electron paramagnetic resonance study of an Al-associated oxygen hole center in $KTiOPO_4$: Al crystals. *Journal of Physics and Chemistry of Solids*, **56**: 233-240.

Chapter 6

Conclusions

The present thesis provides EPR results relevant to the fundamental understanding of five defect centers in selected borates and borosilicates. The major findings of the present thesis can be summarized as follow:

- The present research presents a combined single-crystal EPR and DFT result of a $[BO_4]^0$ center in datolite. The unpaired electron is shown to be trapped on the hydroxyl oxygen atom after the removal of the hydrogen atom via a reaction $O_3BOH \rightarrow O_3BO^{\bullet} + H^0$, where $\bullet$ denotes the unpaired electron. Also, our results confirm the thermal stability and decay kinetics of the $[BO_4]^0$ center in datolite by isochronal and isothermal annealing experiments.

- The present study provides detailed results for three arsenic-associated paramagnetic electron centers (I, II and III) in danburite by a combined synchrotron X-ray absorption spectroscopy (XAS), single-crystal EPR and pulse electron spin echo envelope modulation (ESEEM) spectroscopy. Centers I and II are varieties of the $[AsO_2]^{2-}$ radicals, formed from electron trapping on a substitutional As^{3+} ion at the Si site. This model is also supported by the ^{11}B superhyperfine structures determined by ESEEM spectra at 80 K. Center III is the $[AsO_3]^{2-}$ radical, originated from electron trapping on a $[AsO_4]^{3-}$ group after removal of the O_4 atom during gamma-ray

irradiation. The present results allow us to identify that arsenic in danburite is present in both the +3 and +5 oxidation states and preferentially occupies the Si site.

- The present work also reports single-crystal EPR and DFT results for a $^{VI}Al–O^{-}–^{VI}Al$ center in jeremejevite. Our results suggest that this $^{VI}Al–O^{-}–^{VI}Al$ center represents hole trapping on a hydroxyl oxygen atom linked to two equivalent octahedral Al^{3+} ions, after the removal of the proton. Also, isochronal annealing experiments provide information about the thermal stability of the $^{VI}Al–O^{-}–^{VI}Al$ center. These data obtained from the $^{VI}Al–O^{-}–^{VI}Al$ center in jeremejevite provide new insights into analogous defects that have been documented in several other minerals.